UNIVERSITY OF OKLAHOMA

GRADUATE COLLEGE

TOWARDS IMPROVED QPE BY CAPITALIZING GROUND- AND SPACE-BASED PRECIPITATION MEASUREMENTS

A DISSERTATION

SUBMITTED TO THE GRADUATE FACULTY

in partial fulfillment of the requirements for the

Degree of

DOCTOR OF PHILOSOPHY

By

YIXIN WEN
Norman, Oklahoma
2015

Downloaded from SHAREOK. Persistent Handle URL: https://hdl.handle.net/11244/14634

TOWARDS IMPROVED QPE BY CAPITALIZING GROUND- AND SPACE-BASED PRECIPITATION MEASUREMENTS

A DISSERTATION APPROVED FOR THE
SCHOOL OF METEOROLOGY

BY

_____
Dr. Yang Hong, Chair

_____
Dr. Guifu Zhang, Co-Chair

_____
Dr. Jonathan J. Gourley

_____
Dr. Robert D. Palmer

_____
Dr. Jian Zhang

_____
Dr. Naiyu Wang

© Copyright by YIXIN WEN 2015
All Rights Reserved.

Table of Contents

Table of Contents ..... **iv**

List of Figures ..... **vii**

List of Tables ..... **xi**

Chapter 1. Introduction **1**

1.1 Background 1

1.1.1 Gauges 1

1.1.2 Ground Weather radar (single-pol, Dual-pol, MRMS) 2

1.1.3 Spaceborn Radar (TRMM, GPM) 5

1.2 Objectives 7

1.3 Outline of the Dissertation 7

1.4 Hypotheses 10

References 12

Chapter 2. Ground Polarimetric Weather Radar **15**

2.1 Cross validation statistic results 15

2.1.1 Data 15

2.1.2 Spaceborne Radar and Ground Radar Matching Methods 18

2.1.3 Cross-Validation indices 19

2.1.4 Comparison Results 20

2.2 HCA analysis 28

2.3 Snow estimation by ground polarimetric radar 36

2.3.1 Motivation 36

2.3.4 Methodology 40

2.3.3 Case study results 42

References 57

Chapter 3. VPR_IE methods 59

3.1 Concept of VPR_IE 61

3.1.1 Overview 61

3.1.2 Physically-based VPR model 63

3.2 Implementation of VPR_IE 67

3.3 Case study of VPR_IE 70

References 83

Chapter 4. Real time climatological VPR_IE 86

4.1 Climatological VPRs from TRMM/PR 86

4.1.1 TRMM/PR more than 10 years observation 87

4.1.2 Data processing 88

4.2 Climatological VPR_IE implementation 91

4.2.1 Ku-band to S-band conversion 94

4.2.2 Apparent VPR at Different Radar Ranges 95

4.2.3 Climatological VPRs for VPR Correction 95

4.2.4 Procedure for Real-time Implementation 96

4.3 Comprehensive Evaluation of CVPR_IE 97

4.3.1 Data and methodology 98

4.3.2 Results 102

4.3.3 Discussion 117

References 122

Chapter 5. Overall conclusions and future work 124

5.1 Summary and conclusions 124

5.2 GPM era 129

References 131

List of Figures

Figure 1.1 Two-dimensional effective WSR-88D radar coverage at a constant height at 1km, 2km, and 3km Above Ground Level from left to right, respectively (from Maddox et al., 2002). 5

Figure 2.1 Study region showing KOUN location and 50km, 100km and 150km range rings. 17

Figure 2.2 Schematic of resolution volume matching technique of ground-based KOUN and space-borne TRMM Precipitation Radar (PR). The purple area shows the intersections between KOUN and PR sweeps. 19

Figure 2.3(a) Scatterplot with colored data density of KOUN and TRMM PR melting layer heights for 19 events. The correlation coefficient, bias ratio, MAE, RMSE, and sample size are shown in the embedded text. (b) Histograms of KOUN and TRMM PR melting layer heights for data shown in Fig. 2.3a. 22

Figure 2.4 Scatterplot of event-averaged melting layer heights from KOUN and TRMM PR. (b) Histogram of melting layer height difference of data shown in Fig. 2.4a. 24

Figure 2.5 Reflectivity bias between PR and KOUN for each event. Event details are provided in Table 2.1. 26

Figure 2.6 Scatterplots with colored data density and histograms of KOUN and TRMM PR reflectivity. (a) and (b) reflectivity and attenuation-corrected PR reflectivity with no additional quality control; (c) and (d) same as (a) and (b) but non-meteorological echoes based on KOUN's hydrometeor classification algorithm (HCA) have been removed; (e) and (f) same as (c) and (d) but applied a minimum18 dBZ threshold. 27

Figure 2.7 Relationships between reflectivity factors at S and Ku bands for liquid water, hail and dry snow. Backscatter cross sections are simulated using T-matrix method at S and Ku bands, where reflectivity calculations assume a mono-dispersed drop size distribution. 30

Figure 2.8 Scatterplots with colored data density in the first column and histograms in the second column for reflectivity observed for different hydrometeors as determined from KOUN HCA: (row a) rain/hail mix, (row b) wet snow, (row c) graupel, (row d) heavy rain, (row e) big drops, (row f) moderate rain, and (row g) dry snow. 33

Figure 2.9 Bias (%) of TRMM PR reflectivity observations relative to KOUN for different hydrometeor types as discriminated by the dual-polarization HCA 34

Figure 2.10 Mean vertical reflectivity profiles for (a) convective, (b) stratiform, and (c) all rain types as determined by TRMM 2A23. ZG is reflectivity from KOUN, Zm is measured reflectivity from TRMM 1C21 with no attenuation correction, and Zc is attenuation-corrected TRMM 2A25. 36

Figure 2.11. Conical volume representing azimuthally averaged quasi-vertical profiles of polarimetric radar variables in the dry snow region. The radar variables will be related to rain gauge measurements on the ground to derive Z-SWE relation. The parameters in Z-SWE relation will be constrained by dual-polarimetric data and environmental variables obtained from sounding data or other remote sensors. 41

Figure 2.12. Dec. 5, 2014 event information from MRMS. (a) Hourly accumulation of rainfall estimated by ground radars; (b) Freezing level height estimated by RAP model; (c) Surface Precipitation Type; (d) Relative Humidity from Pittsburg Sounding observation station. 44

Figure 2.13. The height vs time representation of quasi-vertical profiles of Z, Z_{DR}, ρ_{hv}, and Φ_{DP} retrieved from the KCLE WSR-88D radar data collected at elevation 19.5° during the stratiform rain event in Cleveland, OH on 5 Dec 2014 and 6 Dec. 2014. 46

Figure 2.14. The height vs. time representation of vertical profile of hourly radar SWE calculated by using $Z=75R^2$. The colored circles indicate the rain gauges measurements on ground. 48

Figure 2.15. Scatterplot of 1-h radar precipitation estimates at 3 km height (circles) and at 4 km height (filled circles). 49

Figure 2.16. Shows radar reflectivity measurements from heights of (a) 3 km and (b) 4 km. The circles indicate the improvements of radar snow estimates by using calibrated α values in Z-S relation. 50

Figure 2.17. The height vs. time representation of vertical profile of hourly radar SWE calculated by using $S=0.03R^{0.64}$. The colored circles indicate the rain gauge measurements on ground. 51

Figure 2.18. The height vs. time representation of vertical profile of α value 52

Figure 2.19. The height vs. time representation of vertical profiles of temperature (left) and relative humidity (right) from RAP model. 53

Figure 2.20. The change of α with height, temperature and relative humidity. The color indicates the scan time. 55

Figure 2.21. The change of α with Z_{DR}. The color indicates the scan time. 56

Figure 2.22. Left: The change of α with ρ_{hv}. Right: The change of α with Φ_{DP}. The color indicates the scan time. 56

Figure 3.1. Illustration of using spaceborne radar measured representative VPR to improve the near-surface QPE based on ground-radar. 62

Figure 3.2. Steps for incorporating TRMM-PR measurements into NMQ-QPE (VPR-IE method). The representative example of the VPR on December 8, 2009 is shown: (a) fit

a physically based VPR model (5 parameters) on the Ku-band TRMM-PR reflectivity profiles; (b) convert the Ku-band VPR (dotted grey line) into S-band VPR (solid black line); (c) convolve the S-band VPR with the sampling properties of WSR-88D ground radars. On panel (c), apparent VPRs are simulated from the S-band VPR from (b) at various distances (from 20 to 240 km with an interval of 20 km) using the beam characteristics of WSR-88D radars. 66

Figure 3.3. Histograms of the five parameters of the physically based VPR model fit on TRMM-PR reflectivity profiles passing over Arizona at 01:35Z on 8 December 2009: (a) the top of precipitation , (b) the density parameter , (c) the freezing level height , (d) the melting layer thickness , and (e) the slope of the profile in liquid phase 68

Figure 3.4. An image showing the topography around the study area (black dashed box) and the locations of rain gauges (circles) and WSR-88D radar sites (white circles with cross). The inset black and white map shows the radar coverage at 3 km above ground level. 74

Figure 3.5. Scatterplots of 1-hour radar precipitation estimates before (black) and after (white) the corrections for all five events combined using the (a) rainfall rate calibration method (b) rings-based range adjustment and (c) VPR-IE method. 76

Figure 3.6. 1-hour radar estimates before (Column a) and after (Column b) adjustment using the VPR-IE method..... 78

Figure 3.7. QPE error (multiplicative bias ((radar-raingauge)/raingauge ratios)) in terms of range for the 8 December 2009 case (left) and for the 22 January case (right). 82

Figure 4.1. Normalized VPR shape for stratiform precipitation with different rainfall rates for (a) – (d) the four seasons (from Cao et al., 2013, Fig. 12) 91

Figure 4.2. Illustration of using spaceborne radar measured representative VPR to improve the near-surface QPE based on ground-radar. Different physical processes associated with different state of hydrometeors at various heights are also shown in the figure..... 92

Figure 4.3. Framework of proposed VPR-IE system at OU. The major components associated with VPR correction are enclosed by dashed lines (from Cao et al., 2014). 93

Figure 4.4. S-band climatological VPRs. Y-axis denotes the height relative to the freezing level. 96

Figure 4.5. An image showing the topography of the study area and the locations of rain gauges (white crosses) and WSR-88D radar sites (white circles with cross) with 100-km range rings. 99

Figure 4.6. Climatological VPRs (already converted from Ku-band) for winter season from 11-year TRMM/PR observations. X-axis denotes the difference relative to the

reflectivity measured at 1 km below freezing level. Y-axis denotes the height relative to the freezing level. 100

Figure 4.7. Procedure of real-time climatology-based VPR correction. 101

Figure 4.8. The probability distribution of RB, CC, MAE and RMSE using bootstrapping method. 104

Figure 4.9. The statistics before and after CVPR_IE for a range of sampling sizes. The whiskers refer to the interquartile range. 106

Figure 4.10. The occurrences of improved QPE after correction based on gauge measurements is denoted as dashed black line; the occurrences of worse QPE after correction is denoted as solid line. 108

Figure 4.11. The range-dependent statistics of beam height relative to freezing level. The dashed lines denote radar only rain estimation before correction; the black lines denote rain estimation after CVPR_IE; the gray line denotes rain gauge measurements on the ground. 110

Figure 4.12. Similar to Fig. 4.11. But statistics are along Radar Quality Index (RQI). 112

Figure 4.13. Similar to Fig. 4.11. Statistics are along the stratiform precipitation proportion in one hour 114

Figure 4.14. Similar to Fig. 4.11. Statistics are with Bright Band precipitation proportion. 116

Figure 4.15. Hourly precipitation accumulation from Event 8 Dec 2009. (a) Radar only QPE; (b) Gauge measurements from HADS and the Maricopa County mesonet; (c) Using physically-based VPR-IE approach; (d) Using climatological VPR-IE scheme approach. The red triangles denote the locations of WSR-88D radar sites 119

Figure 4.16. (a) Physically based VPR from Event 8 Dec 2009 (gray line) and climatological VPRs; (b) Beam height relative to the freezing level in meters. 120

List of Tables

Table 1. Description of events used in PR-KOUN comparisons. Times are in UTC. 17

Table 2. Summary of Z(S) relations for dry snow listed in literature and utilized by the WSR-88D network in the US. 38

Table 3. Summary of the events. 73

Table 4. Statistical results of the three TRMM PR-based correction approaches. I is the rainfall rate calibration method; II is the rings-based range adjustment method; III is VPR-IE method. The method with the best performance according to the statistic is denoted in boldface. 79

Table 5. TRMM V7 data (2A23, 2A25) availability by month, where the numbers in the first row indicate the month. (from Cao et al., 2013, Table 1) 88

Table 6. Statistical results of the climatological VPR_IE approach. The first row shows the statistics before CVPR_IE correction; the second row shows the statistics after CVPR_IE correction. 103

Table 7. Relative changes of statistics due to CVPR-IE and physically based VPR-IE. 117

Chapter 1 Introduction

1.1 Background

Reliable quantitative information on the spatial and temporal distribution of precipitation is essential for hydrologic and climatic applications, which range from real-time flood forecasting to evaluation of regional and global atmospheric model simulations. Therefore, accurate measurement of precipitation at a range of spatial and temporal resolutions is invaluable for a variety of scientific applications. However, accurately measuring precipitation has been a challenge to the research community predominantly because of its high variability in space and time. There are primarily three major types of techniques of precipitation measurement: (1) surface-based in-situ precipitation gauges, (2) weather radars, and (3) space-based meteorological satellites.

1.1.1 Gauges

To measure the liquid rain, rain gauges provide perhaps the best available point measurements. A rain gauge collects rainfall directly in a small orifice and measures the water depth, weight, or volume. A various types of rain gauges have been developed such as weighing gauges, tipping-bucket gauges, distrometers, capacitance gauges, and others, among which, tipping-bucket gauges are mostly used for ground-based rainfall measurements by National Weather Service (Humphrey et al. 1997) and also used in rainfall processing of products from Next Generation Weather Radar (NEXRAD) radar systems (Young et al. 1999). The tipping bucket rain gauge networks around the globe are deployed to provide ground validation products for the Tropical Rainfall Measuring Mission (TRMM) satellite (Simpson et al. 1988). However, several studies showed that the gauge data are corrupted by both random and systematic errors (Sevruk and Lapin,

1993). The systematic error is the most significant source of error and includes losses due to wind, wetting, evaporation, and splashing. Also, rain gauges suffer from poor spatial coverage and lack areal representation over land, which becomes particularly problematic for intense rainfall with high spatial variability (Zawadzki 1975).

Ground measurement for solid precipitation is more challenging. The World Meteorological Organization (WMO) conducted a comprehensive study of the accuracy, reliability, and repeatability of automatic solid precipitation measurement methods. The report highlighted a number of challenges, including blockage of the gauge orifice by snow capping the gauge or accumulating on the side of the orifice walls; undercatch of snow due to the formation of updrafts over the gauge orifice; the unknown role of turbulence on gauge catch; and the large variability in gauge catch efficiency for a given gauge and wind speed (Goodison et al. 1998). Measurement errors for solid precipitation frequently range from 20% to 50% (Rasmussen, et al. 2012), as big as the first-guess radar estimates.

1.1.2 Ground Weather radar (single-pol, Dual-pol, MRMS)

The development of weather radar after World War II has dramatically increased our ability of measuring high-resolution precipitation data in space and time. Weather radar has proven its value to the nation since the installation of the current Weather Surveillance Radar – 1988 Doppler (WSR-88D) network (NEXRAD). The U.S. NEXRAD network consists of 159 S-band (2.8 GHz) radars. The 10 cm wavelengths of S-band radar are much larger than the diameter of the droplets or ice particles, so the Rayleigh scattering occurs at this frequency. Shorter wavelengths are useful for smaller

particles, but the signal is more quickly attenuated. So a S-band radar is preferred but is more expensive than a 5-cm C-band radar and 3-cm X-band radar.

In conventional rainfall estimation using single-polarimetric radar accuracy is often limited by frozen or partially frozen hydrometeors (e.g., hail, wet snow, graupel) as well as non-meteorological scatterers (e.g., ground clutter, birds, insects). Polarimetric weather radar can significantly improve QPE by identifying rain echoes from other hydrometeor types and as such is a very powerful tool for PR validation (Chandrasekar et al. 2008). Park et al. (2009) developed a polarimetric radar Hydrometeor Classification Algorithm (HCA) that discerns 10 different classes of radar echo: 1) ground clutter or anomalous propagation, 2) biological scatterers, 3) dry aggregated snow, 4) wet now, 5) crystals of various orientations, 6) graupel, 7) big drops, 8) light and moderate rain, 9) heavy rain, and 10) a mixture of rain and hail. The polarimetric HCA, which includes an automated detection of the bright band, also plays a fundamental role in the polarimetric QPE through a rainfall estimation scheme that varies according to hydrometeor type (Giangrande et al. 2008b). Polarimetric radar has also been used to observe winter storm events. Ibrahim (1998) present a comparison of polarimetric radar observations and in-situ 2D-video disdrometer observations in winter precipitation to study microphysical properties of snow. Trap et al, (2010) uses polarimetric radar to observe winter storms with both snow and mixed-phase precipitation in Oklahoma. Also in Oklahoma, Zhang et al, 2010 deployed a 2D video disdrometer to observe winter precipitation events and calculated polarimetric radar variables for comparison with a polarimetric weather radar data in Norman, Oklahoma

(KOUN). Polarimeric weather is becoming a powerful tool of frozen precipitation estimation.

In Norman, Oklahoma, a project built upon data collected by the NEXRAD network is NOAA's Multi-Radar/Multi-Sensor (MRMS) system (previous National mosaic QPE (NMQ) system), developed by researchers at the National Severe Storms Laboratory (NSSL) and the University of Oklahoma (OU). The MRMS system combines information from all ground-based radars comprising the National Weather Service's NEXRAD network, mosaics reflectivity data onto a common 3D grid, estimates surface rainfall accumulations and types, and blends the estimates with collocated rain gauge networks to arrive at accurate, ground-based estimates of rainfall. Based on the significant research already performed on the ground-based MRMS data in regards to data quality (Lakshmanan et al. 2007), data mosaicking techniques (Zhang et al. 2005), rainfall estimation (Vasiloff et al. 2007), the system has been generating high-resolution national 3-D reflectivity mosaic grids (31 levels) and a suite of severe weather and QPE products at a 1-km horizontal resolution and 5-minute update cycle since June 2006 (Zhang et al. 2011). Since July 2013, the MRMS has accommodated the recent dual-polarization upgrade of NEXRAD radars. Currently, the MRMS data are disseminated across government agencies and universities in real-time and have been utilized in applications including data assimilation, Numerical Weather Prediction (NWP) model verification and aviation product development (e.g., icing severity). A web-based display and rain gauge-based validation system has also been built around the datasets and is freely accessible on the Internet (http://nmq.ou.edu).

Despite these recent advances, reliable ground-based precipitation measurements are difficult to obtain over all regions of the world, including many mountainous regions (e.g., Intermountain West of the US), due to the lack of adequate ground radar coverage from intervening terrain blockages (see Fig. 1.1). The limitations of rain gauges and weather radar systems highlight the attraction of space-based meteorological satellites to obtain seamless regional and global precipitation information from the vantage point for weather forecasting, modeling the hydrological cycle, and climate studies.

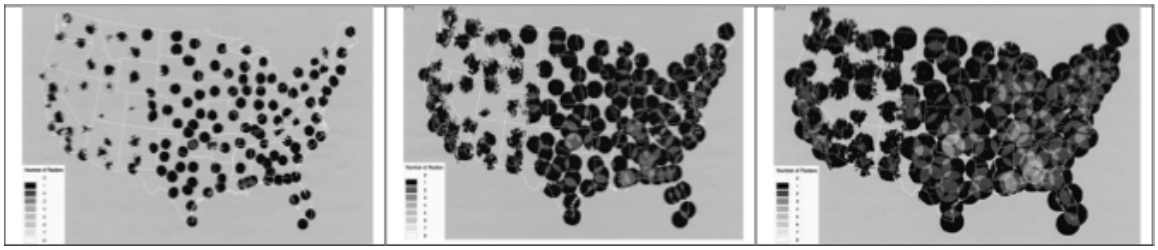

Figure 1.1 Two-dimensional effective WSR-88D radar coverage at a constant height at 1km, 2km, and 3km Above Ground Level from left to right, respectively (from Maddox et al., 2002).

1.1.3 Spaceborn Radar (TRMM, GPM)

One of the main advantages of satellite QPE is their ability to provide information over areas where sparse or no in-situ observations are available such as in remote areas, mountainous regions, and the vast oceanic surface. The first meteorological satellite was launched in 1960 and since then a plethora of sensors have been developed and launched to observe the atmosphere (Gruber et al. 2008).

The NASA Tropical Rainfall Measuring Mission (TRMM) was launched in 1997. Onboard is the Precipitation Radar (PR), which is the first quantitative space-borne weather radar dedicated to measuring tropical precipitation from space (Simpson

et al. 1998). The PR operating at Ku band (13.8 GHz) often suffers attenuation that is corrected by a combination of the surface reference and Hitschfeld-Bordan methods (Iguchi et al. 2000). Compared to horizontally scanning NEXRAD radars, TRMM-PR is much less impacted by mountain blockage and beam broadening effects in the vertical direction (Kummerow et al., 2000).

Since the launch of TRMM, we have witnessed the unprecedented development of a number of high-resolution, space-borne quantitative precipitation estimates (QPE) with quasi-global coverage at sub-daily sampling frequencies (3-hour or half-hourly) and relatively high spatial resolutions (25 km or down to geostationary satellite pixel resolution, 4 km). These satellite-based, high-resolution precipitation products have been developed by combining information from the high-sampling geostationary infrared (IR), and the superior-quality data from the Low-Earth-Orbiting passive microwave (MW) and space-borne weather radar (Hsu et al. 1997; Sorooshian et al. 2000; Kidd et al. 2003; Hong et al. 2004; Joyce et al. 2004; Turk and Miller 2005; Hong et al. 2007; Huffman et al. 2007). Benefited from the success of the TRMM program, Global Precipitation Measurement (GPM) spacecraft was launched in Feb. 2014. With a multi-satellite constellation, the GPM spacecraft carries a dual-frequency Phased Array Radar (Ku-Ka band) to provide measurements of 3-D precipitation structures and microphysical properties to serve as a space-based precipitation microphysics observatory for improved understanding of precipitation processes and retrieval algorithms (Petersen et al., 2008). However, verification and refinement of satellite precipitation retrievals requires ground-validation datasets.

Even though the internal and external calibration of spaceborne radars confirms that the PR/DPR functions properly and has good performance in quantitatively measuring the three-dimensional structure of precipitation (Kozu et al. 2001), cross validation with ground radars (GR) – in particular, those with polarimetric capability – is of vital importance to understanding spaceborne radar measurements and derived products.

1.2 Objectives

Accurately measuring precipitation at high spatiotemporal resolution over a large area has been a challenge to the research community predominantly because of its high variability in space and time. Ground weather radar with polarimetric capability can improve QPE by identifying different hydrometeor types and retrieving particle size distributions. Also, ground polarimetric radars provide a very powerful tool to validate PR measurements and derived products (Chandrasekar et al. 2008).

Despite the recent advances of GR network such as the polarimetric upgrade, it is still difficult to obtain seamless coverage of ground QPE, particularly in the Intermountain West of the U.S. due to inadequate radar coverage from intervening terrain blockages (Maddox et al. 2002); thus, highlights the attraction of satellites (TRMM and GPM) to obtain regional and global precipitation information. To achieve the most possible accurate precipitation, the efforts are made to capitalize the ground- and space-based precipitation measurements.

1.3 Outline of the Dissertation

This dissertation consists of five Chapters: the first Chapter is the introductive Chapter which describes the problem and raises the objectives, Chapters 2 to 4 are the

three main Chapters followed by Chapter 5 which is an overall summary of this dissertation.

Chapter 2 introduces ground-based polarimetric weather radar, which is arguably the most powerful validation tool that provides physical insight into the development and interpretation of space-borne weather radar algorithms and observations. This study aims to compare and resolve discrepancies in hydrometeor retrievals and reflectivity observations between the NOAA/National Severe Storm Laboratory (NSSL) "proof of concept" polarimetric WSR-88D radar (KOUN) and the space-borne precipitation radar (PR) onboard NASA's Tropical Rainfall Measuring Mission (TRMM) platform. An intercomparison of PR and KOUN melting layer heights shows a high correlation coefficient of 0.88 with relative bias of 5.9%. A resolution volume matching technique is used to compare simultaneous TRMM PR and KOUN reflectivity observations. The comparisons reveal an overall bias <0.2% between PR and KOUN. The bias is hypothesized to be from non-Raleigh scattering effects and/or errors in attenuation correction procedures applied to Ku-band PR measurements. By comparing reflectivity with respect to different hydrometeor types (as determined by KOUN's Hydrometeor Classification Algorithm), we find the bias is from echoes classified as rain/hail mixture, wet snow, graupel and heavy rain, respectively. This Chapter also discusses the quantitative frozen precipitation estimation by polarimetric radars. The polarimetric signatures of snow provide valuable insights into its microphysical processes/properties and thus potentially improve radar snow estimation.

Chapter 3 proposes an approach that identifies and corrects for the vertical profile of reflectivity (VPR) by using Tropical Rainfall Measuring Mission (TRMM) precipitation radar (PR) measurements in the region of Arizona and southern California, where ground-based Next Generation Radars (NEXRAD) find difficulties in making reliable estimation of surface precipitation amounts due to complex terrain and limited radar coverage. A VPR Identification and Enhancement (VPR-IE) method based on the modeling of the vertical variations of the equivalent reflectivity factor using a physically-based parameterization is employed to obtain a representative VPR at S-band from the TRMM PR measurement at Ku-band. Then the representative VPR is convolved with ground radar beam sampling properties to compute apparent VPRs for enhancing NEXRAD Quantitative Precipitation Estimation (QPE). The VPR-IE methodology is evaluated with several stratiform precipitation events during the cold season and compared to two other statistically-based correction methods, i.e., TRMM PR-based rainfall calibration and a range ring-based adjustment scheme. The results show that the VPR-IE has the best overall performance and provides much more accurate surface rainfall estimates than the original ground-based radar QPE but limited to TRMM/PR observation availability.

In Chapter 4 discussed how to implement the VPR-IE concept into the MRMS (previous NMQ) system in real-time. Climatological VPRs from 11 years of TRMM PR observations for different stratiform/convective rain types, seasons, and surface rain intensities have been characterized. Then, these representative profiles are used to adjust ground radar-based precipitation estimates in the NMQ system based on different precipitation structures. A comprehensive evaluation of the newly developed

Climatological VPR-IE (CVPR-IE) method is conducted on winter events (January, February, and December) in 2011. The statistical analysis reveals that the CVPR-IE method provides a clear improvement over the original radar QPE in the NMQ system for the study region. Compared to physically-based VPRs from real-time PR measurements, climatological VPRs have limitations in representing precipitation structure for individual events.

The last Chapter is the overall summary and conclusions of all chapters. The prospects in the GPM era are also discussed.

1.4 Hypotheses

The following hypotheses are made in this dissertation:

1. An intercomparison of PR and KOUN hydrometeor retrievals and reflectivity observations between the KOUN polarimetric WSR-88D radar and TRMM PR is conducted. The bias is hypothesized to be from non-Rayleigh scattering effects and/or errors in attenuation correction procedures applied to Ku-band PR measurements. This research motivates and invites synergistic development of multisensory rainfall algorithms using coordinated observations from space and ground.

2. The intercept α in the power-law relation $S = \alpha Z^{\beta}$ increases with height and decreasing temperature. The dynamic Z-S relationship is desired in quantitative frozen precipitation estimate.

3. Reliable ground-based precipitation measurements are difficult to obtain over all regions of the world, including many mountainous regions, due to the lack of adequate ground radar coverage from intervening terrain blockages. The physically-based VPR_IE method integrates TRMM/PR products (4-km precipitation quantity, types, and 250-meter VPR) into the NMQ ground-based rainfall estimation system to improve the precipitation estimation at surface.

4. The temporal resolution of TRMM limits the application of VPR-IE method operationally. In order to implement the VPR-IE concept into the NMQ system in real-time, climatological VPRs from 11 years of TRMM PR observations are used to adjust ground radar-based precipitation estimates in the NMQ system based on different precipitation structure. The comprehensive evaluation of the method reveals that the method provides a clear improvement over the original ground radar QPE in the NMQ system.

References

Chandrasekar, V., A. Hou, E. Smith, V.N. Bringi, S.A. Rutledge, E. Gorgucci, W.A.Petersen, and G. S. Jackson, 2008: Potential role of dual-polarization radar in the validation of satellite precipitation measurements: Rationale and opportunities. *Bull. Amer. Meteor. Soc.*, **89,** 1127-1145.

Giangrande, S. E., J. M. Krause, and A. V. Ryzhkov, 2008a: Automatic designation of the melting layer with a polarimetric prototype of the WSR-88D radar. *J. Appl. Meteor. Climatol.*, **47,** 1354-1364.

Goodison, B. E., P. Y. T. Louie, and D. Yang, 1998: WMO solid precipitation measurement intercomparison. Instruments and Observing Methods Rep. 67 (WMO/TD 872), World Meteorological Organization, Geneva, Switzerland, 212 pp.

Gruber, A., and V. Levizzani, 2008: A Project of the World Climate Research Programme Global Energy and Water Cycle Experiment (GEWEX) Radiation Panel, World Climate Rearch Programme REPORT, WCPR-128, WMO/TD-No. 1430.

Hong Y., K.L. Hsu, X. Gao, and S. Sorooshian, 2004, Precipitation Estimation from Remotely Sensed Imagery Using Artificial Neural Network - Cloud Classification System (PERSIANN-CCS), *Journal of Applied Meteorology*, Vol. **43**, No. 12, pp. 1834–1853.

Hong, Y, D. Gochis, J.T. Chen, K.L. Hsu, and S. Sorooshian, 2007, Evaluation of Precipitation Estimation from Remote Sensed Information using Artificial Neural Network-Cloud Classification System (PERSIANN-CCS) Rainfall Measurement Using the NAME Event Rain Gauge Network, *Journal of Hydrometeorology*, **8(3)**, p469-482.

Hong, Y., Y. Wen, Z. Flamig, G. Zhang, T. Shaun, J. Gourley 2009, Cross Validation of TRMM Space Radar with Ground Polarimetric Radar, The First Symposium on Radar and Modeling Studies of the Atmosphere, Kyoto, Japan, Nov 10-13, 2009

Hsu, K., X. Gao, S. Sorooshian, and H. V. Gupta, 1997: Precipitation estimation from remotely sensed information using artificial neural networks. *J. Appl. Meteor.*, **36,** 1176–1190.

Huffman, G.J., R.F. Adler, D.T. Bolvin, E.J. Nelkin, 2010: The TRMM Multi-satellite Precipitation Analysis (TMPA). Chapter 1 in Satellite Applications for Surface Hydrology, F. Hossain and M. Gebremichael, Eds. Springer Verlag, ISBN: 978-90-481-2914-0, 3-22

Humphrey, M. D., J. D. Istok, J. Y. Lee, J. A. Hevesi, and A. L. Flint, 1997: A new method for automated dynamic calibration of tipping-bucket rain gauges. *J. Atmos. Oceanic Technol.*, **14,** 1513–1519.

Ibrahim, I.A., V. Chandrasekar, V.N. Bringi, P.C. Kennedy, P.C., M. Schoenhuber, H.E. Urban, W.L. Randen, 1998: Simultaneous multiparameter radar and 2D-video disdrome- ter observations of snow. Geoscience and Remote Sensing Symposium Proceedings, IGARSS '98, pp.437-439 vol.1.

Iguchi, T., R. Meneghini, J. Awaka, T. Kozu, and K. Okamoto, 2000: Rain profiling algorithm for TRMM precipitation radar. *J. Appl. Meteor.,* **39,** 2038-2052.

Joyce, R. J., J. E. Janowiak, P. A. Arkin, and P. Xie, 2004: CMORPH: A method that produces global precipitation estimates from passive microwave and infrared data at high spatial and temporal resolution. *J. Hydrometeor.***, 5**, 487–503.

Kidd, C. K., D. R. Kniveton, M. C. Todd, and T. J. Bellerby, 2003: Satellite rainfall estimation using combined passive microwave and infrared algorithms. *J. Hydrometeor*., **4**, 1088–1104.

Kozu, T., and Coauthors, 2001: Development of precipitation radar onboard the Tropical Rainfall Measuring Mission (TRMM) satellite. *IEEE Trans. Geosci. Remote Sens.*, **39,** 102-116.

Kummerow, C., and Coauthors, 2000: The status of the Tropical Rainfall Measuring Mission (TRMM) after two years in orbit. *J. Appl. Meteor.*, **39,** 1965–1982.

Lakshmanan, V., A. Fritz, T. Smith, K. Hondl, and G. Stumpf, 2007: An automated technique to quality control radar reflectivity data. *J. Appl. Meteor. Climatol.,* **46**, 288-305.

Maddox, R., J. Zhang, J.J. Gourley, and K. Howard, 2002: Weather radar coverage over the contiguous United States. *Wea. And Forecast*. , **17**, 927-934

Park, H., A. V. Ryzhkov, D. S. Zrnic, and K. E. Kim, 2009: The Hydrometeor classification algorithm for the polarimetric WSR-88D: description and application to an MCS. *Wea. Forecasting*, **24,** 730-748.

Petersen, Walter A and M. R. Schwaller, 2008: NASA GPM Ground Validation Science Implementation Plan.

Rasmussen, R., and Coauthors, 2012: How well are we measuring snow? The NOAA/FAA/NCAR winter precipitation test bed. *Bull. Amer. Meteor. Soc.*, **93**, 811–829.

Sevruk, B., and M. Lapin, Precipitation measurement and quality control, in Proceedings of the International Symposium on Precipitation and Evaporation, vol. 1, Slovak Hydrometeroral. Inst., Bratislava, 1993.

Simpson, J., C. Kummerow, W.-K. Tao, and R. F. Adler, 1996: On the tropical rainfall measuring mission (TRMM). *Meteor. Atmos. Phys.,* **60**, 19-36.

Sorooshian, S., K.-L. Hsu, X. Gao, H. V. Gupta, B. Imam, and D. Braithwaite, 2000: Evaluation of PERSIANN system satellite- based estimates of tropical rainfall. Bull. Amer. Meteor. Soc., 81, 2035–2046.

Trapp, J. R., D. M. Schultz, A. V. Ryzhkov, and R. L. Holle, 2001: Multiscale structure and evolution of an Oklahoma winter precipitation event. *Mon. Wea. Rev.*, *129*, 486–501,

Turk, F. J., and S. D. Miller, 2005: Toward improving estimates of remotely sensed precipitation with MODIS/AMSR-E blended data techniques. IEEE Trans. *Geosci. Remote Sens*., **43**, 1059–1069.

Vasiloff, S., and co-authors, 2007: Improving QPE and very short term QPF: An initiative for a community-wide integrated approach. *Bull. Amer. Meteor. Soc.,* **88**, 1899-1911.

Young, C. B., B. R. Nelson, A. A. Bradley, J. A. Smith, C. D. Peters-Lidard, A. Kruger, and M. L. Baeck, 1999: An evaluation of NEXRAD precipitation estimates in complex terrain. *J. Geophys. Res.*, **104,** 19691–19703.

Zawadzki, I., 1975: On radar-raingage comparison. *J. Appl. Meteor.,* **14**, 1430–1436.

Zhang, J., K. Howard, and J.J. Gourley, 2005: Constructing three-dimensional multiple radar reflectivity mosaics: Examples of convective storms and stratiform rain echoes. *J. Atmo. and Ocean. Tech.,* **22**, 30–42.

Zhang, J., K. Howard, and et al., 2011a: National Mosaic and Multi-Sensor QPE (NMQ) System: Description, Results, and Future Plans. Bull. Amer. Meteor. Soc., 92, 1321–1338.

Chapter 2 Ground Polarimetric Weather Radar

Polarimetric weather radars have shown significant potential in contributing to the research fields of hydrometeor classification, remote sensing of storm microphysics, quantitative frozen precipitation estimation (Zhang et al, 2010). Polarimetric weather radar can significantly improve QPE by identifying rain echoes from other hydrometeor types and as such is a very powerful tool for PR validation (Chandrasekar et al. 2008). Park et al. (2009) developed a polarimetric radar Hydrometeor Classification Algorithm (HCA) that discerns 10 different classes of radar echo: 1) ground clutter or anomalous propagation, 2) biological scatterers, 3) dry aggregated snow, 4) wet now, 5) crystals of various orientations, 6) graupel, 7) big drops, 8) light and moderate rain, 9) heavy rain, and 10) a mixture of rain and hail. The polarimetric HCA, which includes an automated detection of the bright band, also plays a fundamental role in the polarimetric QPE through a rainfall estimation scheme that varies according to hydrometeor type (Giangrande et al. 2008b).

The objective of this chapter is to illustrate the strengths of ground polarimetric radar as a powerful tool for PR validation and quantitative frozen precipitation estimates. The first part of this chapter was done in my Masters period.

2.1 Cross validation statistic results

2.1.1 Data

In this study, we use the National Severe Storm Laboratory's (NSSL) prototype polarimetric radar for the ongoing upgrade of the NEXRAD national network and NASA's TRMM Precipitation Radar (PR). As research radar, KOUN has been collecting data on an event-by-event, non-continuous basis since 2002. We identify 28

instances (events) that correspond to coincident overpasses by TRMM PR (Fig. 2.1) and then establish the following criteria for comparing data: 1) the maximum time discrepancy between TRMM PR and KOUN observations are less than 3 minutes; 2) TRMM PR and KOUN meteorological echo overlapping areas are larger than 5000 km^2 within 150 km of KOUN; and 3) KOUN data are collected in a conventional volume coverage pattern. Application of these criteria reduces the number of coincident overpasses to 20. The event descriptions and times are listed in Table 2.1. Note that P1 and P2 refer to the first and second coincident overpass on the same day. The sixth column lists a subjective quality control flag for each event. Comments supplied here mention details such that the TRMM overpass has no bright band detected during event 10 because of intense convection lacking stratiform precipitation, but the reflectivity product has good quality. There are two additional cases (events 11 and 15) that have meteorological echoes located at far range from KOUN, which will yield greater uncertainty in the KOUN measurements.

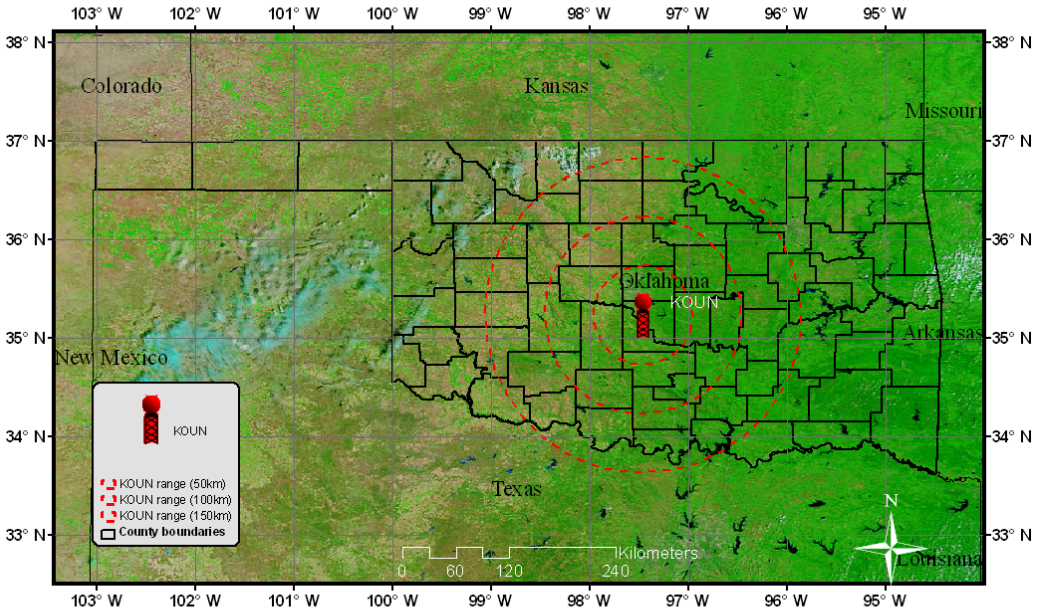

Figure 2.1 Study region showing KOUN location and 50km, 100km and 150km range rings.

Table 1. Description of events used in PR-KOUN comparisons. Times are in UTC.

Event Number	Events/Case study	Description	TRMM Time	KOUN Time	Quality Control Flag
1	May. 13, 2005	MCS	07:23:37-07:26:35	07:23:10-07:28:55	√
2	Oct. 6, 2005(P1)	Widespread rain	04:55:03-04:58:01	04:53:11-04:59:36	√
3	Oct. 6, 2005(P2)	Widespread rain	06:32:38-06:35:36	06:31:06-06:37:15	√
4	Nov. 30, 2006	Convection, freezing rain, snow (long event)	07:44:08-07:47:06	07:41:22-07:48:50	√
5	Dec. 19, 2006(P1)	Winter storm	21:23:33-21:26:31	21:21:48-21:27:50	√
6	Dec. 19, 2006(P2)	Winter storm	23:01:10-23:04:08	22:59:10-23:04:56	√
7	May. 9, 2007	MCS	00:30:51-00:33:49	00:30:14-00:34:47	√
8	May. 24, 2007(P1)	Intense convective line	14:34:33-14:37:31	14:33:55-14:38:29	√
9	May. 24, 2007(P2)	Intense convective line	16:12:09-16:15:07	16:11:25-16:15:58	√
10	Jun. 14, 2007(P1)	MCS, intense convection	04:52:04-04:55:02	04:51:16-04:55:49	No bright band detected
11	Jun. 14, 2007(P2)	MCS, intense convection	06:29:41-06:32:39	06:28:45-06:33:17	Meteorological echo at far range from KOUN
12	Jun.20, 2007	MCS (LL/TS, widespread)	02:35:16-02:38:13	02:34:35-02:39:08	√
13	Jun.26,2007	MCS	00:18:13-00:21:11	00:17:10-00:21:43	√
14	Jun. 28, 2007(P1)	Scattered showers	21:32:00-21:34:58	21:30:56-21:35:29	√
15	Jun. 28, 2007(P2)	Scattered showers	23:09:37-23:12:35	23:10:46-23:15:18	Meteorological echo at far range from KOUN
16	Jul. 13, 2007	Intense convective line	14:10:36-14:13:34	14:10:02-14:14:34	√
17	Aug. 19, 2007	Tropical Storm Erin	19:13:08-19:16:06	19:12:12-19:16:45	√
18	Jun 9, 2008(P1)	Convective line, stratiform	13:14:56-13:18:16	13:12:21-13:17:09	√
19	Jun 9, 2008(P2)	Convective line, stratiform	14:52:40-14:56:00	14:51:59-15:56:45	√
20	Feb. 11, 2009	Supercells	09:02:57-09:06:11	09:01:56-09:07:02	√

1 Note: √ in quality control flag column indicates good quality of the coincident overpass.

2.1.2 Spaceborne Radar and Ground Radar Matching Methods

Diverse approaches have been developed to match up PR and GR observations. These approaches can be divided into three categories: 1) comparing the maps of echoes and rain rates to calculate how much area of echoes PR lost (Schumacher and Houze 2000), 2) resampling PR and GR data to a common 3-dimensional Cartesian grid centered on the GR site (Anagnostou et al. 2001; Bolen and Chandrasekar 2000; Liao and Meneghini 2009; Wang and Wolff 2009), and 3) matching PR and GR to the same resolution volume by determining the intersection of the individual PR and GR rays (Bolen and Chandrasekar 2003; Morris and Schwaller 2009). The resolution volume matching technique is the algorithm adopted for GPM Ground Validation System Validation Network (VN) Software available on NASA's site (http://opensource.gsfc.nasa.gov/projects/GPM/index.php). Our study uses this software package for matching PR and KOUN reflectivity observations. We select each PR ray and KOUN ray within 150 km range from the KOUN site. By assuming standard atmospheric refraction, we calculate the height above ground where the PR ray intersects the KOUN rays. Also, we calculate the vertical beam width of KOUN and horizontal beam width of PR at this range. Within each PR-KOUN ray intersection, we average all PR bins but perform an inverse distance weighted average of the KOUN bins (see Fig. 2.2). Reflectivity data are averaged in linear units and then convert to dB. See Morris and Schwaller (2009) for additional details on the resolution volume matching technique between PR and GR.

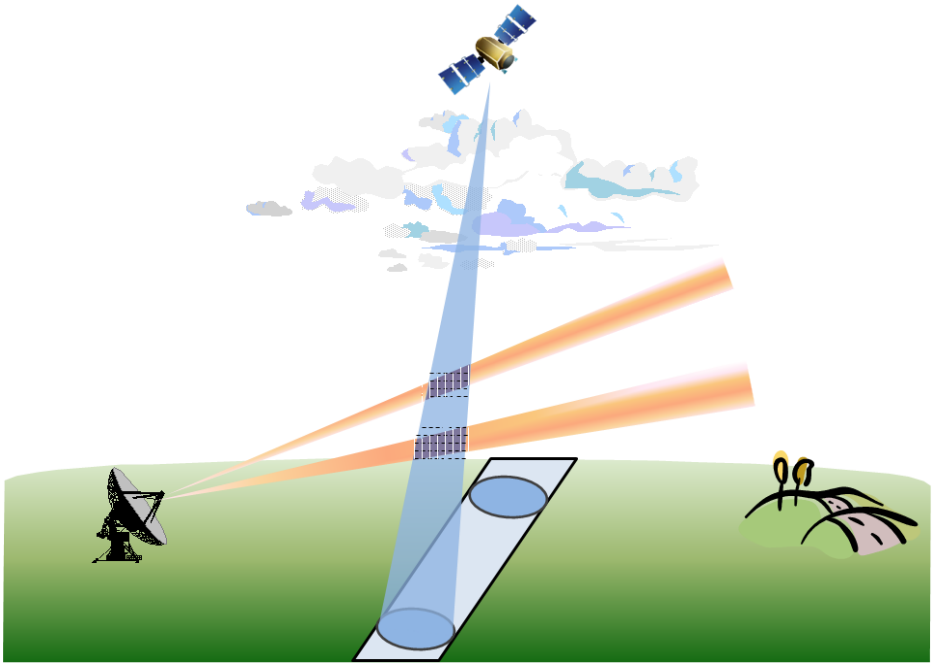

Figure 2.2 Schematic of resolution volume matching technique of ground-based KOUN and space-borne TRMM Precipitation Radar (PR). The purple area shows the intersections between KOUN and PR sweeps.

2.1.3 Cross-Validation indices

We select four statistical indices for the evaluating TRMM PR observations using KOUN as the reference. The Pearson correlation coefficient (CC) is used to assess the agreement between PR and KOUN observations. Relative bias (Bias in %) is used to assess the systematic bias of PR observations. The mean absolute error (MAE) measures the average magnitude of the error. The root mean squared error (RMSE) also measures the average error magnitude but gives greater weight to the larger errors. MAE and RMSE are in units of km for melting layer height comparisons and in dB for reflectivity comparisons.

$$CC = \frac{\sum_{i=1}^{N}(KOUN(i) - \overline{KOUN}) * \sum_{i=1}^{N}(PR(i) - \overline{PR})}{\sqrt{\sum_{i=1}^{N}(KOUN - \overline{KOUN})^2 * \sum_{i=1}^{N}(PR(i) - \overline{PR})^2}}, \quad (2.1)$$

$$bias = \frac{\sum_{i=1}^{N} PR(i) - \sum_{i=1}^{N} KOUN(i)}{\sum_{i=1}^{N} KOUN(i)} * 100, \quad (2.2)$$

$$MAE = \frac{\sum_{i=1}^{N} |PR(i) - KOUN(i)|}{N}, \quad (2.3)$$

$$RMSE = \sqrt{\frac{\sum_{i=1}^{N} |PR(i) - KOUN(i)|^2}{N}}, \quad (2.4)$$

In (1) $\overline{PR}$ and $\overline{KOUN}$ represent the arithmetic mean of the PR and KOUN observations, respectively.

2.1.4 Comparison Results

a. Melting layer height comparisons

Scattering properties detected by polarimetric radar enables the classification of echoes based on their inferred sizes, shapes, phases, and orientations. TRMM PR is capable of retrieving melting layer heights which can then be used to segregate precipitation into frozen, liquid, and mixed categories. Accurate depiction of the melting layer height or bright band is very important for accurate quantitative precipitation estimation, because reflectivity is known to be sensitive to large, wetted hydrometeors within this zone. PR bright band height data are directly extracted from TRMM product 2A23. The melting layer heights are recorded as a function of latitude and longitude and then remapped to a 2D Cartesian grid having 2-km horizontal resolution. For KOUN, the approximate melting layer height for each event is computed by averaging the heights of all bins classified by the HCA as ‘wet snow’ (typical of

radar bright bands) for elevation angles 4° ~ 10° (Giangrande et al. 2008a; Park et al. 2009). The use of radar data exclusively from these higher elevation angles provides a more accurate estimate of the melting layer height than would be possible from data collected at lower elevation angles. These bins are stored in spherical coordinates centered on KOUN as a function of range, azimuth, and elevation angle. The heights of the wet snow bins are then calculated assuming a 4/3 Earth radius model to account for standard beam refraction. Then, the spherical coordinates are remapped to the same 2D Cartesian grid containing the TRMM PR melting layer heights, thus enabling their intercomparison. As such, we do not need to employ the 3D volume matching technique described in section 2b for melting layer heights. It is noted that event 10 is a Mesoscale Convective System (MCS) case with intensive convection but lacking an extensive stratiform region, so no bright band is detected from this event (as noted in Table 2.1). Melting layer height comparisons are thus made for the remaining 19 events.

Figure 2.3 shows results from the melting layer height comparison. The colored data density scatter plot in Fig. 2.3a and the histograms in Fig. 2.3b indicate there is good overall agreement with a relative bias of 5.94% and correlation coefficient of 0.88. Both plots show there is more scatter with the KOUN-detected melting layer heights than from TRMM PR. The wider range of KOUN melting layer heights is caused by the relatively coarse vertical resolution from horizontally scanning platforms compared to the vertical scanning of TRMM PR, which has a height resolution of 0.25 km. For KOUN, the vertical resolution depends on range and elevation angle of beams that intercept the melting layer. We find that TRMM PR typically has a single value for

melting layer height within a nominal 2-km grid cell, whereas KOUN provides a range of heights due to radar beams increasing in altitude with range within the grid cell.

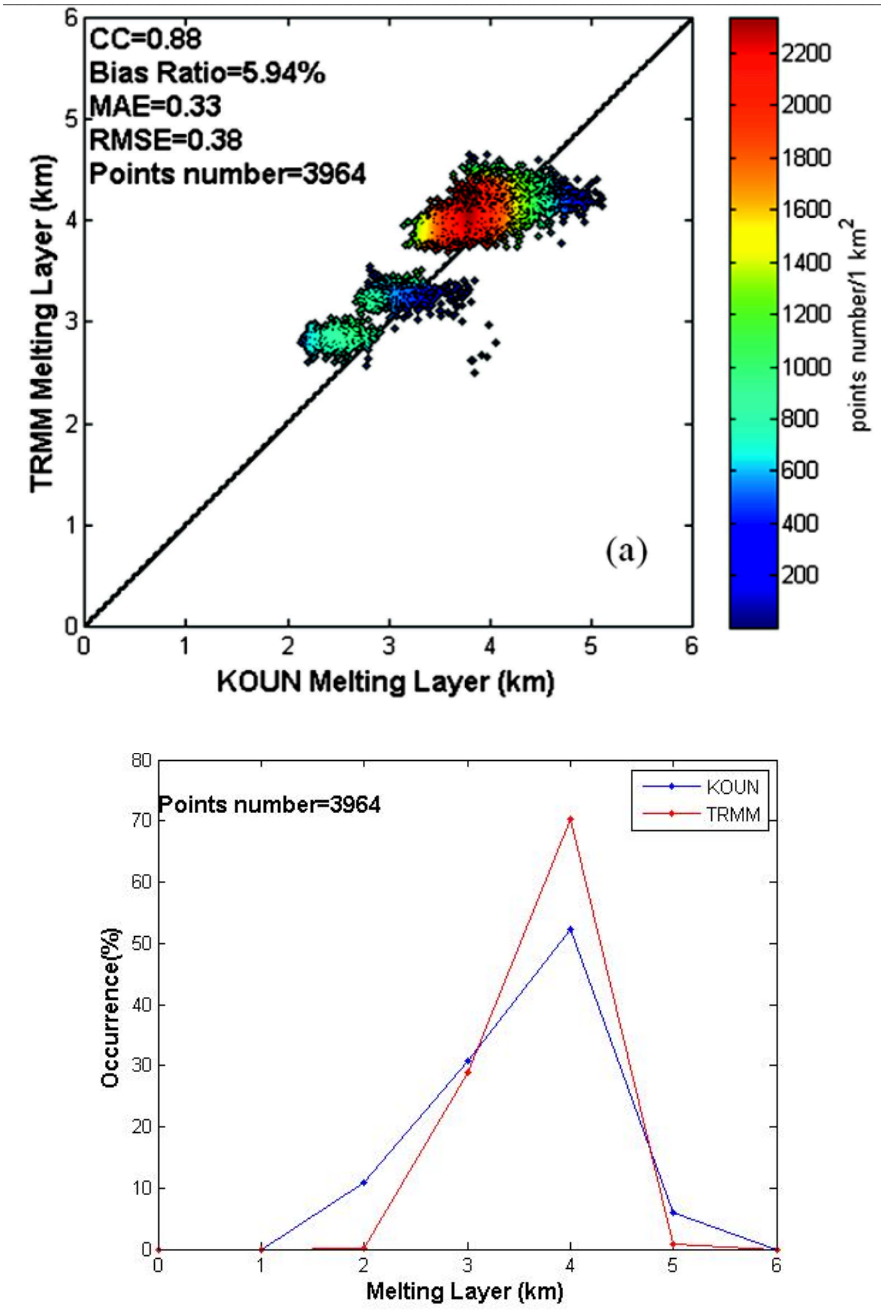

Figure 2.3(a) Scatterplot with colored data density of KOUN and TRMM PR melting layer heights for 19 events. The correlation coefficient, bias ratio, MAE, RMSE, and sample size are shown in the embedded text. (b) Histograms of KOUN and TRMM PR melting layer heights for data shown in Fig. 2.3a.

In order to assess a potential bias between the TRMM PR and KOUN melting layer heights, we compute event-averaged melting layer heights to minimize the impacts due to different scanning orientations. The majority of events shown in Fig. 2.4a lie very close to the one-to-one line, although there are three events where TRMM melting layer heights are 1-1.5 km lower than that detected by KOUN. These points were associated with events 12, 18, and 19, which are all strong convective warm season events during the month of June (see Table 1). In these events, the melting layer is hardly discernible with <12 data pairs. The histogram of the difference in TRMM PR and KOUN melting layer heights in Fig. 2.4b also shows the majority of points are close to 0-km difference, indicating very little to no bias in detected melting layer heights between the two instruments. In summary, the melting layer height comparison reveals differences that are primarily explained from sampling differences between the two instruments rather than systematic offsets that might have pointed to algorithmic errors.

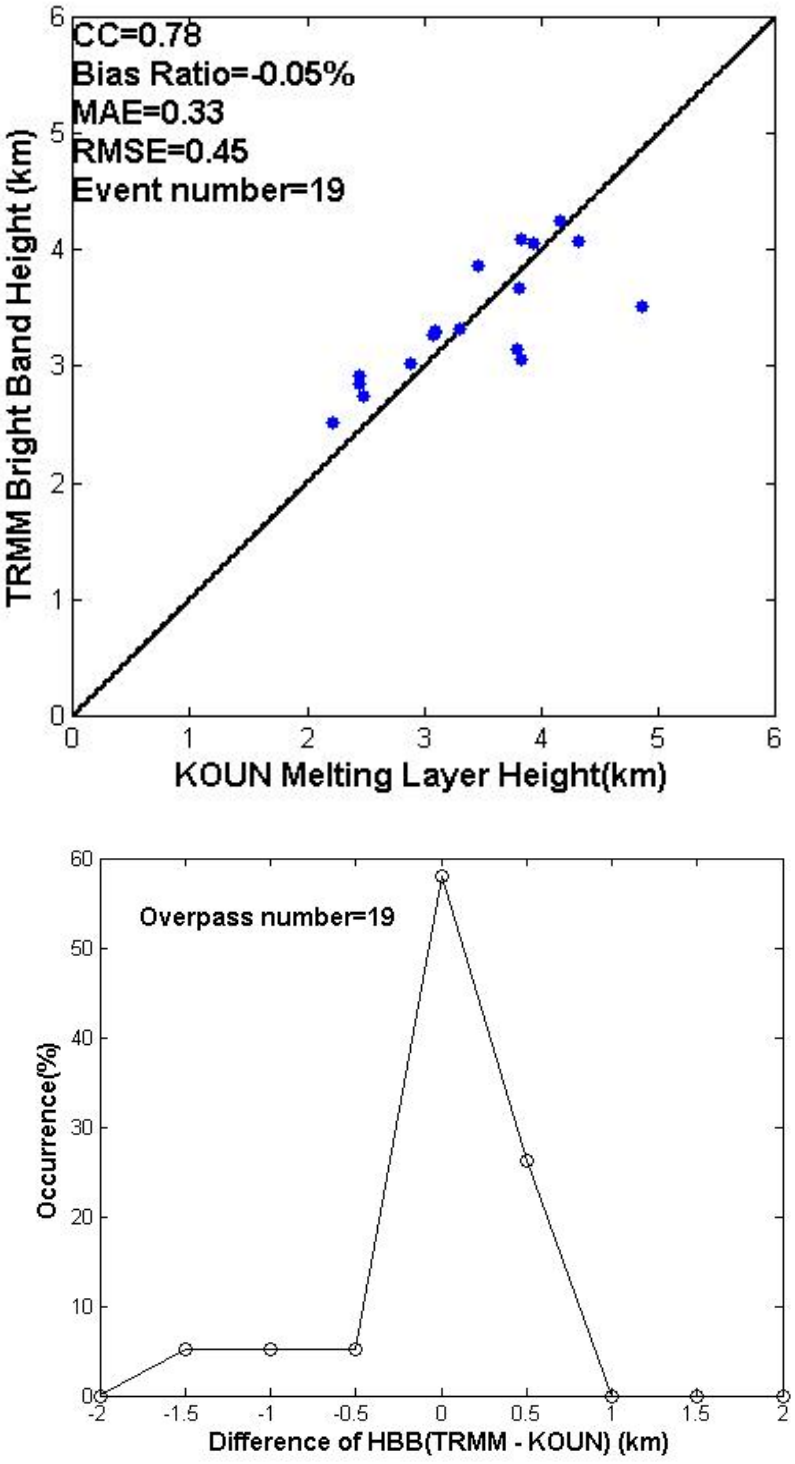

Figure 2.4 Scatterplot of event-averaged melting layer heights from KOUN and TRMM PR. (b) Histogram of melting layer height difference of data shown in Fig. 2.4a.

b. Reflectivity comparisons

Using KOUN as a reference, reflectivity (Z) comparisons between the PR and KOUN can be used to assess the PR's performance. For each event shown in Table 1, KOUN Z data are compared to a neighboring NEXRAD radar in Twin Lakes, OK, KTLX which is known to have a stable calibration to within 1 dB as shown in Ryzhkov et al. (2005) and Giangrande and Ryzhkov (2005). KOUN differential reflectivity (ZDR) is also manually calibrated for each event to within 0.2 dB by examining dry aggregated snow above the melting layer at elevation angles between 4.5 and 6˚. Here, the true or intrinsic ZDR is known to be approximately 0.3 dB. Out of the 20 events shown in Table 1, we compare 18 events which all have sufficient overlapping areas of coincident data coverage. Fig. 2.5 shows the mean reflectivity bias for each event with 95% confidence intervals provided as vertical error bars. Although the biases are within a 2 dB range, there are discrepancies that warrant additional investigation.

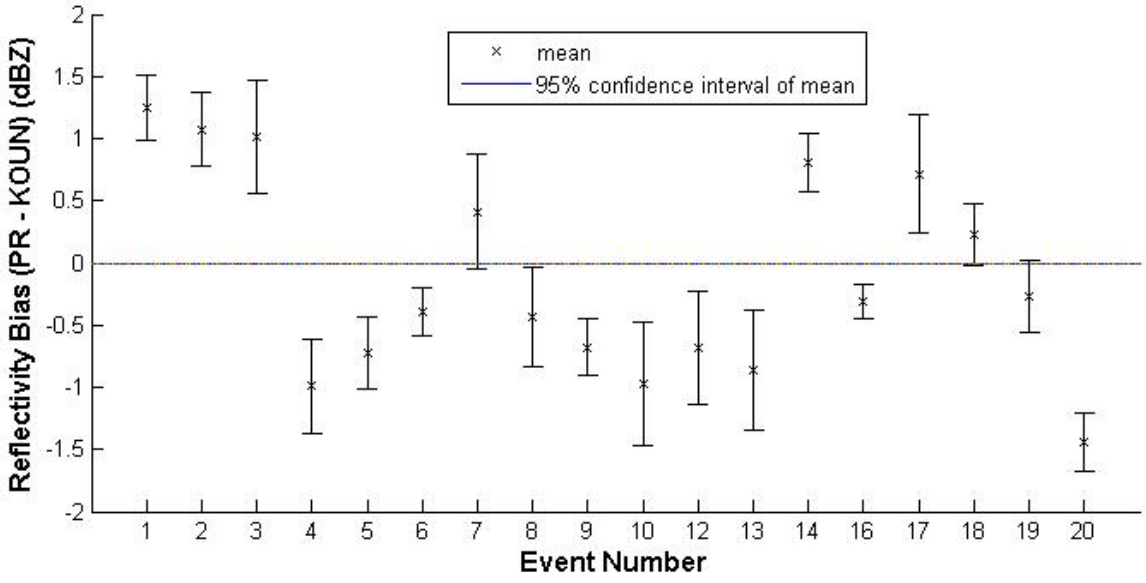

Figure 2.5 Reflectivity bias between PR and KOUN for each event. Event details are provided in Table 2.1.

Figure 2.6 shows reflectivity comparisons between KOUN and TRMM PR subject to subsequently applied quality control procedures. Figures 2.6a and 2.6b show a colored data density scatterplot and histograms for reflectivity data with no quality control. A major advantage of polarimetric radar is its capability of distinguishing non-meteorological from meteorological echoes. Non-meteorological echoes identified by the HCA, which contaminate radar observations, have been removed from the KOUN and PR comparisons in Figs. 2.6c and d. Also, due to PR's low sensitivity of 18 dB or lower (NASDA 1999), only Z >18 dBZ are used in comparing values in Figs. 2.6e and f.

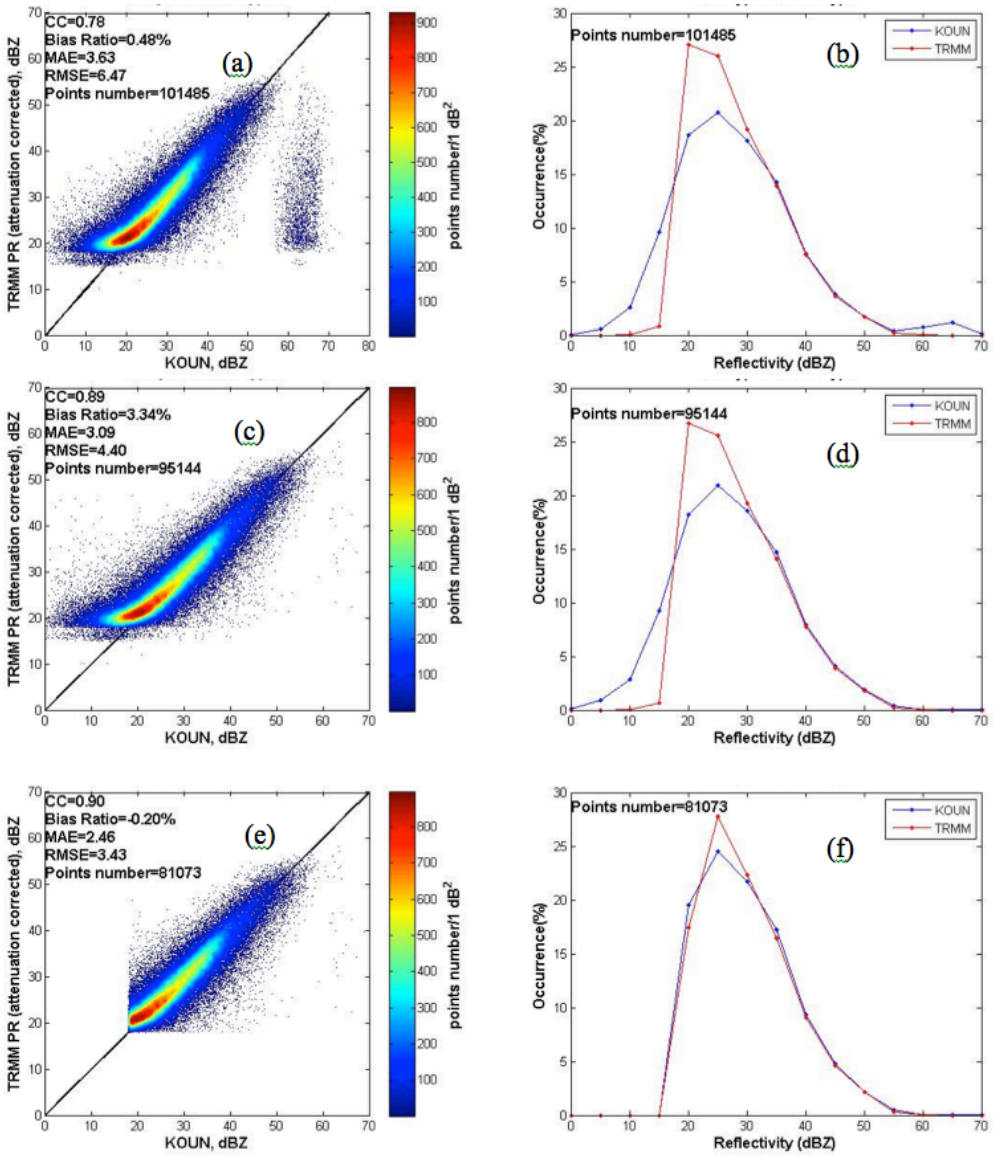

Figure 2.6 Scatterplots with colored data density and histograms of KOUN and TRMM PR reflectivity. (a) and (b) reflectivity and attenuation-corrected PR reflectivity with no additional quality control; (c) and (d) same as (a) and (b) but non-meteorological echoes based on KOUN's hydrometeor classification algorithm (HCA) have been removed; (e) and (f) same as (c) and (d) but applied a minimum18 dB*Z* threshold.

We can see substantial improvements in the reflectivity comparisons following the removal of non-meteorological echoes and application of the 18 dBZ threshold in the plots and statistics. The CC improves from 0.78 to 0.89 following removal of non-meteorological echoes, while the RMSE decreases from 6.47 to 4.40 dB. In Fig. 2.6a,

there is a separate cluster of points for which KOUN shows values of Z from 55 to 70 corresponding to a much larger range of PR Z values. These points are associated with non-meteorological KOUN echoes, most likely due to ground clutter. In Fig. 2.6c, this cluster has been effectively removed following application of the HCA, with only a few points left. The histogram in Fig. 2.6d no longer contains the discrepancy in the occurrence of Z in the range of 55-70 dBZ.

The best results are shown in Fig. 2.6e and f with both non-meteorological echoes removed and the 18-dBZ threshold applied. Although remaining differences are slight, about as small as can be expected between two independent remote-sensing instruments, it is possible that remaining discrepancies could be related to difficult-to-discern random factors, such as spatial and temporal volume mismatches or non-uniform beam-filling effects (NUBF). It is also possible that the discrepancies may be due to systematic, non-random effects such as errors in the PR attenuation correction scheme and differences in backscattered radiation between PR and KOUN at 2.17- and 10.7-cm wavelength, respectively (Bolen and Chandrasekar 2000; Liao and Meneghini 2009; Schumacher and Houze 2000; Wang and Wolff 2009). These potential non-random factors are elucidated in following section with the aid of HCA results.

2.2 HCA analysis

Non-Rayleigh scattering effects are significant for TRMM PR at a frequency of 13.8 GHz. But for KOUN S-band radar, nearly all hydrometeors in our dataset satisfy the Rayleigh approximation. Due to different backscattering cross sections measured by the radars, PR Z can be up to 2 dB higher than KOUN for rain measurements in the range of 40-50 dBZ (Bolen and Chandrasekar 2000). However, other types of

hydrometeors (e.g., dry aggregated snow, wet snow, mixture of rain and hail) have different backscattering cross sections at Ku and S band potentially resulting in systematic discrepancies between PR and KOUN observations.

The difference in Z at S and Ku bands for different hydrometeors is simulated and shown in Fig. 2.7. The radar reflectivity factor Z is given as

$$Z = \frac{\lambda^4}{\pi^5 |K_w|^2} \int_0^\infty N(D)\sigma_b dD, \tag{2.5}$$

where Kw=(m2-1)/(m2+2) and m is the complex refractive index of water (Doviak and Zrnic, 1993). We choose 0.93 for |Kw|2. N(D) is the particle size distribution, which is simulated by mono dispersion model using number concentration of 1/m3. The σb is the back scattering cross section of hydrometeors which is simulated using the T-matrix method (Waterman 1971, Vivekanandan et al. 1991) at different radar wavelengths λ. As seen in Fig. 2.7, Z values at Ku and S band are approximately equal for all hydrometeor types for Z < 30 dBZ, with the exception of wet snow, which has lower Z at Ku band. As Z increases above 30 dBZ, all hydrometeors except liquid water have lower reflectivity at Ku band because of non-Raleigh scattering effect. For liquid water, the simulated reflectivity gradually deviates for Z in the range of 40-50 dBZ, which conforms to results shown in Bolen and Chandrasekar (2000). Beyond 50 dBZ, the deviation becomes more severe. Liao and Meneghini (2009) also show that PR underestimates in heavy rain.

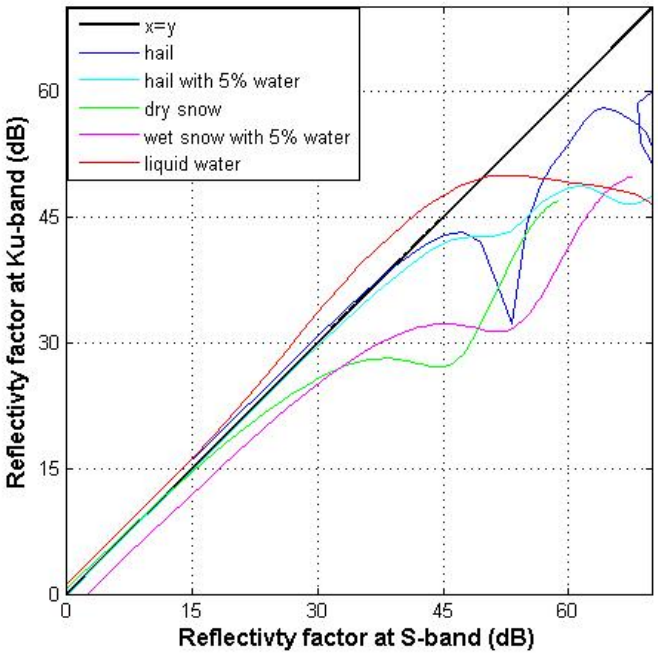

Figure 2.7 Relationships between reflectivity factors at S and Ku bands for liquid water, hail and dry snow. Backscatter cross sections are simulated using T-matrix method at S and Ku bands, where reflectivity calculations assume a mono-dispersed drop size distribution.

The HCA discerns eight different classes of hydrometeors based on polarimetric characteristics of the radar echoes. The previous analysis indicates PR and KOUN retrieve comparable melting layer heights, thus we can confidently classify different hydrometeor classes exclusively based on the KOUN HCA. During the PR-KOUN volume matching procedure, we calculate the percentage of each hydrometeor class in each volume. The final hydrometeor class is assigned to a bin if a particular hydrometeor type has the highest percentage in a volume and the percentage exceeds 50%. We then group all KOUN-PR reflectivity data with respect to the different hydrometeor types.

The reflectivity comparisons classified by different hydrometeor types are shown in Fig. 2.8. The scatterplots with colored data density and histograms for reflectivity in rain/hail mixture, wet snow, graupel, and heavy rain show they have an obvious negative bias at Ku band, which is in good qualitative agreement with simulated results shown in Fig. 2.7. The reflectivity comparison of light and moderate rain types (Figs. 2.8f1 and 2.8f2) also conforms to expectations shown in Fig. 2.7 with very little bias between Ku- and S-band reflectivity. However, for dry snow, simulations indicate PR Z should be less then KOUN especially for values of $Z > 25$ dBZ. Figures 2.8g1 and 2.8g2 do not reveal this discrepancy in the observations with a relative bias of only 1.92%. Liao and Meneghini (2009) also show that simulated reflectivity at S band should be higher than at Ku band for snow by assuming the Gunn-Marshall (1958) snow particle-size distribution with a snow density of 0.3 g cm-3. However, their quantitative bias for snow Z between S-band and Ku-band does not clearly agree with the expected bias shown in the simulation. It is possible that assumptions used in the simulations such as the dry snow density and particle size distribution differ from observations, an area inviting future research.

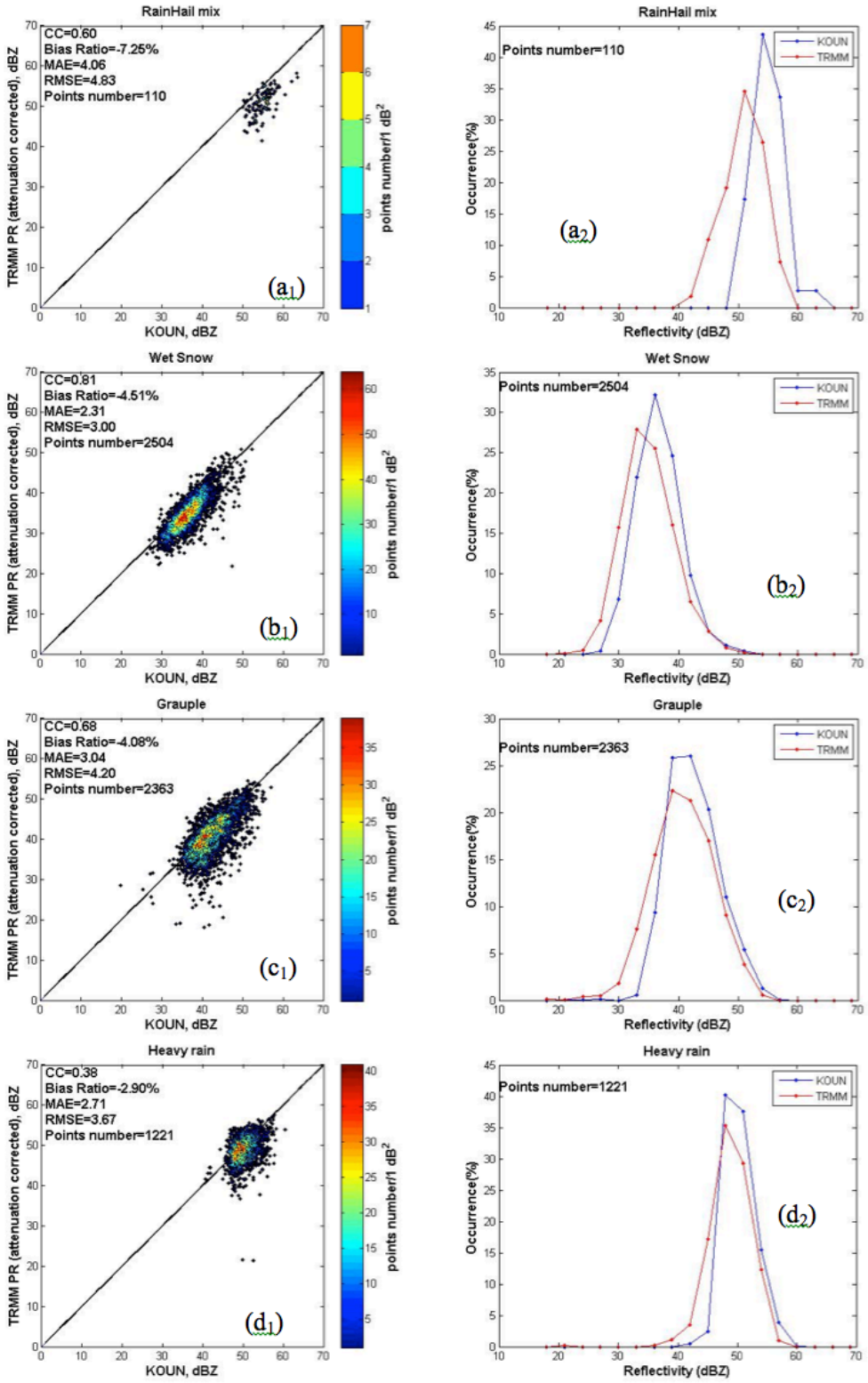
RainHail mix
CC=0.60
Bias Ratio=-7.25%
MAE=4.06
RMSE=4.83
Points number=110
TRMM PR (attenuation corrected), dBZ
KOUN, dBZ
points number/1 dB²
(a1)
RainHail mix
Points number=110
KOUN
TRMM
Occurrence(%)
Reflectivity (dBZ)
(a2)
Wet Snow
CC=0.81
Bias Ratio=-4.51%
MAE=2.31
RMSE=3.00
Points number=2504
TRMM PR (attenuation corrected), dBZ
KOUN, dBZ
points number/1 dB²
(b1)
Wet Snow
Points number=2504
KOUN
TRMM
Occurrence(%)
Reflectivity (dBZ)
(b2)
Grauple
CC=0.68
Bias Ratio=-4.08%
MAE=3.04
RMSE=4.20
Points number=2363
TRMM PR (attenuation corrected), dBZ
KOUN, dBZ
points number/1 dB²
(c1)
Grauple
Points number=2363
KOUN
TRMM
Occurrence(%)
Reflectivity (dBZ)
(c2)
Heavy rain
CC=0.38
Bias Ratio=-2.90%
MAE=2.71
RMSE=3.67
Points number=1221
TRMM PR (attenuation corrected), dBZ
KOUN, dBZ
points number/1 dB²
(d1)
Heavy rain
Points number=1221
KOUN
TRMM
Occurrence(%)
Reflectivity (dBZ)
(d2)

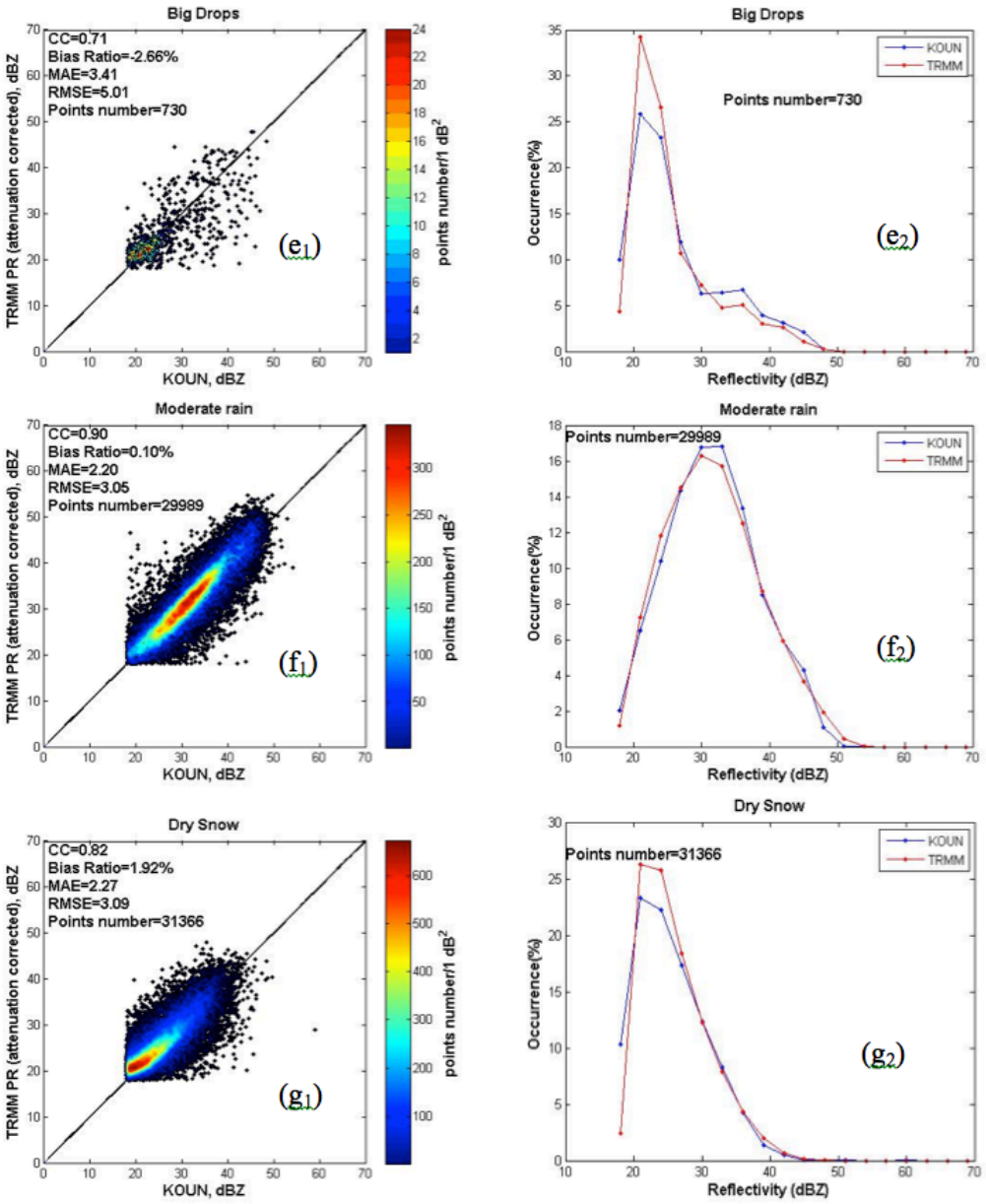

Figure 2.8 Scatterplots with colored data density in the first column and histograms in the second column for reflectivity observed for different hydrometeors as determined from KOUN HCA: (row a) rain/hail mix, (row b) wet snow, (row c) graupel, (row d) heavy rain, (row e) big drops, (row f) moderate rain, and (row g) dry snow.

A simple bar chart in Fig. 2.9 gives an overview of the PR reflectivity bias as a function of the different hydrometeor types. Rain/hail mixture, wet snow, graupel, heavy rain, and big drops show the largest negative biases, respectively, while moderate

rain observations are unbiased and dry snow indicates a positive PR bias. Differences in scattering between Ku and S band are the main reason to explain the discrepancies, as confirmed in the T-matrix simulations. Simulating multi-frequency reflectivity values for dry snow is an area inviting future research.

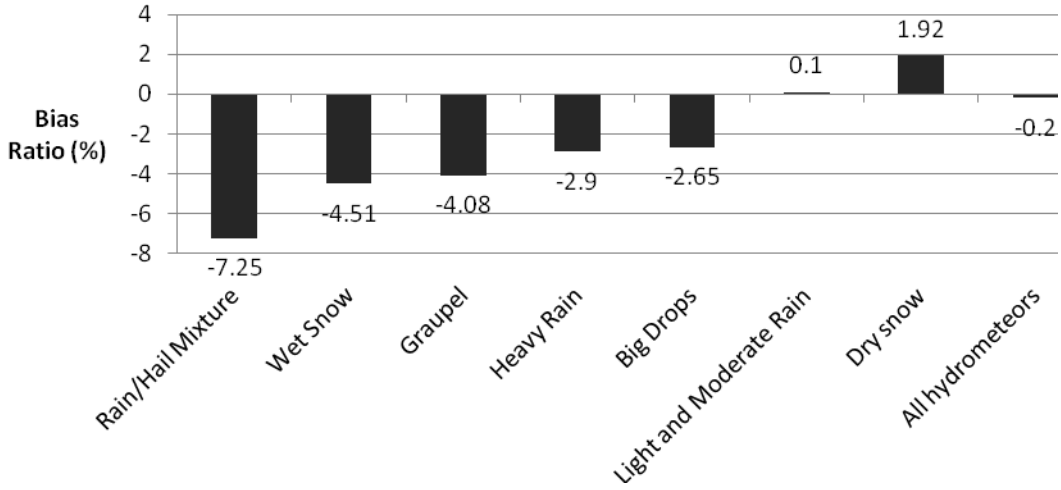

Figure 2.9 Bias (%) of TRMM PR reflectivity observations relative to KOUN for different hydrometeor types as discriminated by the dual-polarization HCA

A method to identify potential attenuation correction errors applied to TRMM PR reflectivity data is to compare vertical profiles of reflectivity from PR to KOUN, where KOUN is again the reference. A hybrid correction scheme combining the surface reference technique and the Hitschfeld and Bordan method is used in the PR attenuation correction (Iguchi et al. 2000). The magnitude of the correction increases with path length, thus it is informative to compare reflectivity profiles in the vertical, path-integrated direction. Figure 2.10 shows the profiles of 18 overpasses for convective, stratiform, and all rain types combined. The rain type classification is made exclusively according to PR observations, which is from the TRMM 2A23 product. To reveal the

magnitude of estimated attenuation losses, the PR measured reflectivity (Zm; uncorrected reflectivity from 1C21) is shown in the profiles along with corrected PR reflectivity (Zc; attenuation corrected reflectivity from 2A25) and the reference reflectivity from the KOUN ground radar (ZG). The profiles are computed at 9 vertical layers from 1.5 – 13.5 km with 1.5-km spacing for values of Z >18 dBZ. As the path length increases from the top down in Fig. 2.10a, the gap between the Zm and Zc curves gradually increases which illustrates PR suffers significant attenuation losses. In comparing Zc to ZG in stratiform rain from 3 - 4.5 km, we see there is a large discrepancy in the presumed melting layer (Fig. 2.10b). The hydrometeors within the melting layer are primarily wet snow and from results shown in Fig. 2.9 we can see TRMM PR underestimates S-band reflectivity due to the effect of non-Rayleigh scattering. But at the lowest height of 1.5 km, Zc and ZG converge indicating the attenuation correction for stratiform rain performs well at the surface. The same convergence of Zc and ZG values is also noted in convective precipitation at the surface level. As shown in Fig. 2.10c for all rain types combined, due to mismatches in resolution volumes and/or different back scatter cross sections between PR and KOUN, the reflectivity profiles have slight discrepancies, but at the surface level the measurements agree quite well. To summarize, our analysis shows close correspondence between corrected TRMM PR near-surface reflectivity observations and KOUN data, thus indicating no systematic biases were caused by the TRMM attenuation correction procedures.

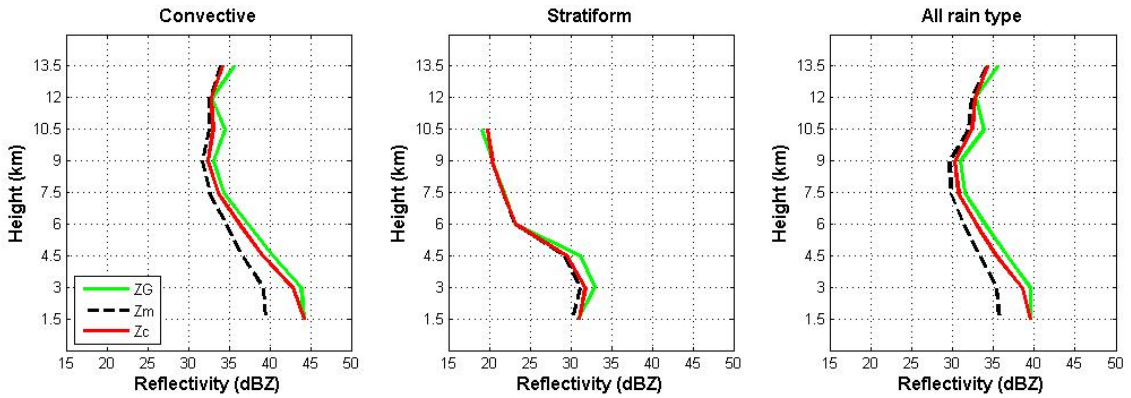

Figure 2.10 Mean vertical reflectivity profiles for (a) convective, (b) stratiform, and (c) all rain types as determined by TRMM 2A23. ZG is reflectivity from KOUN, Zm is measured reflectivity from TRMM 1C21 with no attenuation correction, and Zc is attenuation-corrected TRMM 2A25.

2.3 Snow estimation by ground polarimetric radar

The polarimetric weather radar not only significantly improves quantitative liquid precipitation estimation, but also a potential powerful tool for frozen precipitation estimation. This section discusses estimation of Snow Water Equivalent (SWE) from the polarimetric weather radar measurements.

2.3.1 Motivation

Snow is a significant contributor to high-altitude/latitude regional water budgets, and thus is of critical importance to our society. Snow can also cause potentially hazardous driving conditions, and rapidly melting snowpack may result in flooding. Despite its importance, accurate estimation of snow remains challenging. Snow gauges are assumed to provide the 'ground truth' of snow measurements and the measurement errors are often ignored for automated systems; however, the measurement errors frequently range from 20% to 50% due to undercatch in windy conditions (Rasmussen,

et al. 2012). Snow Water Equivalent (SWE) measured at ground has significant errors and representative issues, perhaps as big as the first-guess radar estimates.

For large-scale weather monitoring and climate studies, remote sensing of snow is highly desirable but is even more challenging. The installation of the current Weather Surveillance Radar – 1988 Doppler (WSR-88D) network (NEXRAD) has dramatically increased our ability to accurately estimate liquid precipitation data over large spatial domains. In conventional precipitation estimation radar reflectivity factor Z is directly related to the precipitation rate R. In general, liquid precipitation events are studied more thoroughly than frozen precipitation events. Dramatic variability in snowflake physical properties and scattering properties introduce high uncertainties in Z-Snowfall rate relations. The traditional Z-S relation derivation uses a single wavelength much longer than the snowflake particle sizes so that the scattering is within Rayleigh scattering region. And the traditional approaches can be roughly divided to two categories, one easier way is to directly relate radar reflectivity measurements to the observed snowfall rate from nearby snow gauges. Super and Holroyd, (1998) developed Snow Accumulation Algorithm (SAA) for WSR-88D radars dry snow measurements by comparing the snow gauge accumulation. The algorithm is an equation of $Z=aS^b$. S is the liquid water equivalent (mm/h). Different a,b values are assigned along with a correction factor adjusting radar range-dependent errors. The other approach is linking Snowfall rate and radar reflectivity factor by considering snow Particle Size Distributions (PSD). Sekhon and Srivastava (1970) proposed a relation of Z and S by considering the measured snow PSDs. The Z-S relation the NMQ system adopts is

$Z=75R^2$, which is from the "Guidance on selecting Z-R relationships" reported in Radar Operations Center (1999).

Table 2. Summary of Z(S) relations for dry snow listed in literature and utilized by the WSR-88D network in the US.

Source	Z(S) relation for dry snow
Gunn and Marshall 1958	$Z = 448\ S^2$
Sekhon and Srivastava 1970	$Z = 399\ S^{2.21}$
Ohtake and Henmi 1970	$Z = 739\ S^{1.7}$
Puhakka 1975	$Z = 235\ S^2$
Koistinen et al. 2003	$Z = 400\ S^2$
Huang et al. 2010	$Z = (106 – 305)\ S^{1.11 – 1.92}$
Szyrmer and Zawadzki 2010	$Z = 494\ S^{1.44}$
WSR-88D, Northeast	$Z = 120\ S^2$
WSR-88D, Great Lakes	$Z = 180\ S^2$
WSR-88D, North Plains / Upper Midwest	$Z = 180\ S^2$
WSR-88D, High Plains	$Z = 130\ S^2$
WSR-88D, Inter-mountain West	$Z = 40\ S^2$
WSR-88D, Sierra Nevada	$Z = 222\ S^2$

A variety of Z-S relations have been derived. Ryzhkov et al (2015), provides a table showing different Z-S relationships. Considering the complexity of snow habits, it is not surprising to have many significantly different Z-R relations from storm to storm. Generally, in $Z=aS^b$, parameter b is relatively stable range around1.11~2, while parameter a has a dramatically large variation in value from 40 to 739. Large number of

studies (e.g., Thurai et al., 2007; Zhang et al, 2011) have investigated the characteristics of the size distribution using polarimetric radars or dual frequency radar measurements.

A dual (or triple) frequency approach is another way to improve radar retrievals. By comparing in situ observations and radar measurements, clear improvements are observed by using dual frequency techniques. Gosset and Sauvageot (1992) utilized a dual-wavelength method to differentiate supercooled water from ice by using a wavelength couple of 3.2 cm and 0.86 cm. By using concurrent 35- and 94- GHz radars located at Chilbolton, England, Holgan et al. (2000) measured crystal size in cirrus clouds and found that density is the most important uncertainty source. A lot of dual frequency approaches combine spaceborne radar sensors and ground based radar sensors to allow one frequency in Rayleigh regime (S, C, X band) and the other in the Mie regime(e.g. Ku, Ka in GPM, and W band in Cloudsat).

Due to these dynamic factors, applying a single Z-S rate relationship to retrieve snow rate can result in large estimation errors. Since 2013 the NEXRAD network has been upgraded with dual-polarization technology. Compared to single–polarized radars, the polarimetric technology reduces fundamental and limiting errors in reflectivity-to-precipitation rate conversion by accounting for hydrometeor phase (liquid, melting, or frozen) and changes in particle size distributions within individual storm systems and between meteorological regimes (Bringi and Chandrasekar, 2001; Ryzhkov, et al. 2005; Zhang et al. 2011). The polarimetric signatures of snow provide valuable insights into its microphysical processes/properties and thus can potentially improve radar snow estimation. To link the polarimetric radar signatures aloft and precipitation near the

surface, scans from the "Range-Height Indicator" can be used to show the vertical structure of a precipitation system but only in selected azimuthal directions. To represent the general structure of the precipitation system and reduce the noisiness of the key polarimetric variables ZDR, Phidp, and RhoHV, Kumjian et al. (2013) and Ryzhkov et al. (2013) suggest azimuthal averaging of polarimetric variables at high elevation angles to obtain the so-called high-resolution quasi-vertical profiles (QVPs) of polarimetric variables.

Given both the limitations of snow measurements and the capabilities offered by polarimetric radars, we propose a novel snow retrieval method, which utilizes high polarimetric radar data at high elevation angles to estimate the liquid water equivalent of dry snow above the freezing level and then assumes that the rain rate near the surface is equal to the liquid water equivalent of dry snow aloft. This assumption based on hypothesis of the mass conservation (confirmed by Zhang et al. 2012) is appropriate for situations where depositional growth of snow above the melting layer or evaporation of rain below it is not significant. Our procedure is to minimize the difference between (i) the calculated snow water equivalent from the reflectivity measured by the WSR-88D ground radar and (ii) the measured hourly rain accumulation from rain gauges on ground. Moreover, we develop the Z-SWE relations for snow generated by different microphysical processes aided by polarimetric radar signals.

2.3.4 Methodology

a. Generate QVP of the polarimetric radar variables from selected events

Long duration stratiform raining events with melting layers below (this assumes the surface precipitation liquid) 2.5 km will be selected. Sounding data will be used to

filter out events with low near-surface relative humidity in order to ensure the mass flux conservation assumption (i.e. limited evaporation) holds. The quasi-vertical profiles (QVPs) of the polarimetric radar variables used in this study are obtained by azimuthal averaging of the radar data collected during standard conical scans at antenna elevation angles at 19.5°. The high elevation ensures a high vertical resolution and minimizes radar beam broadening (Ryzhkov et al. 2015). Quality control of the polarimetric data will be performed before calculating the QVPs in order to remove non-meteorological radar echoes such as ground clutter, biological scattering, etc. All reflectivity measurements less than -10 dBZ are removed before averaging, also only correlation coefficient greater than 0.9 are calculated to generate QVPs.

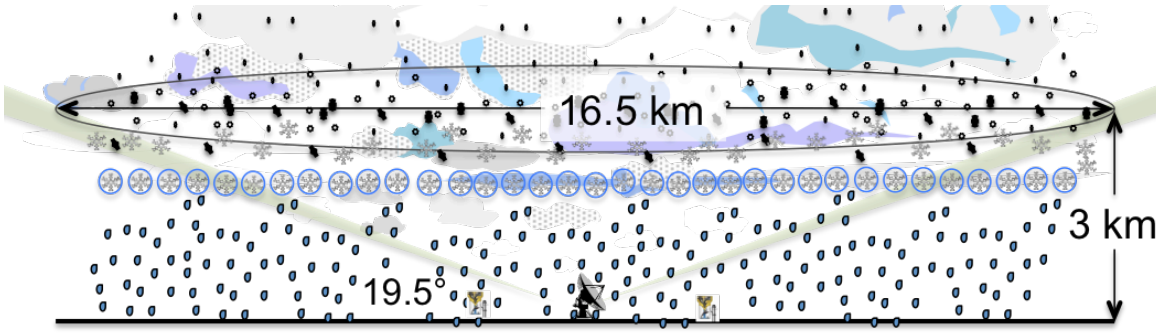

Figure 2.11. Conical volume representing azimuthally averaged quasi-vertical profiles of polarimetric radar variables in the dry snow region. The radar variables will be related to rain gauge measurements on the ground to derive Z-SWE relation. The parameters in Z-SWE relation will be constrained by dual-polarimetric data and environmental variables obtained from sounding data or other remote sensors.

b. Calibrate the Z-SWE relationship

As discussed above, in Z-SWE relation, $S=\alpha Z^{\beta}$, β value is relatively stable, around 0.64. So we fix β as 0.64 and calibrate α value. The parameter α is calibrated to minimize the difference between calculated SWE from the radar reflectivity and the matched rain gauge measurements.

The polarimetric radar measurements and gauge measurements are matched up spatially and temporally. The azimuthally averaged QVPs represent observations from a conical volume (Fig. 2.11). The values of QVPs at a specific height indicate the averaged measurements from that height. As illustrated in Fig. 2.11, QVPs at 3 km height are the averaged measurements from the circle with a diameter of 16.5 km. To match radar measurements with gauges, we also average all gauge measurements located within the 16.5km-diameter circle. The radar and gauge observations must also be temporally matched/scaled because QVPs represent quasi-instantaneous observations while gauge measurements are hourly based. To temporally scale the two measurements, we calculate hourly averages of the QVPs. One assumed Z-S relation, e.g., $S=0.01Z^{0.63}$, is applied at the radar observation scale, and then the instantaneous snow rates are accumulated to hourly scale. We use the rain gauge measurements as the reference to calculate the bias of SWE in ground radar-based estimation. After determining the estimation bias, we then calibrate parameter α at each pixel on QVPs.

2.3.3 Case study results

a. QVP examples

The QVPs of Z, Z_{DR}, ρ_{hv}, and Φ_{DP} generated from the KCLE WSR-88D radar (Cleveland, Ohio) data collected at elevations of 19.5° on Dec. 5, 2014 to Dec. 6, 2014,

totally 19 hours. Figure 2.12 from MRMS system provides the storm and the environmental information of this event. The Fig. 2.12(a) is the hourly radar rainfall accumulation which illustrates a massive rainfall event with an average rainfall rate around 0.15 inch/hr. The surface precipitation type is stratiform according to MRMS Precipitation Type product (Fig. XXc). Fig. XXb shows the freezing level height from the Rapid Refresh (RAP) numerical weather model is about 2.5 km around KCLE radar, which means the precipitation at surface level is liquid rain. The Fig. 2.12d is the relative humidity from Pittsburgh sounding observations east of KCLE radar. The relative humidity is greater than 90% from surface up to 6.5 km height. The high relative humidity depresses the evaporation rate thus ensures the mass conservation assumption.

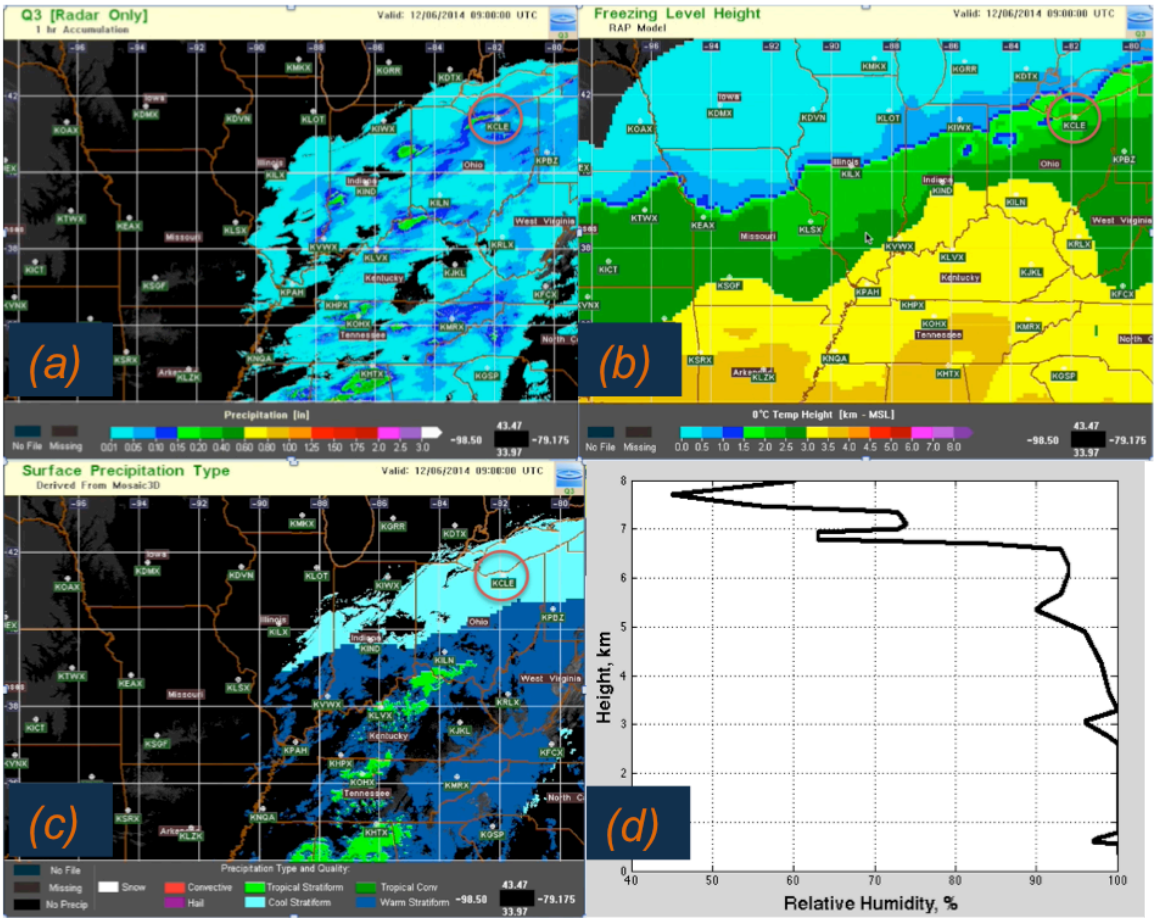

Figure 2.12. Dec. 5, 2014 event information from MRMS. (a) Hourly accumulation of rainfall estimated by ground radars; (b) Freezing level height estimated by RAP model; (c) Surface Precipitation Type; (d) Relative Humidity from Pittsburg Sounding observation station.

Fig. 2.13 illustrates the QVP evolution during 19 hours and reveals the internal structure of the storm. Notable are abrupt variations of the height of the melting layer with time marked by enhanced Z, Z_{DR}, and Φ_{DP} as well as depressed ρ_{hv}, which can be effectively monitored using this height vs time format. In the first several hours, melting layer reveals clear 'fingerprints' as detected by polarimetric variables, Z_{DR} and ρ_{hv} is not captured by the QVPs of Z. The polarimetric variables are more sensitive to the phase change caused by the hydrometeor melting process. Analysis of the thermodynamic

output of the RAP shown in Fig. 2.12b reveals that the freezing level height at 9:00 UTC on Dec. 6, 2014 is around 2.5 km, which is consistent with the freezing level height revealed by radar QVPs . After 0500UTC on Dec. 6, the storm top height increases as melting layer height decreases compared to the first half time of the storm. Deeper storm is associated with more active ice nucleation, which would induce more precipitation. The QVP clearly exhibits the episode of riming associated with weak embedded convection at the second half time of the storm. All three attributes of riming are evident in the QVP plots: enhanced Z, depressed Z_{DR} above the freezing level, and downward excursion of the melting layer in terms of Z_{DR} and ρ_{hv}.

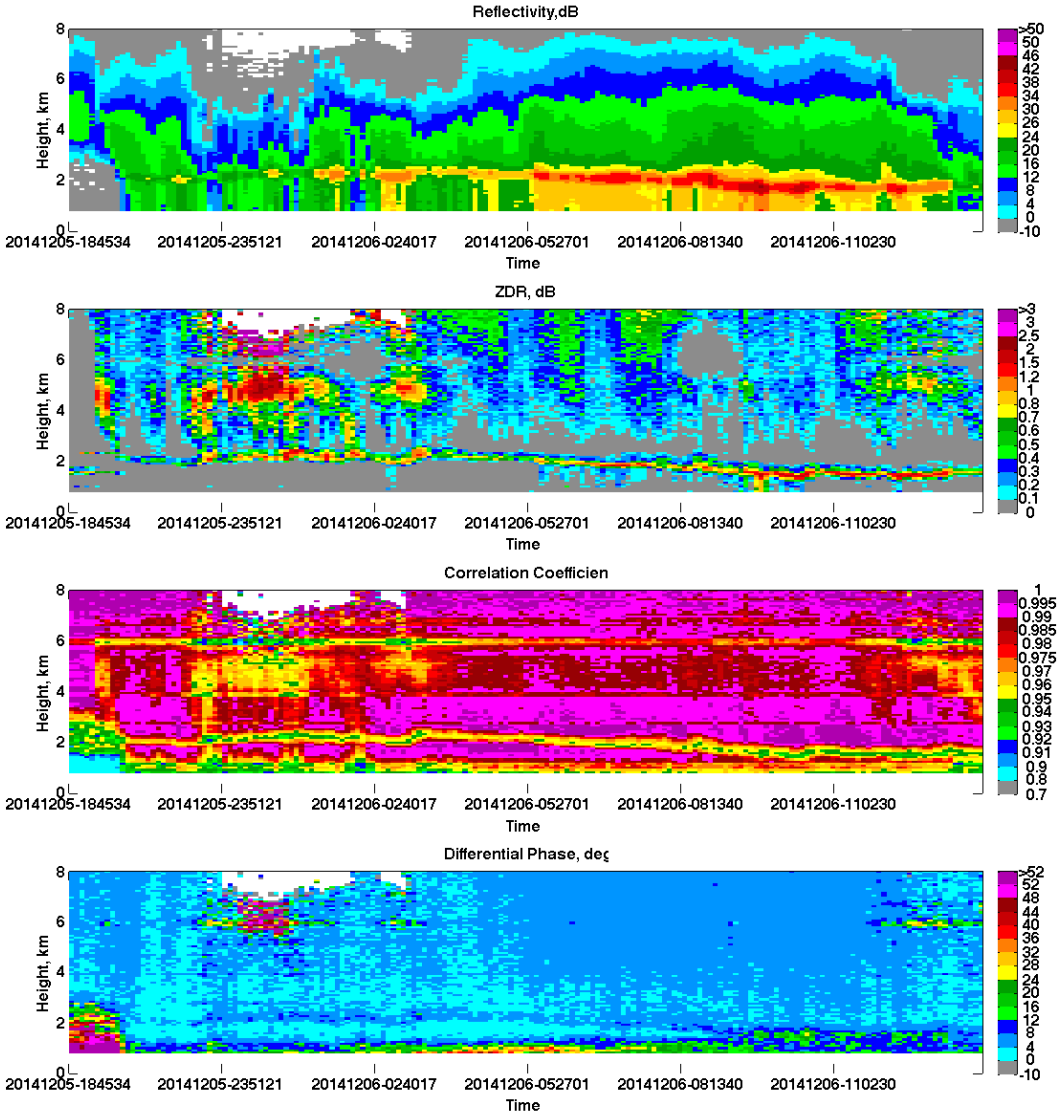

Figure 2.13. The height vs time representation of quasi-vertical profiles of Z, Z_{DR}, ρ_{hv}, and Φ_{DP} retrieved from the KCLE WSR-88D radar data collected at elevation 19.5° during the stratiform rain event in Cleveland, OH on 5 Dec 2014 and 6 Dec. 2014.

b. Evaluation of SWE estimated from current MRMS Z-SWE relation

The Z-SWE relation the MRMS system adopts is $Z=75R^2$, which is from the "Guidance on selecting Z-R relationships" reported in Radar Operations Center (1999). The MRMS system (http://nmq.ou.edu) is fully automated and has been operational

since 2006 by incorporating data from more than 140 WSR-88D radars and about 31 Canadian C-band weather radars within the latitude band (20N – 55N) of North America, thereinafter MRMS region (Zhang et al. 2011). Q3 (Next-generation QPE), a key component in the MRMS system, performs automated precipitation classification and generates a suite of mosaic QPE products at 1-km horizontal resolution and 5-minute update cycle including hybrid scan reflectivity (HSR), surface precipitation phase, rain/snow rate, etc. The snow rates are obtained by applying $Z=75R^2$ to the mosaicked HSR field at eat snow grid point. The evaluation of snow estimates in MRMS has been conducted by validating against snow gauges on ground. However, snow gauges have dramatic uncertainty in measuring snow, and are sparse and unevenly distributed, the evaluation of MRMS snowfall product with snow gauge measurements as a reference is inaccurate. In this study, we calculate the SWE by applying $Z=75R^2$ (or $S=0.1155\ Z^{0.5}$) to QVP of reflectivity above the melting layer, accumulate the calculated snow water rate to hourly and compare the hourly accumulated radar SWE to the matched rain gauge measurements. Fig. 2.14 shows the height vs. time representation of calculated radar SWE for this event. The colored circles plotted on 3 km and 4 km indicate the rain gauge measurements on ground from one HADS gauge for this event. For the first four hours, no rain indicated by rain gauge measurements due to the evaporation under the melting layer as implied by the layer of low relative humidity shown in Fig. 2.19b. The radar estimates for the 5th hour matches good with rain gauges. But starting at the 7th hour, the radar estimates shows underestimation. With the storm height increases, the underestimation of radar estimates is more severe. Compared to the radar estimates at 3 km height, the estimates at 4 km have larger underestimation. The

decrease of particle concentrations with height due to aggregation processes will significantly affect the parameter α. The parameter α in current MRMS system is a fixed constant, which cannot vary with changes in snow particle size distribution and will thus result in an underestimation or overestimation when converting from Z to SWE.

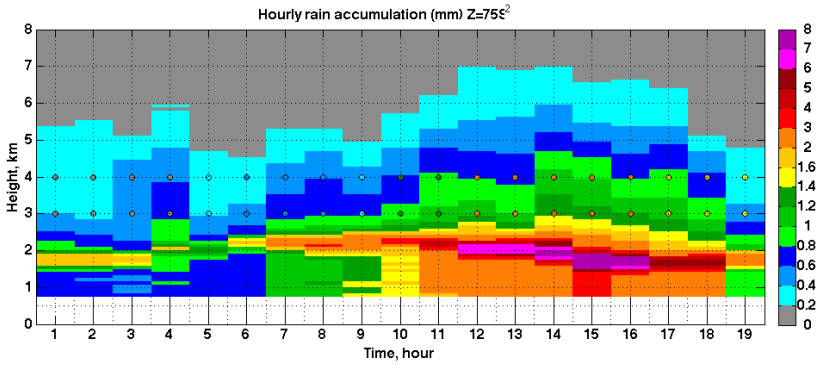

Figure 2.14. The height vs. time representation of vertical profile of hourly radar SWE calculated by using $Z=75R^2$. The colored circles indicate the rain gauges measurements on ground.

Fig. 2.15. Shows a comparison of hourly rainfall from radar data and rain gauge measurements. The circles in the figure indicate the ground radar estimates are calculated from reflectivity at 3 km height, while the filled circles are from 4 km height. Most points seem to be plagued by underestimation. The statistic shows the bias ratio is ~-35% for 3 km but ~-53% for 4 km. The decrease of particle concentrations with height due to aggregation processes will significantly affect the parameter α.

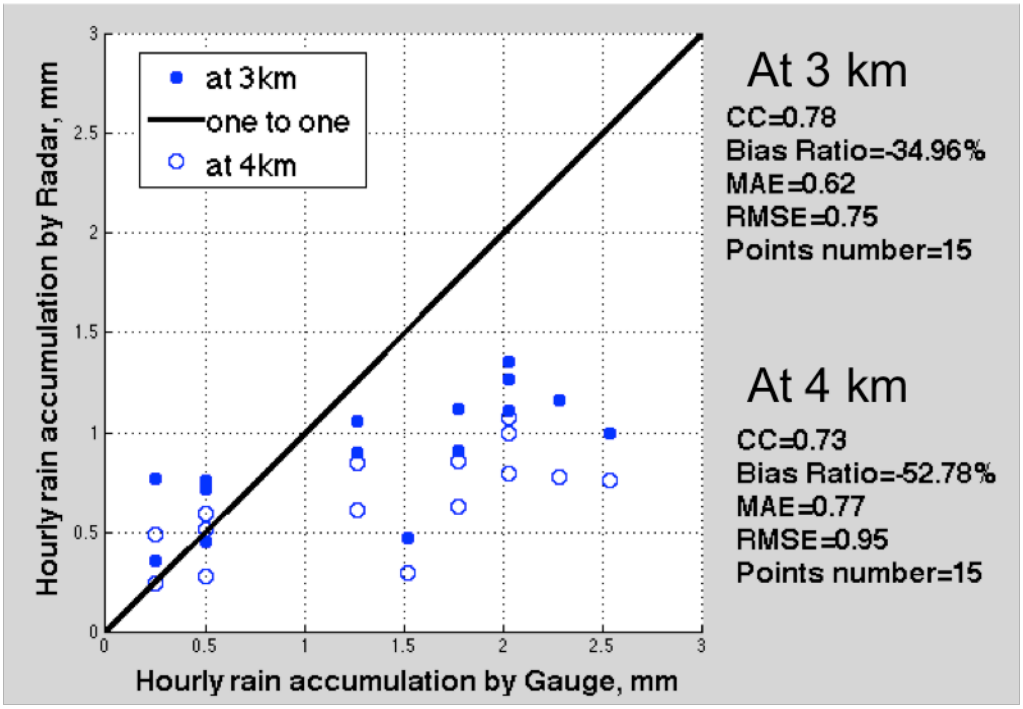

Figure 2.15. Scatterplot of 1-h radar precipitation estimates at 3 km height (circles) and at 4 km height (filled circles).

To minimize the difference between radar precipitation estimates and the gauge measurements, we times a coefficient with α in S= α $Z^{0.5}$. Thus,

$$S = (Coefficient \times \alpha)\, Z^{0.5} \quad \text{.....(2.6)}$$

The coefficients applied to the old Z-SWE relation are show in Fig. 2.16. Fig. 2.16a shows after applying a coefficient of 1.53, the bias ratio is zero. The appropriate Z-SWE relation for radar measurements at 3 km is S = 0.1776 $Z^{0.5}$. Similarly, we applied a coefficient for 4 km measurements and the coefficient valus is 2.12, bigger than the coefficient for 3 km. The new α value is 0.2445 for 4 km radar data.

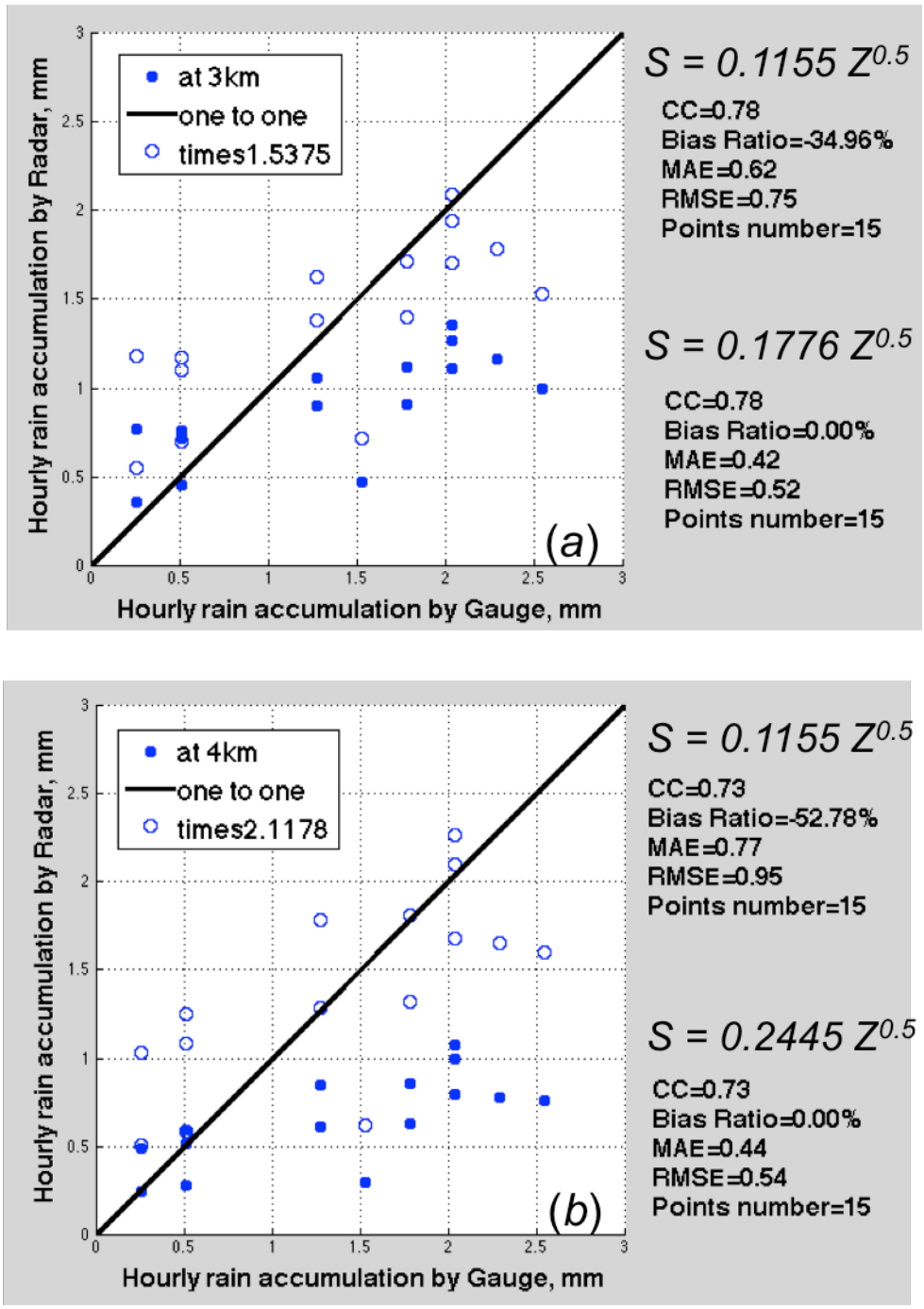

Figure 2.16. Shows radar reflectivity measurements from heights of (a) 3 km and (b) 4 km. The circles indicate the improvements of radar snow estimates by using calibrated α values in Z-S relation.

c. The value of α varies with polarimetric variables and environmental variables.

The parameter α is associated with microphysical processes, which can be constrained by polarimetric radar data and the environmental variables. So our goal is to figure out how the PSD affects parameter α, which can be expressed as a function of polarimetric variables and environmental variables:

$$\alpha = f(\text{Zdr, RhoHV, PhiDP,temperature and relative humidity}) \quad \ldots\ldots (2.7)$$

The environmental variables, e.g. temperature and relative humidity, are from RAP model downloaded from NCDC website (http://nomads.ncdc.noaa.gov/data/rap130). Ryzhkov (2015) suggested β value in $S=\alpha Z^{\beta}$ is 0.64. So I tried $S=0.03Z^{0.64}$ as my first guess to calculate radar SWE rate and then accumulated to 1 hour to compare with rain gauge. The results are shown in Fig. 2.17. Compared to $S = 0.1776\ Z^{0.5}$ shown in Fig. 2.14, $S=0.03Z^{0.64}$ yields more underestimation.

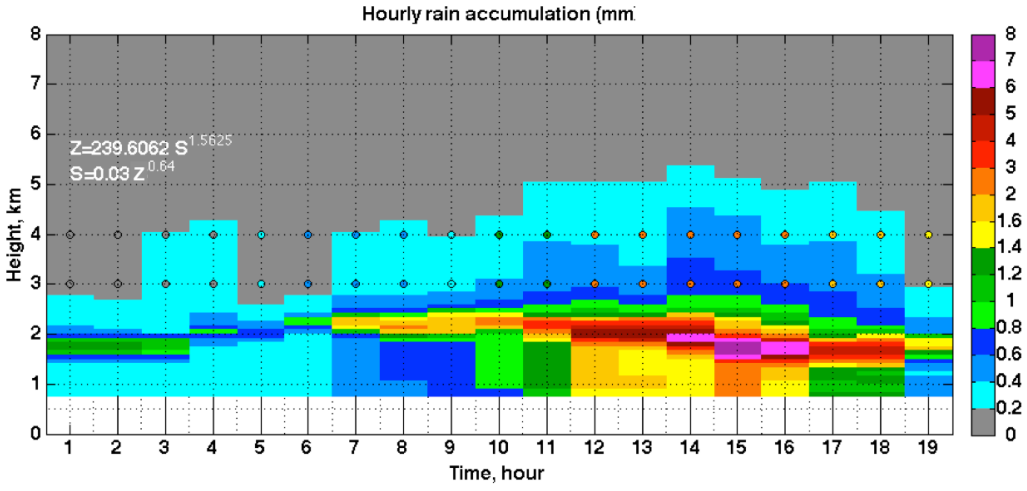

Figure 2.17. The height vs. time representation of vertical profile of hourly radar SWE calculated by using $S=0.03R^{0.64}$. The colored circles indicate the rain gauge measurements on ground.

To eliminate the bias of radar estimates, we apply different α at different height for different time. The height vs. time representation of vertical profile of α value is shown in Fig. 2.18. At the height of 3 km, the value of α changes from 0.02 at the 9th hour to 0.16 at the 13th hour. The change of α reflects different microphysics processes in the storm. The relation between α value and environment variables as well as the polarimetric radar measurements is discussed as follows.

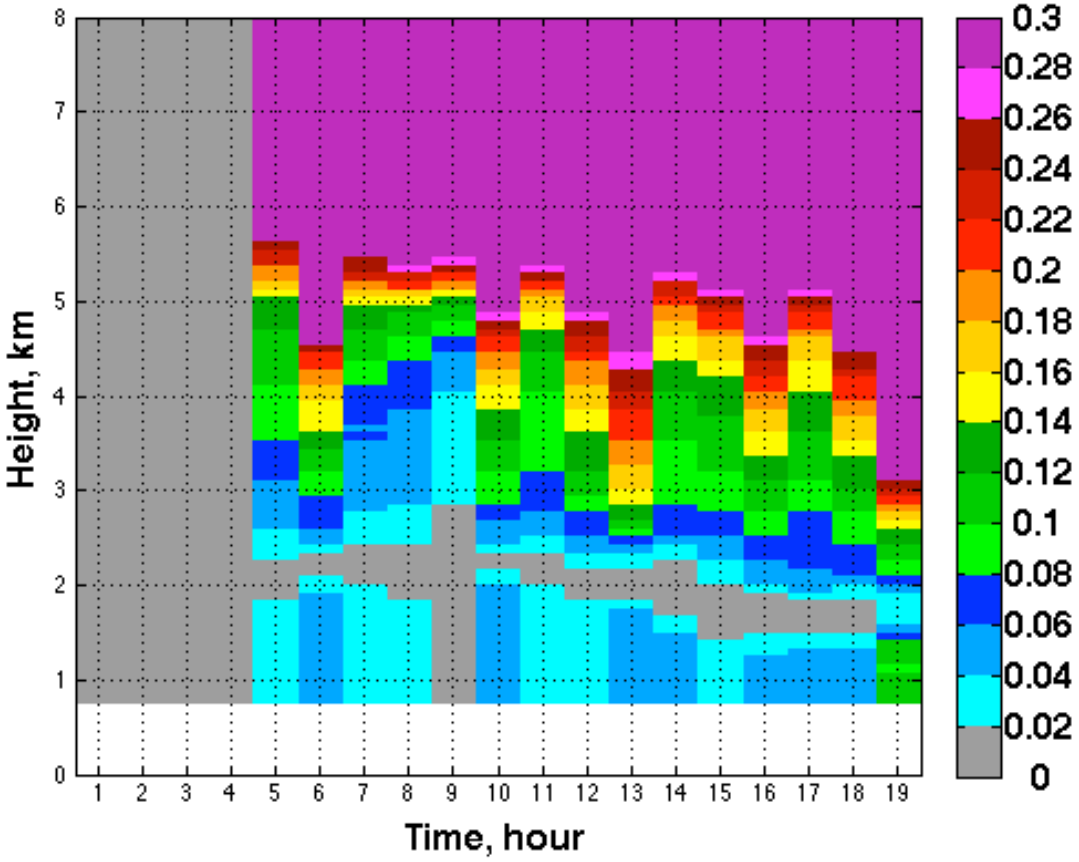

Figure 2.18. The height vs. time representation of vertical profile of α value

The profiles of environmental variables are shown in Fig. 2.19. The temperature has less variation with time compared to the relative humidity. In the first four hours, the relative humidity drops as low as 30% at about 3 km altitude. Evaporation likely

occurs at this height, which causes no precipitation at surface level consistent with rain gauge measurements. In the 10th hour, the relative humidity shows a high value at 8 km height associated with deep storm depth shown in QVP of reflectivity figure in Fig. 2.13.

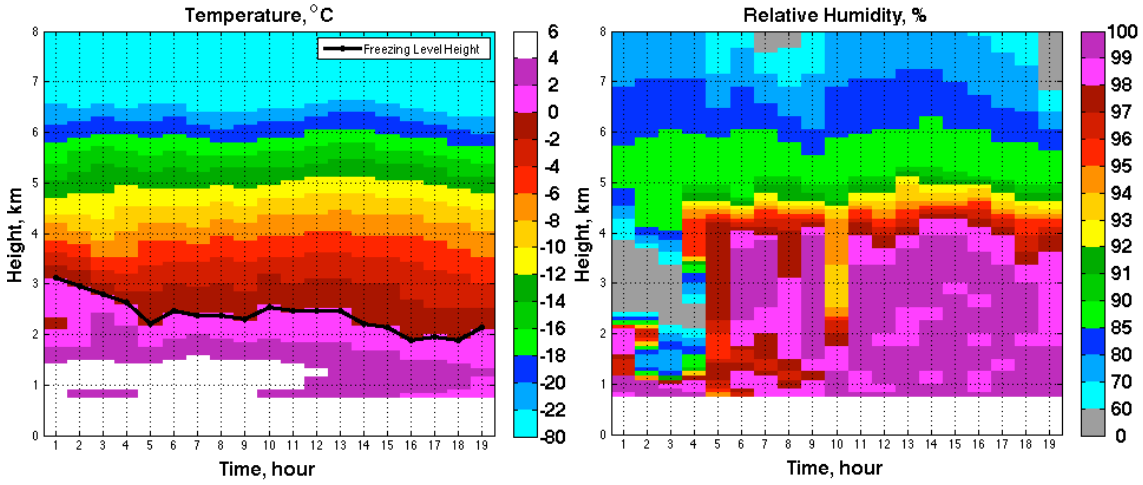

Figure 2.19. The height vs. time representation of vertical profiles of temperature (left) and relative humidity (right) from RAP model.

The change of α with height, temperature and relative humidity is shown in Fig. 2.20. The α value increases as the height AGL increases and decreases as the temperature increases. The parameter α is the most sensitive to temperature. Ryzhkov et al, (2015) discussed α is almost entirely dependent on the intercept of the exponential size distribution of snow N_0, which depend on the snow habit and temperature (Ryan 2000; Heymsfield et al. 2002; Woods et al. 2008). N_0 generally increase with height and decreasing temperatures. The primary reason for decreasing of N_0 with increasing temperature and decreasing altitude is aggregation of ice crystals and snowflakes. Our study is consistent with the results found in Ryzhkov et al, (2015). Higher α value is associated with deeper storm depth at the same height or temperature. The α shows the same value when the relative humidity is almost 100%.

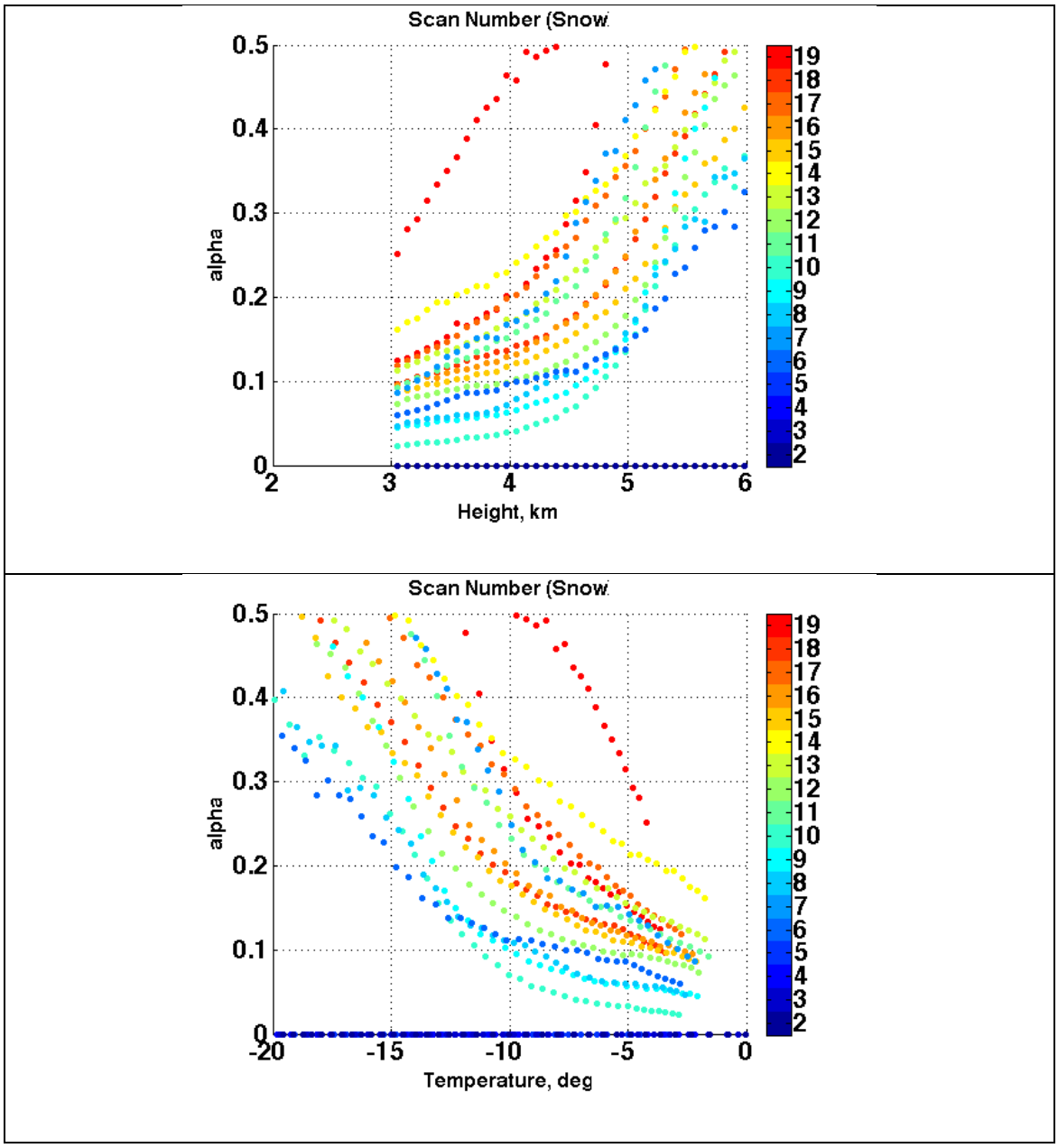
Scan Number (Snow
alpha
Height, km
Scan Number (Snow
alpha
Temperature, deg

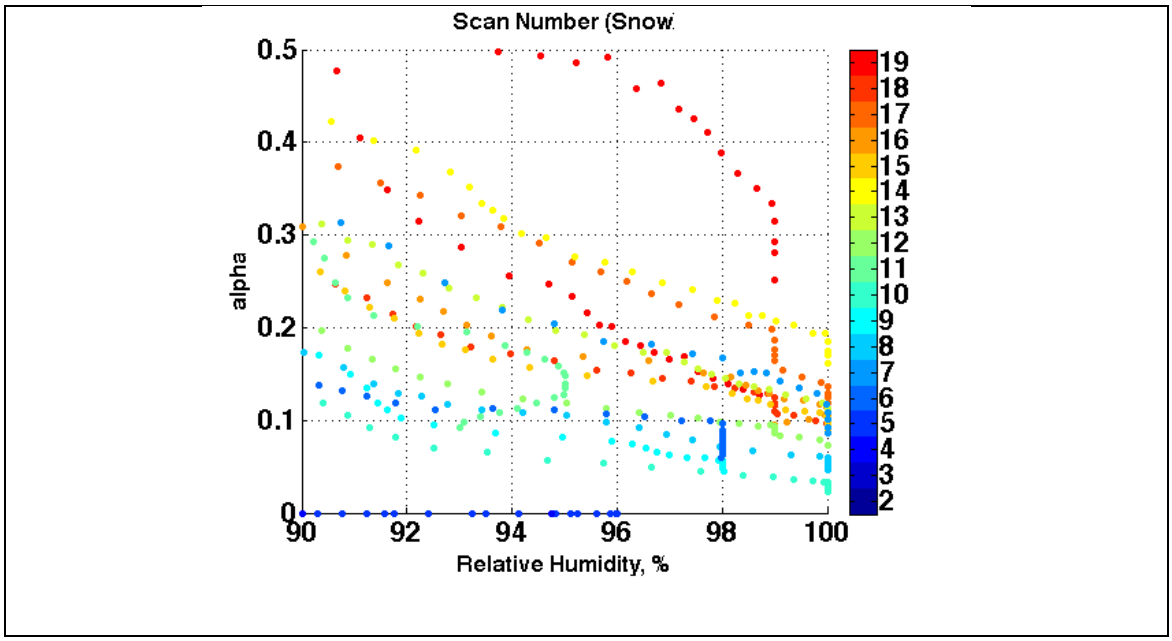

Figure 2.20. The change of α with height, temperature and relative humidity. The color indicates the scan time.

Figure 2.21 shows α changing with radar Z_{DR}. It's interesting to find α shows different relations with Z_{DR} values. The green, yellow and red points shown in Fig. 2.21 from the deep storm shows high α values with low Z_{DR}. The primary reason for these low Z_{DR} and high α is riming of ice crystals and snowflakes. The Fig. 2.22 shows the relation between α and ρ_{hv} as well as Φ_{DP}. But neither of ρ_{hv} and Φ_{DP} show any patterns.

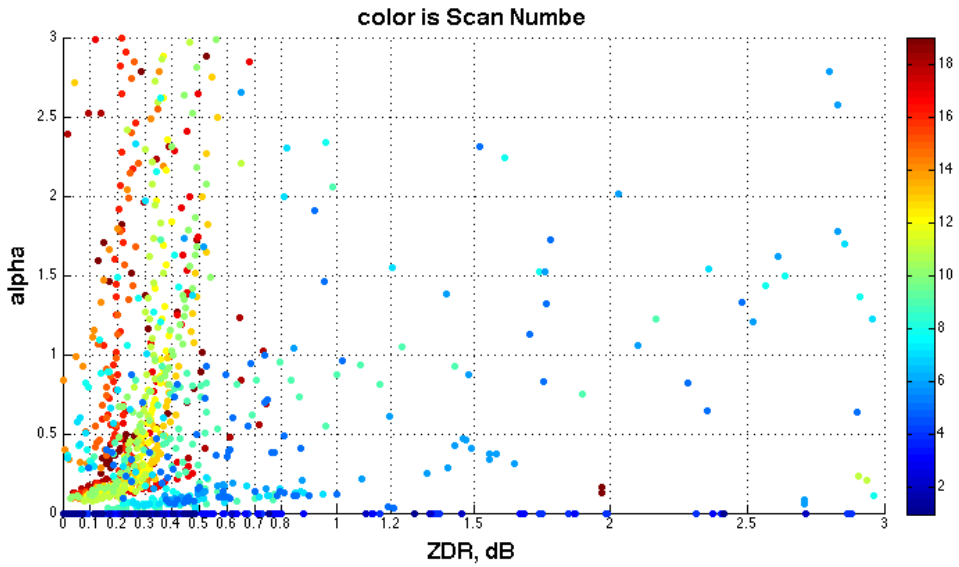

Figure 2.21. The change of α with Z_{DR}. The color indicates the scan time.

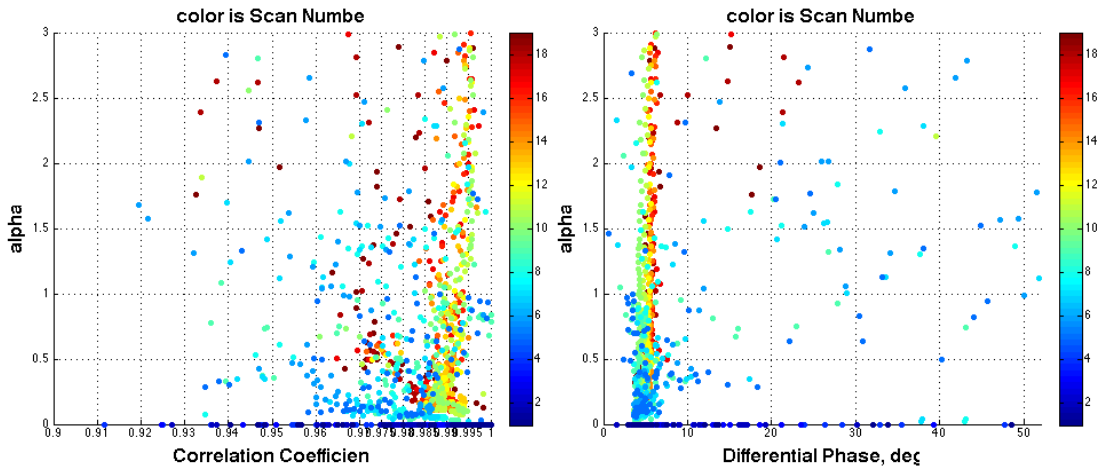

Figure 2.22. Left: The change of α with ρ_{hv}. Right: The change of α with Φ_{DP}. The color indicates the scan time.

References

Amitai, E., X. Llort, and D. Sempere – Torres, 2009: Comparison of TRMM Radar Rainfall Estimates with NOAA Next-Generation QPE. *J. Meteor. Soc. Japan*. **87A**, 109-118.

Anagnostou, E., C. Morales, and T. Dinku, 2001: The use of TRMM precipitation radar observations in determining ground radar calibration biases. *J. Atmos. Oceanic Technol.*, **18**, 616-628.

Bolen, S., and V. Chandrasekar, 2000: Quantitative cross validation of space-based and ground-based radar observations. *J. Appl. Meteor.*, **39,** 2071-2079.

_____, and V. Chandrasekar, 2003: Methodology for aligning and comparing spaceborne radar and ground-based radar observations. *J. Atmos. Oceanic Technol.*, **20**, 647-659.

Chandrasekar, V., A. Hou, E. Smith, V.N. Bringi, S.A. Rutledge, E. Gorgucci, W.A.Petersen, and G. S. Jackson, 2008: Potential role of dual-polarization radar in the validation of satellite precipitation measurements: Rationale and opportunities. *Bull. Amer. Meteor. Soc.*, **89,** 1127-1145.

Doviak, R. J. and D. S. Zrnic, 1993: Doppler Radar and Weather Observations. 2d ed. Dover, 562 pp.

Giangrande, S. E. and A. V. Ryzhkov, 2005: Calibration of dual-polarization radar in the presence of partial Beam blockage. *J. Atmos. Oceanic Technol.*, **22**, 1156-1166.

_____, J. M. Krause, and A. V. Ryzhkov, 2008a: Automatic designation of the melting layer with a polarimetric prototype of the WSR-88D radar. *J. Appl. Meteor. Climatol.*, **47,** 1354-1364.

_____, and A. V. Ryzhkov, 2008b: Estimation of rainfall based on the results of polarimetric echo classification. *J. Appl. Meteor. Climatol.*, **47,** 2445-2462.

Gunn, K. L. S., and J. S. Marshall, 1958: The distribution with size of aggregate snowflakes. *J. Meteor.*, **15**, 452-461.

Iguchi, T., R. Meneghini, J. Awaka, T. Kozu, and K. Okamoto, 2000: Rain profiling algorithm for TRMM precipitation radar. *J. Appl. Meteor.,* **39,** 2038-2052.

Kozu, T., and Coauthors, 2001: Development of precipitation radar onboard the Tropical Rainfall Measuring Mission (TRMM) satellite. *IEEE Trans. Geosci. Remote Sens.*, **39,** 102-116.

Liao, L., and R. Meneghini, 2009: Validation of TRMM precipitation radar through comparison of its multiyear measurements with ground-based radar. *J. Appl. Meteor. Climatol.*, **48,** 804-817.

Morris, K., and M. Schwaller, 2009: An enhanced global precipitation measurement (GPM) validation network prototype. Preprints, *34th Conf. on Radar Meteorology*, Williamsburg, VA, Amer. Meteor. Soc., P7.3.

Park, H., A. V. Ryzhkov, D. S. Zrnic, and K. E. Kim, 2009: The Hydrometeor classification algorithm for the polarimetric WSR-88D: description and application to an MCS. *Wea. Forecasting*, **24,** 730-748.

Petersen, W. A., and M. R. Schwaller, 2008: NASA GPM ground validation: science implementation plan.

Ryzhkov, A. V., S. E. Giangrande, V. M. Melnikov, and T. J. Schuur, 2005: Calibration issues of dual-polarization radar measurements. *J. Atmos. Oceanic Technol.*, **22**, 1138-1155.

Ryzhkov, A. V., P. Zhang, M. Kumjian, S. Troemel, C. Simmer, Quasi-vertical profiles – a new way to look at polarimetric radar data. (To be submitted to *J. Atmos. Oceanic Technol*)

Schumacher, C., and R. A. Houze, 2000: Comparison of radar data from the TRMM satellite and Kwajalein oceanic validation site. *J. Appl. Meteor.*, **39,** 2151-2146.

Simpson, J., C. Kummerow, W.-K. Tao, and R. F. Adler, 1996: On the tropical rainfall measuring mission (TRMM). *Meteor. Atmos. Phys.*, **60,** 19-36.

Vivekanandan, J., W. M. Adams, and V. N. Bringi, 1991: Rigorous approach to polarimetric radar modeling of hydrometeor orientation distributions. *J. Appl. Meteor.*, **30**, 1053-1063.

Wang, J., and D. Wolff, 2009: Comparisons of reflectivities from the TRMM precipitation radar and ground-based radars. *J. Atmos. Oceanic Technol.*, **26,** 857-875.

Waterman, P. C., 1971: Symmetry, unitarity, and geometry in electromagnetic scattering. *Phys.Rre. D*, **3,** 825-839.

Chapter 3 VPR_IE methods

Studies of various physical processes related to water cycle, which are of interest to scientific communities of meteorology, hydrology, environment, ecology, agriculture, etc., often require reliable quantitative precipitation estimation (QPE). Therefore, accurate measurement of precipitation at a range of spatial and temporal resolutions is invaluable for a variety of scientific applications. Weather radar has proven its value to the nation since the installation of the current Weather Surveillance Radar – 1988 Doppler (WSR-88D) network (NEXRAD). Based on data measured by the NEXRAD network, the National Mosaic and the next-generation quantitative precipitation estimation (Q2) system (NMQ; Vasiloff et al. 2007; Zhang et al. 2011) is a real-time test bed comprising high-resolution (1 km, 5 min) multisensor precipitation products. A web-based display and rain gauge-based validation system has been built for the datasets and is freely accessible on the Internet. However, due to the lack of adequate ground radar (GR) coverage from intervening terrain blockages (Maddox et al. 2002), reliable ground-based precipitation measurements are difficult to obtain in mountainous regions.

For ground-based volume-scanning weather radars, an important error source which can lead to significant systematic error in radar rainfall estimates, is attributed to inaccurate calibration of the radar (Smith et al. 1996). Another major error source, particularly in complex terrain, comes from the lack of representativeness of reflectivity sampled aloft to surface precipitation. Reflectivity varies with height due to evaporation at low levels as well as processes of melting, aggregation, and drop break-up. This problem is exacerbated in complex terrain where ground radars must rely on scans at

higher elevation angles to observe precipitating systems, in which radar observations of cloud top are used for QPE. Furthermore, the radar beam broadens with range and could be too wide to accurately resolve the vertical structure of precipitation.

To mitigate radar QPE errors associated with nonuniform vertical profiles of reflectivity (VPRs), a variety of studies have investigated different approaches to derive representative VPRs for improving QPE. The representative VPRs in previous studies include: 1) climatological VPR (Joss and Lee 1995); 2) retrieved VPR from radar observations at different distances and different altitudes (Koistinen 1991; Joss and Lee 1995; Germann and Joss 2002; Andrieu and Creutin 1995; Vignal et al. 1999; Vignal et al. 2000; Vignal and Krajewski 2001, Zhang and Qi 2010); 3) parameterized VPR (Kitchen et al. 1994; Fabry and Zawadzki 1995; Kitchen 1997; Smyth and Illingworth 1998; Matrosov et al. 2007; Tabary 2007). All of these approaches rely on radar data or other surface observations to obtain the VPRs. However, in mountainous regions (e.g., the analysis region of this study), radar measurements near the surface are less ubiquitous and the complete VPRs might not be fully obtained. Some observational limitations of ground-based radar can be mitigated by spaceborne radar whose measurements are much less impacted by mountain blockages and beam broadening effects in the vertical direction (Iguchi et al. 2000). The spaceborne precipitation radar (PR) onboard the NASA Tropical Rainfall Measuring Mission (TRMM) satellite, launched in late 1997, is the first weather radar to estimate rainfall over the tropics and subtropics from space (Simpson et al. 1996). PR operates at Ku band with a frequency of 13.8 GHz and scans across a 215-km wide footprint, with vertical and horizontal resolutions of 250 meters and 4.3 kilometers, respectively, at nadir. Considering that

precipitating systems typically extend several kilometers in the vertical direction, PR's vertical resolution of 250 meters ensures fine observations suitable for studying the vertical structures of storms. Although the precipitation attenuates Ku-band PR observations more than S-band ground radar's, PR's signal processing algorithms developed by the PR science team (Iguchi et al. 2000, 2009) have shown good performance in correcting for attenuation losses in precipitation. Gabella (2006) has used the radar reflectivity calculated for the lowest PR pulse volume, the so-called NearSurfZ from product 2A25, to mitigate GR's range-dependent bias in the island of Cyprus.

3.1 Concept of VPR_IE

3.1.1 Overview

The VPR-IE methodology to correct the ground radar based QPE for VPR sampled from space is summarized in Fig. 1. Note that we follow the formalism from Andrieu and Creutin (1995) and Vignal et al. (1999) and use a normalized VPR (i.e., ratios of reflectivities at different heights vs. the reflectivity at a reference height). In doing so, it becomes implicitly assumed that the reflectivity factor Z(x, h) at location x and altitude h can be expressed as the product of its value at the reference level (h_0, supposed to be 1 km MSL) and the normalized VPR value at the given altitude (see eq. 1 in Kirstetter et al., 2010). The VPR for a given precipitation type (e.g., stratiform) is assumed to be homogeneous over the domain of estimation (i.e. over the study area for a given TRMM overpass). Although the TRMM-PR can accurately resolve the vertical reflectivity variations (owing to its sampling geometry and vertical resolution), it does not match

with WSR-88D radars due to the frequency difference. For instance, the reflectivity of the bright band peak is higher at S band than at Ku band.

In order to use the information from TRMM-PR data for ground-radar correction, we first identify the vertical distribution of hydrometeors and PSD from the TRMM-PR measurements and fit the Ku-band VPR with a physically-based model (Fig. 2). This model is then used to simulate the corresponding S-band VPR (Fig. 2b). Finally, this simulated VPR is convolved with ground radar sampling properties to compute apparent GR VPRs used for surface QPE computation (Fig. 2c). The projection of ground radar measured reflectivity onto the ground level using the S-band VPR applies a three-dimensional radar beam propagation model by assuming the beam refraction of standard atmospheric conditions and accounting for the earth curvature effect as described by Pellarin et al. (2002), Delrieu et al. (2009) and Kirstetter et al. (2010).

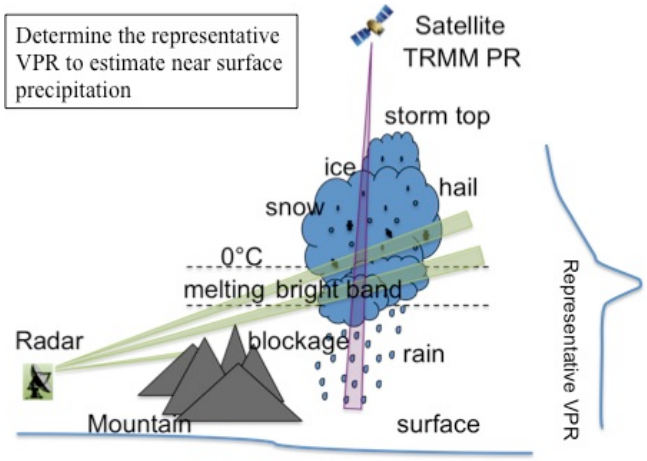

Figure 3.1. Illustration of using spaceborne radar measured representative VPR to improve the near-surface QPE based on ground-radar.

3.1.2 Physically-based VPR model

This section describes a VPR identification method based on a VPR model with several physically-based parameters. The VPR model proposed by Kirstetter et al. (2012) and derived from Boudevillain and Andrieu (2003) aims at representing the vertical evolution of the equivalent radar reflectivity factor:

$$Z_e(h) = \frac{\lambda^4}{\pi^5 |K_w|^2} \int_0^\infty \sigma(D, \lambda, m(h))\, N(D,h)\, dD \qquad (3.1)$$

, where h is the altitude, σ is the backscattering cross-section of a hydrometeor which depends on the equivalent diameter D and the complex refractive index $m(h)$; the refractive index depends on the phase of the hydrometeors and on the radar wavelength λ. $N(D,\mathrm{h})$ is the number of particles with diameters between D and $D + dD$ per unit diameter range and per unit air volume at altitude h; $|K_w|^2$ is a constant depending on the refractive index for liquid water m_w. Equation (1) indicates that the equivalent radar reflectivity factor profile depends on (i) the phase of the hydrometeors, which drives their dielectric properties and scattering cross-sections through a given scattering model (T-matrix, Mie, Rayleigh), (ii) the PSD and (iii) the radar wavelength.

The atmospheric column is divided into three vertical layers. The upper layer contains particles of frozen water with air inclusions. In the lowest layer, the precipitation particles are raindrops. The intermediate layer is the melting layer in which particles are composed of a mixture of ice, air and liquid water. These three layers are defined by their altitude boundaries. The top of the precipitating cloud, provided by the radar echo top, is denoted as h_T. The interface between solid and

melting layers (the freezing level for stratiform precipitation) is denoted as h_M. Δh_E is the melting layer's vertical extension. A reference level close to the ground denoted as h_0 is considered the bottom of the liquid layer. The temperature is assumed to decrease with altitude at the moist adiabatic lapse rate. The scaling formalism initially proposed by Sempere Torres *et al.* (1994) is used to describe the relationship between the PSD (assumed as gamma) and the equivalent radar reflectivity factor in the liquid phase, and to infer the PSD in the other layers.

The liquid layer is defined between the reference level h_0 and the melting layer (level $h_M - \Delta h_E$), where hydrometeors are liquid drops. Vertical variations of the equivalent radar reflectivity factor are assumed linear from Z_0 at h_0 to Z_m at $h_M - \Delta h_E$, with a slope G_l. In the solid layer, the hydrometeors are heterogeneous and described by a matrix of ice with inclusions of air. The "matrix inclusion" scheme (Klaassen, 1988) is used to retrieve the refractive index of hydrometeors and calculate their dielectric properties. The composition of a solid particle is parameterized using a density factor D_g, varying between 0 (light snow) to 1 (hail) to cover the entire range of mass density of hydrometeors:

$$\rho(h) = \rho_{min}^{1-Dg} \rho_{max}^{Dg} \quad \text{with } \rho_{min} = 5 \text{ and } \rho_{max} = 900 \text{kg.m}^{-3} \tag{3.2}$$

The density factor drives the composition of the particles through the ice volume fraction of the total particle volume (Boudevillain & Andrieu, 2003, Kirstetter et al., 2012):

$$f_{mat} = (\rho_{min} / \rho_{max})^{1-Dg} \text{ and } f_{inc} = 1 - f_{mat} \tag{3.3}$$

where f_{mat} and f_{inc} are the matrix fraction and the inclusion fraction, respectively. The density factor D_g is part of the calculation of the complex refractive index m through the composition of particles and drives therein the dielectric properties of the particles. It is supposed to remain constant in the solid phase and the melting layer. The form of the VPR in the solid layer therefore depends on the PSD defined at the top of the liquid layer and on D_g. The melting layer is a transitional zone in which the backscattering properties of precipitation particles change rapidly. The possible enhancement of the measured reflectivity by the radar, the bright band, occurs in this zone. The present study uses the simple and convenient scheme proposed by Hardaker *et al.* (1995), which reproduced the high gradients of reflectivity with a reduced number of variables representative of the PSD, composition and dielectric properties in this zone. Assuming the PSD to be constant between solid particles and liquid raindrops ensures the continuity of the PSD at the solid/melting and melting/liquid transitions. Particles are composed of a mixture of liquid and solid water with inclusions of air. They are characterized by the melted mass fraction f_m increasing from 0 at the level h_M to 1 at the level $h_M - \Delta h_E$. A two-step processing of the Klaassen (1988) concept and the "matrix inclusion" scheme are applied. By driving the density and the dielectric properties of the particles, D_g controls the enhancement of the bright band. Values of D_g of about 0.8 simulate very light snowflakes with large air inclusions. These particles are more characteristic of stratiform precipitation, and the model simulates an enhanced bright band. Values of D_g of about 1.0 simulate denser particles more often met in convective precipitation. This simple melting layer model could be

refined following the results of the series of papers devoted to the bright band description (Szyrmer and Zawadzki, 1999).

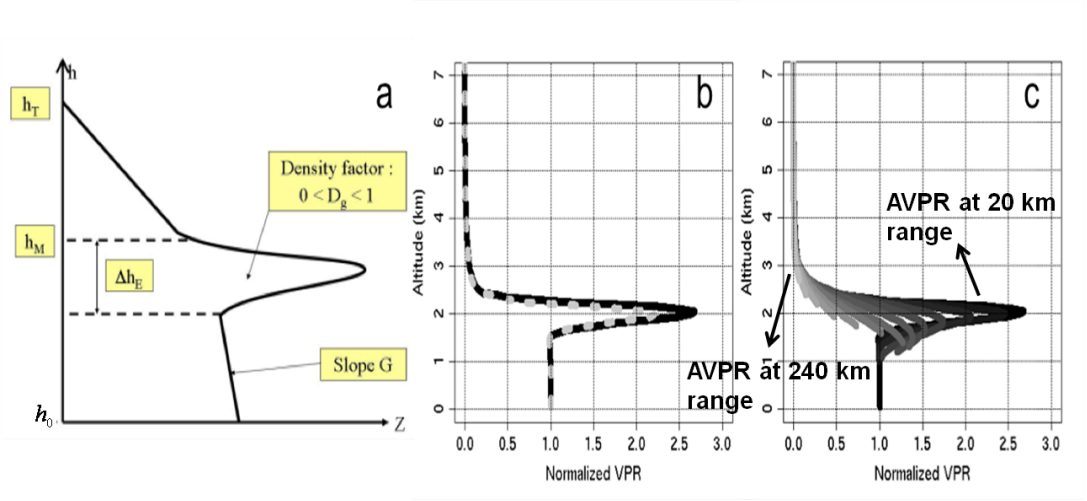

Figure 3.2. Steps for incorporating TRMM-PR measurements into NMQ-QPE (VPR-IE method). The representative example of the VPR on December 8, 2009 is shown: (a) fit a physically based VPR model (5 parameters) on the Ku-band TRMM-PR reflectivity profiles; (b) convert the Ku-band VPR (dotted grey line) into S-band VPR (solid black line); (c) convolve the S-band VPR with the sampling properties of WSR-88D ground radars. On panel (c), apparent VPRs are simulated from the S-band VPR from (b) at various distances (from 20 to 240 km with an interval of 20 km) using the beam characteristics of WSR-88D radars.

To summarize, the vertical variations of the equivalent reflectivity factor according to altitude can be represented using a model for the vertical variations of hydrometeors and PSD. These vertical variations of the equivalent reflectivity factor can finally be written $Z_e(h;\varphi)$, while $\varphi = \left[G_l, h_T, h_M, \Delta h_E, D_g\right]$ is the vector grouping the five parameters of the VPR model. Note that this set of parameters is relative to the microphysics only and do not depend on the radar wavelength. The VPR, defined as the equivalent reflectivity factor Z_e with altitude, normalized by its value at the reference level Z_0 is expressed: $z(h;\varphi) = Z_e(h;\varphi)/Z_0$.

3.2 Implementation of VPR_IE

For a given event, an optimization procedure adjusts the VPR model to each individual reflectivity profile from the 2A25 product. It uses a quadratic cost function that is minimized with respect to the parameterized profiles of reflectivity using a Gauss–Newton method (Kirstetter et al., 2010). During the optimization procedure, Ku-band VPRs are simulated using the model to match with the TRMM-PR measurements. Figure 3.3 shows the histograms of parameters resulting from the fitting on TRMM-PR reflectivity profiles for the case of 8 December 2009. The histograms of the parameters are typically unimodal, so that a representative VPR may be extracted for the whole stratiform region. The top of the precipitation presents more uncertainties than the other parameters; it may be due to real variations of the vertical extension of the rain field in the region linked to significant elevation differences as well as different PR beam filling conditions and relatively poor sensitivity of the radar (17 dBZ). The most probable values for the density parameter D_g are around 0.85, which is consistent with stratiform precipitation. The retrieved freezing level height is for most of cases within the range [2400-2600] m altitude, in accordance with the mean value extracted from the 2A25 product. The histogram of the melting layer thickness is highly peaked around 850 m, which is realistic from long-term bright-band observation studies (Fabry et al., 1995). Finally, the histogram of the slope of the profile in liquid phase is peaked around 0. More research is needed to investigate the variability of these parameters and the corresponding vertical variations of hydrometeor and PSD.

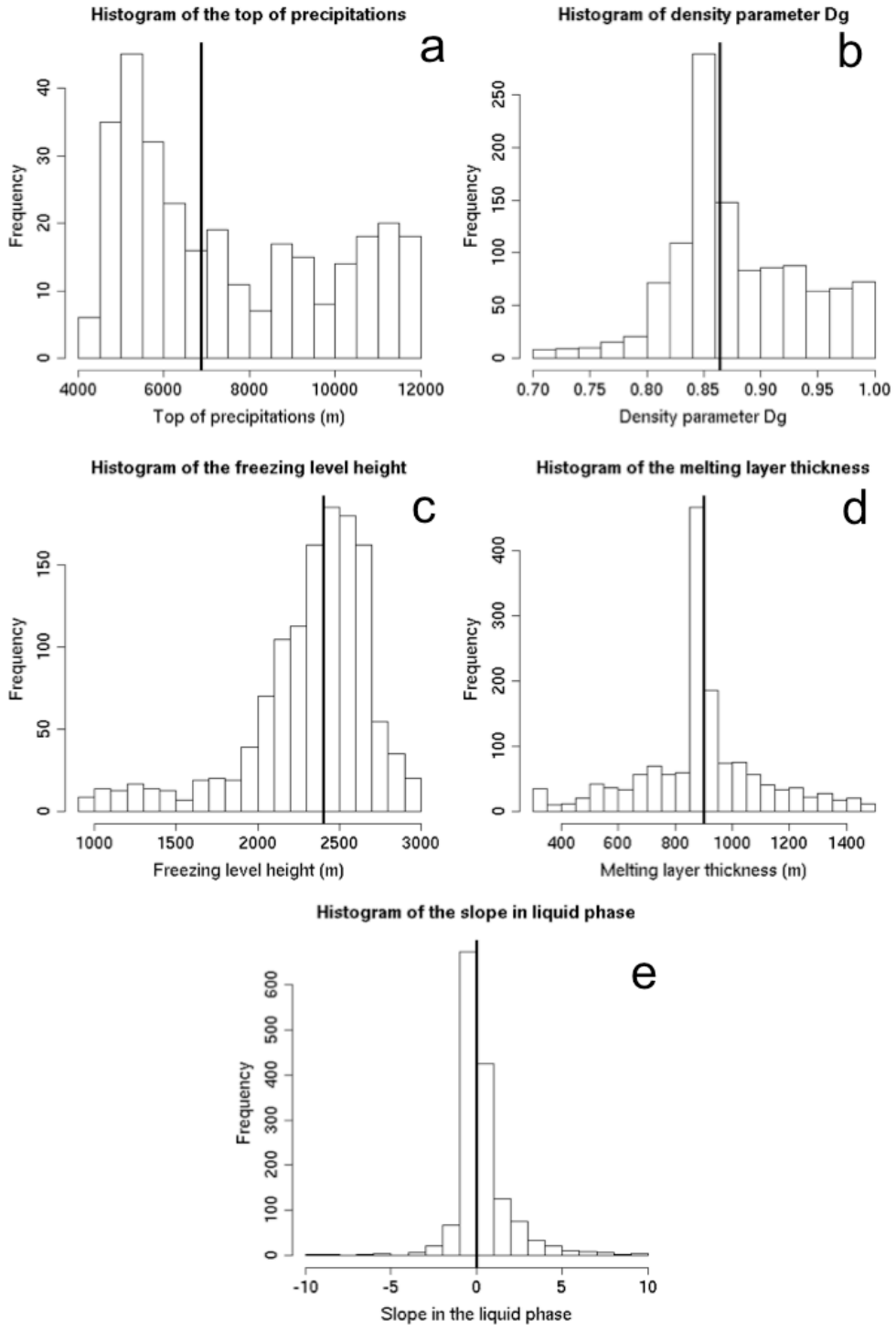

Figure 3.3. Histograms of the five parameters of the physically based VPR model fit on TRMM-PR reflectivity profiles passing over Arizona at 01:35Z on 8 December 2009: (a) the top of precipitation h_T, (b) the density parameter D_g, (c)

the freezing level height h_M, (d) the melting layer thickness Δh_E, and (e) the slope of the profile in liquid phase G_l.

Our goal is to identify a representative VPR for the whole stratiform region sampled conjointly by ground radar and the PR. The characteristics of this VPR differ from those of the ‘‘true’’ VPR sampled quasi-instantaneously at the PR pixel level because it is representative of a much larger domain. Kirstetter et al. (2010) addressed specifically the issue of VPR homogeneity by performing the VPR identification over areas of homogeneous rain types and consistent microphysical processes. Figure 3.3 shows that while increasing the representativeness of the VPRs by focusing on the stratiform region (rain type information is from TRMM 2A23 product), the parameters retrieved from the individual 2A25 profiles present variability, which may be caused by microphysics variability inside the stratiform region, noise in the sampled radar reflectivity profiles and/or simplifications of the physically-based VPR model. A representative VPR for the whole stratiform region may be characterized by a unique set of parameters $\varphi = \left[G_l, h_T, h_M, \Delta h_E, D_g \right]$. We consider the median of each parameter distribution to identify φ. The corresponding VPRs at Ku-band and S-band for the representative case of 8 December 2009 are shown in Fig. 3.2b.

We summarize the VPR-IE procedure below:

- A physically-based VPR model serves to retrieve the vertical hydrometeor and PSD profiles from the TRMM-PR measurements by focusing on the stratiform region;

- This model is used to simulate the corresponding S-band VPR, because the model parameters do not depend on the radar wavelength;

- This representative VPR is convolved with ground radar sampling properties to compute the apparent VPRs;

- The correction is applied to the reflectivity at the corresponding ranges where the apparent VPRs are computed;

- The reflectivity field is converted into rainfall rate using Z-R relations: $Z= 200R^{1.6}$ for stratiform rain and $Z=300R^{1.4}$ for convective rain. The rainfall rates are then accumulated to hourly rainfall amounts and compared to rain gauge observations.

We assess the approach in the next section by comparing rainfall estimates from the VPR-IE method with respect to the conventional NMQ products and two additional correction methods.

3.3 Case study of VPR_IE

In the current study, we have chosen the region of Arizona and southern California (latitude is from 32°N to 37°N, longitude is from -115°to -110°) as the study area (Fig. 3.4). QPE in this region is challenging due to the sparseness of rain gauge networks, high spatial variability of precipitation due to orographic enhancements, relatively shallow precipitating clouds, and insufficient NEXRAD radar coverage. The digital elevation map in Fig. 3.4 shows the topography in this study area, which consists

of six smaller regions: the plateau region (the White Mountains, Mogollon Rim, and Kaibab Plateau of northern Arizona), the central region (the transition zone between the plateaus of the north and the desert of the south), the northwest region (also a transition zone between the plateau region and the lower desert), the southwest region (Phoenix and all of the lower desert), the southeast region, and northeast region (Colorado plateau system) (Sellers and Hill, 1974; Watson et al. 1993). The average altitude of the study area is about 1106 m, while the lowest elevation is only 3 m and the highest elevation is 3657 m. The climatological statistics in this area indicates two peaks of precipitation each year – one in the winter caused by large-scale synoptic systems and the other one in the summer caused by the North American monsoon.

Nearly half of the area has average rainfall of less than 250 mm per year. The southwest region receives rainfall amounts of less than 125 mm per year. The northern plateau regions have an average rainfall of more than 500 mm per year (Sellers and Hill 1974). Experience with more than 3 yr of radar data in the NMQ system indicates that the ground radar QPE has significant underestimation issues due to the poor sampling of precipitation. Figure 3.4 shows that some regions are as far as 100 km or even 200 km from the nearest radar (e.g. 35°N and 113°W at more than 200 km from the nearest radar). For the six WSR-88D radars included in this study, the surrounding highlands cause partial or even complete beam blockage to radars (especially at lower elevation angles). At significant distances from the radar (e.g. more than 100 km) this hampers the sampling of precipitation close to the ground with the lower elevation angles. The radar beam might be too high and sample the ice region above the melting layer while it is raining at the surface, causing large errors in surface rainfall estimation because of

the vertical variations of reflectivity. In such conditions the radar beam may be too wide to accurately resolve the vertical structure of precipitation. This is particularly true in the case of strong vertical reflectivity gradients, e.g., linked to the bright band (Kirstetter et al. 2010). Figure 3.2c illustrates the effect of beam widening on the apparent GR VPRs, which degrades with range. It is clearly shown that the bright band becomes thicker and less intense with increasing range. The apparent VPR is defined as the VPR influenced by beam broadening. It is noted that due to earth curvature and the increase of beam altitude, the radar beam samples less often the lowest part of the VPR with increasing distance. This effect is aggravated by beam blockage due to surrounding highlands.

The NMQ system (Zhang et al. 2011) combines information from ground-based radars comprising the National Weather Service's NEXRAD network. Based on the significant research already performed on the ground-based NMQ data in regards to data quality (Lakshmanan et al. 2007), data mosaicking techniques (Zhang et al. 2005), rainfall estimation (Vasiloff et al. 2007), the system has been generating high-resolution national 3-D reflectivity mosaic grids (31 levels) and a suite of severe weather and QPE products at a 1-km horizontal resolution and 5-minute update cycle since June 2006. We have identified five TRMM PR overpasses that meet the following criteria: 1) the maximum time discrepancy between TRMM PR and NMQ data is less than 1 hour, 2) the overlapping area of TRMM PR and NMQ data is larger than 5000 km^2, 3) the maximum rainfall rate measured by ground radar is greater than 10 mm/hr. These five overpasses, hereinafter referred to as events, have been chosen from five different winter days in 2009 and 2010, since Arizona's climate exhibits precipitation peak

during the winter and the bright band is typically low during the cold season. The event descriptions and times are listed in Table 3.

Table 3. Summary of the events.

Event no.	Events/case study (Orbit no.)	Description	No. of radar-gauge pairs
1	8 Feb 2009 (64005)	Moderate stratiform precipitation	18
2	8 Dec 2009 (68721)	Heavy precipitation with wide spread stratiform; snow in north AZ	147
3	22 Jan 2010 (69423)	Heavy precipitation with wide spread stratiform	262
4	28 Feb 2010 (70003)	Moderate stratiform precipitation; weak convection likely	238
5	7 Mar 2010 (70110)	Moderate stratiform precipitation with scattered cells;	60

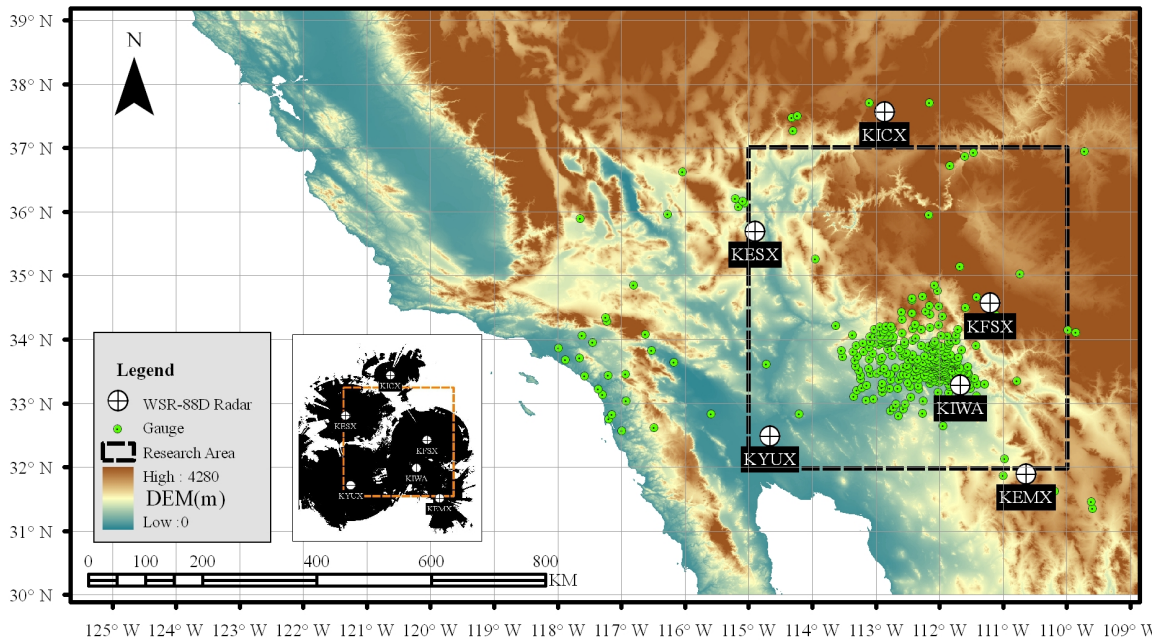

Figure 3.4. An image showing the topography around the study area (black dashed box) and the locations of rain gauges (circles) and WSR-88D radar sites (white circles with cross). The inset black and white map shows the radar coverage at 3 km above ground level.

Hourly rain gauges from the Hydrometeorological Automated Data System (HADS; http://www.nws.noaa.gov.oh.hads/) and the Maricopa County mesonet have been used to evaluate the three different QPE methods by blending the PR with GR observations for five events (summarized in Table 1). It is worth noting that ground radars used for this study have different elevations. As shown in Fig. 3.4, the elevations of KICX, KFSX, KEMX KESX, KIWA, and KYUX radars are 3231, 2261, 1586, 1509, 421, and 53 meters above mean sea level, respectively. Given a storm system in the cold season, the radar beam could overshoot cloud tops or intercept the melting layer at far ranges, especially for KICX, KFSX, KEMX, and KESX radars. According to the locations of rain gauges shown in Fig. 3.4, the QPE based on KFSX radar is most likely affected by the melting layer. Figure 3.5 shows a comparison of hourly rainfall from remote-sensing data and rain gauge measurements, with the three panels corresponding

to the three different methods of blending PR with GR observations. Data shown in this analysis is from all five events combined. The black dots in the figure indicate the GR QPE without any adjustment from PR. Most points seem to be plagued by either underestimation or overestimation. Considering the height of freezing level in the cold season and the position of radar beam in this complex terrain, overestimation is likely due to sampling in the bright band, while the underestimation is likely attributed to sampling frozen hydrometeors above the freezing level. The simple rainfall rate calibration method (Fig. 3.5a) shows some improvements of the QPE, although not significant. The correction using the rings-based range adjustment method (Fig. 3.5b) generally reduced the underestimation but resulted in erroneous overestimation. This was due to the monotonic linear model used in the correction scheme where overestimation errors associated with the bright band and underestimation errors associated with radar sampling in the ice region could not be simultaneously accounted for. The underestimation errors might have dominated the linear regression model and as a result the overestimation error did not get corrected but rather exaggerated. Figure 3.5c shows the QPE result obtained with the VPR-IE method introduced in the last section. This method mitigates both overestimation and underestimation of rainfall, showing a much better agreement with gauge observations than the other two methods.

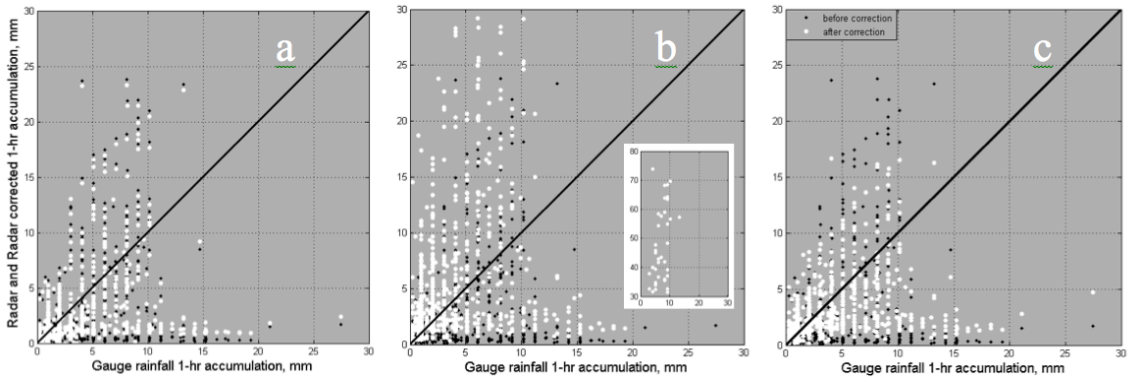

Figure 3.5. Scatterplots of 1-hour radar precipitation estimates before (black) and after (white) the corrections for all five events combined using the (a) rainfall rate calibration method (b) rings-based range adjustment and (c) VPR-IE method.

Figure 3.6 provides hourly rainfall maps with and without applying the VPR-IE method (results using the other two methods are not shown) for each case study. For example, Fig. 3.6c shows a widespread stratiform precipitation on 8 December 2009, for which the freezing level was about 1800, 1800, 2100, 2500, 2600, 2800 meters above mean sea level (MSL) for the KICX, KESX, KFSX, KIWA, KYUX, and KEMX radars, respectively. Note that these freezing level heights are consistent with the histogram of the freezing levels from the VPR model approach (see Fig. 3.2c). For most rainy areas shown in this figure, the radar beam has overshot the melting layer. The measurements within the ice region led to underestimation of rainfall on the surface from the original NMQ QPE product at lower elevations (Fig. $3.6b_1$). After the VPR-IE method was applied (Fig. $3.6b_2$), the underestimation was mitigated, especially in areas 100 km east of KESX and 50 km southeast of KFSX. Another example is 28 February 2010, for which the freezing level was 2400-2600 meters within the area from 33.5°N to 34°N in latitude and from -113° to -112° in longitude. KFSX's radar beam intercepted the melting layer in this area, causing an overestimation of rainfall in the original NMQ QPE as shown in Fig. $3.6a_4$. The VPR-IE product (Fig. $3.6b_4$) reduced this apparent overestimation. On the other hand, similar to the analysis in Figs. $3.6a_2$ and $3.6b_2$, at the further range (e.g., >100 km) where radar beam has overshot the melting layer and samples in the ice region, the VPR-IE method has increased the estimate of rainfall, which was previously underestimated.

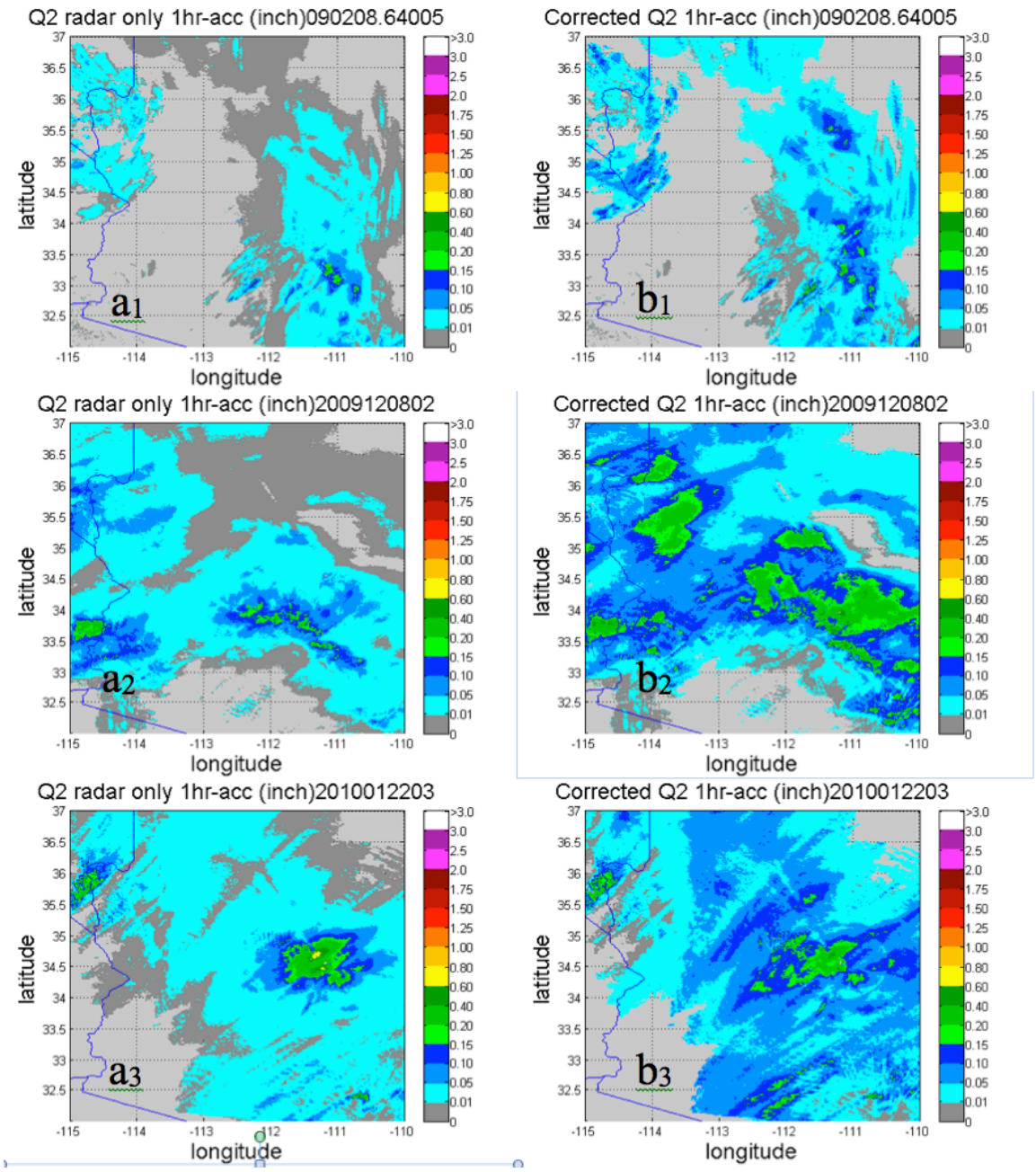
Q2 radar only 1hr-acc (inch)090208.64005
Corrected Q2 1hr-acc (inch)090208.64005
Q2 radar only 1hr-acc (inch)2009120802
Corrected Q2 1hr-acc (inch)2009120802
Q2 radar only 1hr-acc (inch)2010012203
Corrected Q2 1hr-acc (inch)2010012203
latitude
longitude
a1
b1
a2
b2
a3
b3

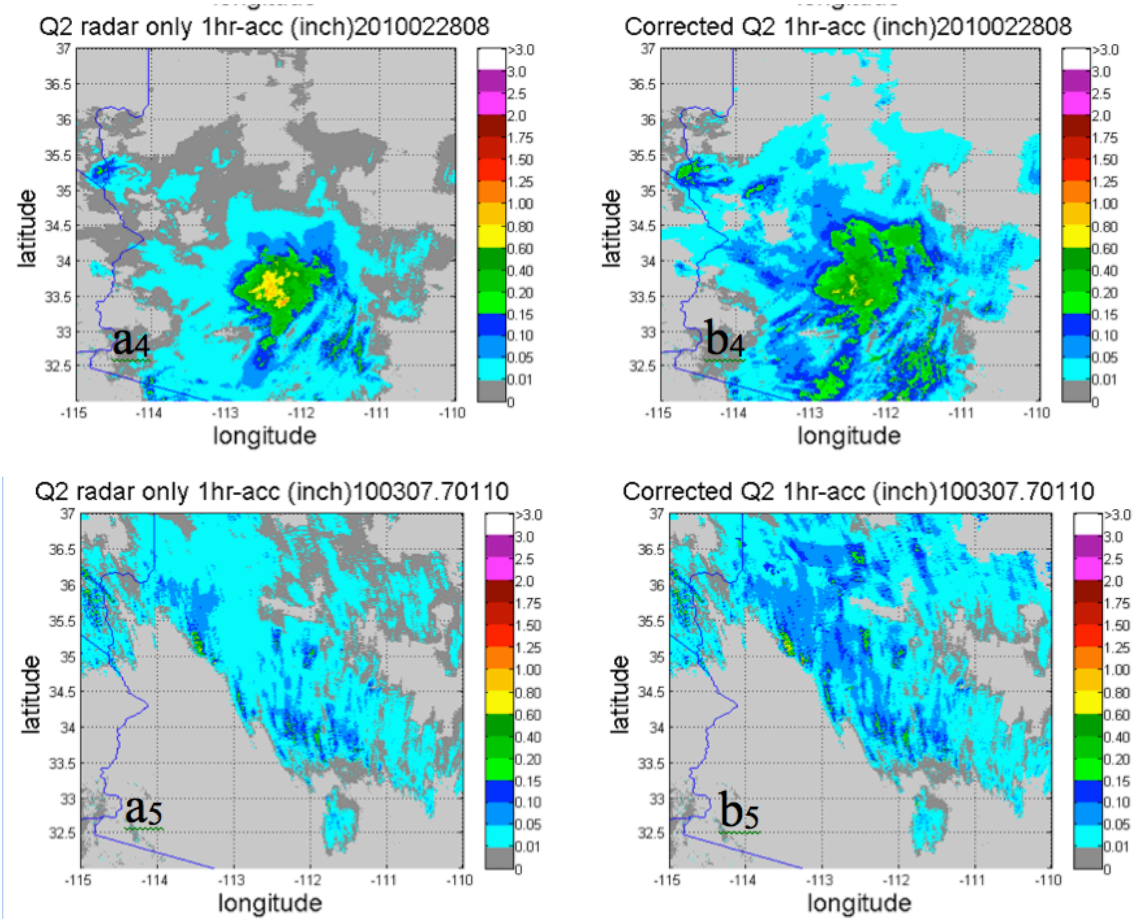

Figure 3.6. 1-hour radar estimates before (Column a) and after (Column b) adjustment using the VPR-IE method.

From the five events shown in Fig. 3.6, three statistical indices have been calculated to evaluate the performance of the three correction methods. Relative bias (Bias in %) is used to assess the systematic bias of radar estimation. The mean absolute error (MAE) measures the average magnitude of the error. The root mean squared error (RMSE) is another way to quantify the average error magnitude, giving greater weights to larger errors. MAE and RMSE are in units of mm for the comparison of estimated rainfall amounts.

$$RB = \frac{\sum_{i=1}^{N} R(i) - \sum_{i=1}^{N} G(i)}{\sum_{i=1}^{N} G(i)} * 100\% \quad . \qquad (3.4)$$

$$MAE = \frac{\sum_{i=1}^{N} |R(i) - G(i)|}{N} \quad .. \qquad (3.5)$$

$$RMSE = \sqrt{\frac{\sum_{i=1}^{N} |R(i) - G(i)|^2}{N}} \qquad (3.6)$$

Here, R(i) and G(i) represent the ith matching pair of rainfall amounts estimated with radar reflectivity and observed by rain gauges, respectively. *N* represents the total number of data pairs for radar-based and rain gauge data matching. The following two criteria have been used for matching data: (i) the gauge location is within one of the $0.01^0 \times 0.01^0$ radar grid cells used in NMQ/Q2, and (ii) both R(i) and G(i) are greater than zero.

Table 4. Statistical results of the three TRMM PR-based correction approaches. I is the rainfall rate calibration method; II is the rings-based range adjustment method; III is VPR-IE method. The method with the best performance according to the statistic is denoted in boldface.

E	*Bias (%)*				*MAE*				*RMSE*			
	Q2	I	II	III	Q2	I	II	III	Q2	I	II	III
1	-69.08	-80.40	**-26.27**	-50.40	0.63	0.75	0.75	**0.48**	1.18	1.30	1.19	**0.94**
2	-39.52	-28.19	71.05	**-12.58**	1.36	1.31	2.51	**1.00**	2.39	2.30	4.10	**1.55**
3	-85.90	-75.19	**-58.04**	-68.60	4.27	3.80	**3.43**	3.50	6.25	5.82	**5.36**	5.45
4	29.55	18.15	242.99	**13.87**	2.44	2.46	10.23	**1.75**	3.98	3.85	17.17	**2.54**
5	-16.93	-36.05	154.85	**-5.09**	**0.97**	0.98	3.09	0.98	1.89	1.91	4.44	**1.81**
All	-38.23	-36.02	69.17	**-21.09**	2.64	2.53	5.30	**2.15**	4.50	4.29	10.47	**3.93**

The statistics have been computed with hourly rainfall estimates and are shown in Table 4 for all five events. The "Q2" columns denote the results calculated from

original GR-only product of NMQ/Q2. The best statistical performances among the three methods are highlighted in bold. Generally speaking, the third method (i.e., VPR-IE method) has the best overall performance compared to the other three approaches. The rings-based range adjustment (i.e., the 2nd method) has the least improvements. This result is likely due to the monotonic linear empirical relation for range adjustment (Eq. 3.3), which is insufficient to simultaneously correct for both overestimation in the melting layer and underestimation with increasing range when sampling in the ice region. However, it is interesting to see this method performs the best for Event #3 on 22 Jan 2010, which was a widespread stratiform event with a freezing level from 2000 to 3000 meters, gradually increasing in altitude from northwest to southeast within the analysis region. The KIWA radar was not working during this case and GR observations mainly came from KICX, KESX, KFSX, and KEMX radars. As a result, all GR observations were above the melting layer and were affected by beam overshooting, alone, rather than underestimation combined with overestimation by sampling in the bright band (Fig. 3.6a$_3$). Significant underestimations of surface rainfall are indicated in Table 4 (underestimate by 58.04-85.9%) for all QPE approaches. The MAE and RMSE values are high as well. The VPR-IE does not show improvements over the rings-based range adjustment in this particular case where the variation of the freezing level from 2000 to 3000 m. This result implies that one representative VPR might not be sufficient to account for the variability of the vertical structure of precipitation in this region, warranting additional research.

Events #2 and #4 on 8 December 2009 and 28 February 2010 demonstrate superior performance of the VPR-IE correction method. GR beam overshooting was a major

issue in the former event while the interception of the melting layer was more evident in the latter event. Table 4 shows effective mitigation of both underestimation and overestimation, with the Bias changing from -39.5% to -12.58% and from 29.55% to 13.87%, respectively. The estimation errors (MAE, RMSE) are also reduced greatly. The simple rainfall rate calibration method I improved the bias over the uncorrected, radar-only method in both these cases, while the rings-based method II increased the bias up to 243% in Event #4.

Systematic error of ground-based radar rainfall estimation, related to the VPR features combined with the geometric effects of the radar beam, creates the often-noted radar range dependence (Bellon et al., 2005; Krajewski et al. 2010). Figure 3.7 shows the range-dependent multiplicative bias ((radar – rain gauge) / rain gauge ratios) as a function of distance from the radar for Events #2 and #3. Considering the relative position of the rain gauge network to the radar sites, the observations evaluated in this figure mainly come from the KIWA radar for distances within 100 km of it and the KFSX radar. We recall the 8 December 2009 Event #2 corresponds to a freezing level height of 2500 meters at MSL while the KIWA radar altitude is 421 meters at MSL. For the uncorrected QPE, the contamination of the radar beam by the bright band leads to bias values exceeding 0 around a range of 70 km, and the overshooting of the radar beam in the ice phase at distances greater than 100 km causes the far range underestimation (Andrieu and Creutin 1995). The VPR-IE using the TRMM-PR information mitigates significantly the range-dependent error. We recall that for the 22 January 2010 Event #3 the KIWA radar data were not available so the range-dependent error is mainly for observations from the KFSX radar. Its altitude is 2261 meters above

MSL while the freezing level height was around 2600 meters above MSL, causing contamination of the radar beam by the bright band at close ranges. The unadjusted radar QPE consistently shows an overestimation relative to rain gauges up to 60 km, followed by an underestimation likely due to the ice phase sampling. The VPR-IE using the TRMM-PR information mitigates this range-dependent error.

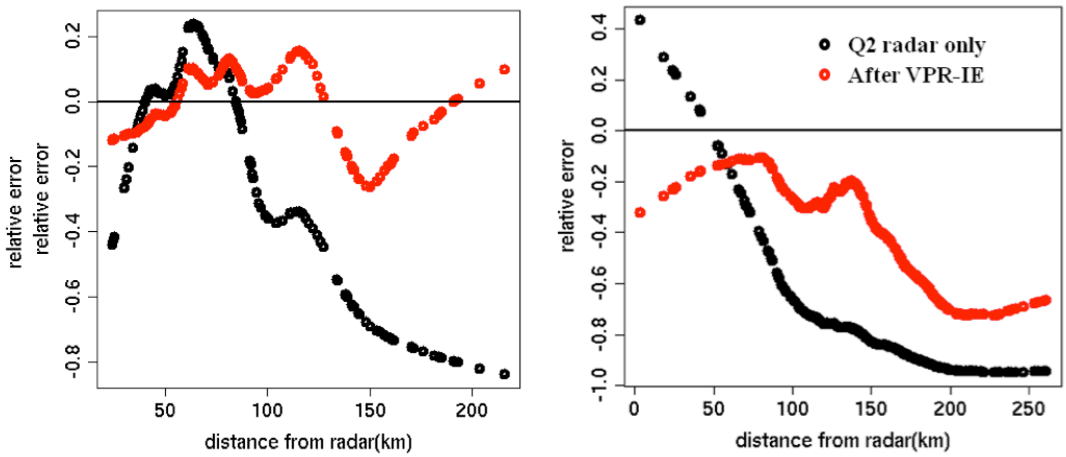

Figure 3.7. QPE error (multiplicative bias ((radar-raingauge)/raingauge ratios)) in terms of range for the 8 December 2009 case (left) and for the 22 January case (right).

References

Andrieu, H., and J. D. Creutin, 1995: Identification of vertical profiles of radar reflectivity for hydrological applications using an inverse method. Part I: Formulation. *J. Appl. Meteor.*, **34**, 225–239.

Bellon, A., G.-W. Lee, and I. Zawadzki, 2005: Error statistics of VPR corrections in stratiform precipitation. *J. Appl. Meteor.,* **44**, 998–1015.

Boudevillain, B., and H. Andrieu, 2003: Assessment of vertically integrated liquid (VIL) water content radar measurement. *J. Atmos. Oceanic Technol.,* **20**, 807–819.

Delrieu, G., B. Boudevillain, J. Nicol, B. Chapon, P-E. Kirstetter, H. Andrieu, and D. Faure, 2009: Bollène 2002 experiment: Radar rainfall estimation in the Cévennes–Vivarais region. *J. Appl. Meteor. Climatol.,* **48**, 1422–1447.

Fabry, F., and I. Zawadzki, 1995: Long-term radar observations of the melting layer of precipitation and their interpretation. *J. Atmos. Sci*., **52**, 838–851.

Gabella, M., J. Joss, G. Perona, and S. Michaelides, 2006: Range adjustment for ground-based radar, derived with the spaceborne TRMM Precipitation Radar. *IEEE Transl. Geosci. Remote Sens.*, **44**, 126-133.

Germann, U. and J. Joss, 2002: Mesobeta profiles to extrapolate radar precipitation measurements above the Alps to the ground level. *J. Appl. Meteor.,* **41**, 542-557.

Hardaker , A. R. Holt, and C. G. Collier, 1995: A melting layer model and its use in correcting for the bright band in single polarization radar echoes. *Quart. J. Roy. Meteor. Soc*., **121**, 495–525.

Iguchi, T., T. Kozu, R. Meneghini, J. Awaka, and K. Okamoto, 2000: Rain-profiling algorithm for the TRMM Precipitation Radar. *J. Appl. Meteorol*., **39**, 2038-2052.

Iguchi, T., T. Kozu, J. Kwiatkowski, R. Meneghini, J. Awaka, and K. Okamoto, 2009: Uncertainties in the Rain Profiling Algorithm for the TRMM Precipitation Radar. *J. Meteorol. Soc. Jpn*., **87**, 1-30.

Joss, J., and R. Lee, 1995: The application of radar-gauge comparisons to operational precipitation profile corrections. *J. Appl. Meteor*., **34**, 2612–2630.

Kirstetter, P., H. Andrieu, G. Delrieu and B. Boudevillain, 2010: Identification of Vertical Profiles of Reflectivity for Correction of Volumetric Radar Data Using Rainfall Classification. *J. Appl. Meteor. Climatol*., **49**, 2167-2180.

Kirstetter, P.E., H. Andrieu, B. Boudevillain and G. Delrieu, 2012: Toward a physically-based identification of vertical profiles of reflectivity from volume scan radar data. *IAHS Publ*. 351-16, in press.

Kitchen, M., 1997: Towards improved radar estimates of surface precipitation at long range. *Quart. J. Roy. Meteor. Soc*., **123**, 145–163.

——, R. Brown, and A. G. Davies, 1994: Real-time correction of weather radar data for the effects of bright band, range and orographic growth in widespread precipitation. *Quart. J. Roy. Meteor. Soc.*, **120**, 1231–1254. Klaassen 1988

Koistinen, J., 1991:Operational correction of radar rainfall errors due to the vertical reflectivity profile. Preprints, 25th Int. Conf. on Radar Meteorology, Paris, France, Amer. Meteor. Soc., 91–94.

Lakshmanan, V., A. Fritz, T. Smith, K. Hondl, and G. J. Stumpf, 2007: An automated technique to quality control radar reflectivity data. *J. Appl. Meteor. Climatol*., **46**, 288 ‑ 305.

Maddox, R., J. Zhang, J.J. Gourley, and K. Howard, 2002: Weather radar coverage over the contiguous United States. *Wea. And Forecast*., **17**, 927-934.

Matrosov, S. Y., K. A. Clark, and D. E. Kingsmill, 2007: A polarimetric radar approach to identify rain, melting-layer, and snow regions for applying corrections to vertical profiles of reflectivity. *J. Appl. Meteor. Climatol*., **46**, 154–166.

Pellarin, T., G. Delrieu, G.-M. Saulnier, H. Andrieu, B. Vignal, and J.-D. Creutin, 2002: Hydrologic visibility of weather radar systems operating in mountainous regions: Case study for the Arde`che catchment (France). *J. Hydrometeor*., **3**, 539–555.

Sellers, W. D., and R. H. Hill, 1974: Arizona Climate 1931-1972. The University of Arizona Press, 616 pp.

Sempere Torres, D., Porrà, J.M. and Creutin, J.-D., 1994. A general formulation for raindrop size distribution. *J. Appl. Meteorol*., **33**, 1494–1502.

Simpson, J., C. Kummerow, W.-K. Tao, and R. F. Adler, 1996: On the tropical rainfall measuring mission (TRMM). *Meteor. Atmos. Phys*., **60**, 19-36.

Smith, J. A., D. –J. Seo, M. L. Baeck, and M. D. Hudlow, 1996: An intercomparison study of NEXRAD precipitation estimates. *Water Resour. Res*., **32**, 2035-2045.

Smyth, T. J., and A. J. Illingworth, 1998: Radar estimates of rainfall rates at the ground in bright band and non-bright band events. *Quart. J. Roy. Meteor. Soc*., **124**, 2417–2434.

Szyrmer, W., and I. Zawadzki, 1999: Modeling of the melting layer. Part I: Dynamics and microphysics. *J. Atmos. Sci.,* **56**, 3573–3592.

Tabary, P., 2007: The new French operational radar rainfall product. Part I: Methodology. *Wea. Forecasting*, **22**, 393–408.

Vasiloff, S., and Coauthors, 2007: Q2: Next generation QPE and very short-term QPF. *Bull. Amer. Meteor. Soc.*, **88**, 1899–1911.

Vignal, B., and W. F. Krajewski, 2001: Large-sample evaluation of two methods to correct range-dependent error for WSR-88D rainfall estimates. *J. Hydrometeor.*, **2**, 490–504.

——, H. Andrieu, and J. D. Creutin, 1999: Identification of vertical profiles of reflectivity from volume-scan radar data. *J. Appl. Meteor.*, **38**, 1214–1228.

——, G. Galli, J. Joss, and U. Germann, 2000: Three methods to determine profiles of reflectivity from volumetric radar data to correct precipitation estimates. *J. Appl.Meteor.*, **39**, 1715–1726.

Vila, D. A., L. G. G. De Goncalves, D. L. Toll, and J. R. Rozante, 2009: Statistical evaluation of combined daily gauge observations and rainfall satellite estimates over continental South America. *J. Hydrometeor.*, **10**, 533–543.

Watson A. I., R. E. Lopez, and R. L. Holle, 1993: Diurnal Cloud-to-Ground Lightning Patterns in Arizona during the Southwest Monsoon. *Mon. Wea. Rev.*, **122**, 1716-1725.

Zhang, J., K. Howard, and J. J. Gourley, 2005: Constructing threedimensional multiple-radar reflectivity mosaics: Examples of convective storms and stratiform rain echoes. *J. Atmos. Oceanic Technol.*, **22**, 30–42.

Zhang J. and Y. Qi, 2010: A real-time algorithm for the correction of brightband effects in radar-derived QPE. *J. Hydrometeor.*, **11**, 1157- 1171.

Zhang. J., K. Howard, C. Langston, S. Vasiloff, B. Kaney, A. Arthur, S. V. Cooten, K. Kelleher, D. Kitzmiller, F. Ding, D. J. Seo, E. Wells, and C. Dempsey, 2011: National Mosaic and Multi-sensor QPE (NMQ) System: Description, Results, and Future Plans. *Bull. Amer. Meteor. Soc.*, **92**, 1321–1338.

Chapter 4 Real time climatological VPR_IE

The VPR_IE approach demonstrates the benefits of integrating the TRMM/PR products into NEXRAD ground-based radar rainfall estimation system. However, the insufficient temporal resolution of TRMM limits the application of VPR-IE method operationally. In order to implement the VPR-IE concept into the MRMS system in real-time fashion, we have characterized Climatological VPRs from 11-year TRMM PR observations for different stratiform/convective rain types, seasons, and surface rain intensities, then integrated the suitable climatological VPR information to the NMQ system based on different precipitation structure. This Chapter gives a detailed description of the proposed real-time VPR-IE system, with performance evaluation in Arizona and south California where NEXRAD radar QPE is typically degraded by the lack of near-surface radar observations. The system's promising performance and the potential error sources are discussed as well via a comprehensive evaluation on events in winter (January, February, and December) in 2011 in terms of radar beam height, radar quality index and proportional precipitation types.

4.1 Climatological VPRs from TRMM/PR

The VPR characteristics improve our understanding of the vertical structures of storms and provides for inferences of dominant microphysical processes. If a representative VPR is known for the different precipitation types, then surface rainfall can be much better estimated with ground radar observations, even for situations where the beam intercepts or overshoots the melting layer. This section gives a description of the spatially and temporally representative VPRs from more than 11 years TRMM/PR observation.

4.1.1 TRMM/PR more than 10 years observation

For the past 15 years, scientists all over the world has been put much effort into generating state-of-the-art radar-precipitation products with TRMM PR (e.g., Meneghini et al. 2000, 2004; Iguchi et al. 2000, 2009; Schumacher and Houze 2003; Takahashi and Iguchi 2004; Seto and Iguchi 2007; Awaka et al. 2009). Three levels of algorithm are used to process TRMM products. Level 1 algorithm calculates the basic radar products, such as radar raw reflectivity and deals with data quality control and calibration. Level 2 algorithms generate the products associated with the radar signal processing and the physical processes of storms. Level 3 algorithms provide 3 hourly gridded dataset averaged from Level 1 and Level 2 products temporally and spatially. The datasets used for analyzing the climatological VPRs were from two Level 2 products: PR qualitative algorithm (2A23) and PR profile algorithm (2A25). 2A23 data include products for brightband detection and quantification, and precipitation type classification (Awaka et al. 2007, 2009). 2A25 data provide range profiles of attenuation-corrected radar reflectivity and corresponding rainfall estimation (Meneghini et al. 2000, 2004; Iguchi et al. 2000, 2009).

The TRMM science team has released several versions of data-processing algorithms since the launch of TRMM satellite in 1997. The latest version of TRMM algorithms, version 7 (TRMM V7), was released in September 2011 (TRMM Precipitation Radar Team 2011). Compared to the version 6 released in 2004, TRMM V7 have introduced improvements (e.g., Seto and Iguchi 2007; Awaka et al. 2009; Iguchi et al. 2009). For example, the 2A23 algorithm now better detects the bright band and shallow storms. It has also increased the rain type subcategories and refines the

classification. The 2A25 algorithm produces enhanced radar reflectivity profiles by improving path-integrated attenuation (PIA) estimation and refining the attenuation correction method. Rain estimation is now improved with the introduction of a new drop size distribution (DSD) model. Nonuniform beam filling (NUBF) correction was also reintroduced in V7.

The data used to generate climatological VPRs are from 1 January 2000 to 26 October 2011. According to the surface rain gauge measurements, the total number of rainy days in the analysis region is 1751. However, because of the mismatch of time and space between the PR scan and the evolution of storms, PR observed879 event, which are 3123 passes with total rainfall rate in the research area greater than 10 mm/hr. Cao et al (2013) gave a table to illustrate more details about the data availability (see table 5). The monthly analysis indicates there are many fewer precipitation events occurring in May and June than in July and August, which is attributed to the onset of the North American monsoon.

Table 5. TRMM V7 data (2A23, 2A25) availability by month, where the numbers in the first row indicate the month. (from Cao et al., 2013, Table 1)

	1	2	3	4	5	6	7	8	9	10	11	12	Total
Rain events	148	161	166	117	85	65	198	247	167	149	100	148	1751
Observed events	71	74	68	47	42	38	125	143	87	74	43	67	879
PR passes with rain	216	271	224	137	107	125	531	609	329	248	130	196	3123

4.1.2 Data processing

VPRs vary with different storm types, different rain intensities and different seasons. To accurately depict the climatological VPRs characteristics, all VPRs observed by PR were broken down to different categories. We first separated all data to stratiform and convective rain types. V7 of 2A25 applies more than 30 subcategories for

the classification of rain types. In general, these 30 subcategories can be summarized to 5 major types: “stratiform certain”, “stratiform maybe”, “convective certain”, “convective maybe”, and “others”. The stratiform type is identified when the bright band (BB) is clearly detected and the VPR reveals apparent features of stratiform precipitation. When the BB does not exist and the VPR reveals convective characteristics, the precipitation will be classified with the convective type. When the BB is not clearly detected the precipitation will be assigned as either convective maybe or stratiform maybe, with the latter distinction being tied to the precipitation structure. Cao et al., (2013) combined the convective maybe type into the convective type for the data analysis.

Seasonal VPR variations are also considered. PR data collected in spring (March, April, May), summer (June, July, August), autumn (September, October, November), and winter (December, January, February) have been processed and composited separately. Considering that surface rainfall of different intensities may be related to different VPR features, the PR data have also been sorted into 24 categories with surface rainfall rate varying from 0.4 to 80 mm/hr. The mean VPR is created with VPRs having the surface rainfall rate with a 20% variation. For example, VPRs with rainfall rates 8-12 mm/hr are sorted and averaged to obtain representative VPR of 10 mm/hr. To reduce the dominant effect of high reflectivity values, the calculation of mean VPR is in the logarithm domain (dBZ). Figure 4.1 provides representative mean VPRs for stratiform precipitation that have been normalized by reflectivity at a reference height. The horizontal axis represents the ratio of reflectivity (dBZ) to the reference value observed 1 km below the height of the BB peak. Light precipitation has a larger ratio

within the melting layer and in the ice region above. This result suggests weaker stratiform precipitation is associated with lower aggregation rates of ice-snow particles above the freezing level and its relatively stronger BB signal may cause further contamination when estimating surface rainfall rates. In addition, the smaller ratios noted below the reference height with light stratiform precipitation indicates that evaporation rates are more influential on the rain slope. For stratiform precipitation with rainfall rates of greater than 7 mm/h, VPR ratios in the ice–snow aggregation region and melting layer are very similar, suggesting that the VPR structures for heavy stratiform rain tend to be less variable and are thus more predictable. Seasonal variations of stratiform VPRs for a given rainfall rate class are also slight and largely negligible. These results are encouraging for VPR correction methodologies for ground-based radars in that the local VPR, when normalized and segregated to the reference value below the BB, appear to be consistent from season-to-season for stratiform precipitation.

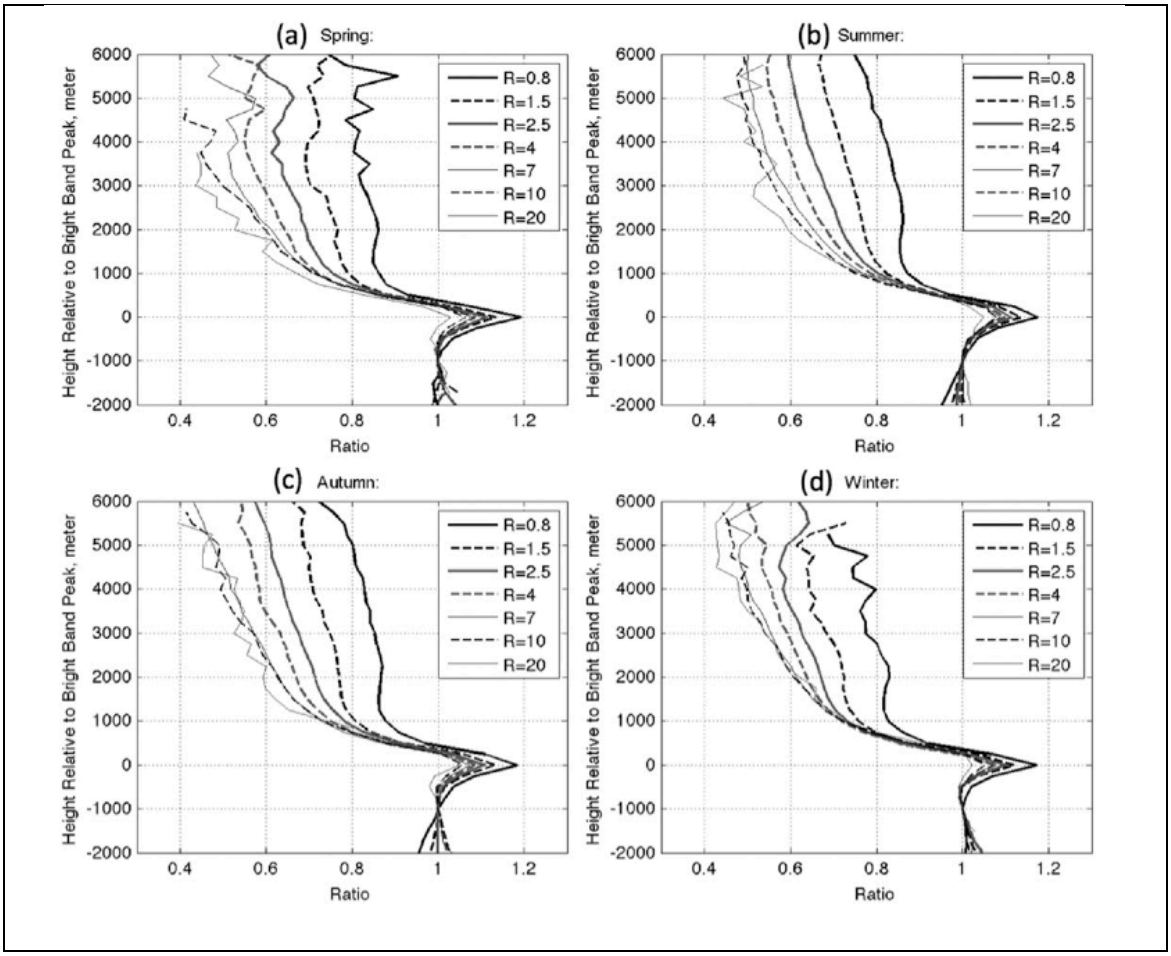

Figure 4.1. Normalized VPR shape for stratiform precipitation with different rainfall rates for (a) – (d) the four seasons (from Cao et al., 2013, Fig. 12) .

4.2 Climatological VPR_IE implementation

The current study proposes an enhanced VPR-IE scheme, which applies climatological VPR models to improve ground-radar QPE. The proposed VPR-IE scheme integrates the National Mosaic and Multi-sensor QPE (NMQ) system [17] and NASA's TRMM-PR products. A real-time system of this VPR-IE scheme is being constructed at OU and is expected to provide near-real-time, CONUS-wide, enhanced QPE products to users and researchers in the radar, satellite, meteorology and hydrology communities. This section gives a detailed description of the proposed real-time VPR-

IE system, with performance evaluation in Arizona where NEXRAD radar QPE is typically degraded by the lack of near-surface radar observations.

Different physical processes are associated with the different state of hydrometeors at various heights in a precipitation system (Fig. 4.2). Solid particles above the 0 °C isotherm normally give a radar reflectivity much lower than liquid drops (below the melting layer) for the same water content. On the other hand, the melting layer is typically associated with BB signals (enhanced radar reflectivity). Therefore, overshooting (or intercepting) the melting layer by the radar beam may lead to an underestimation (or overestimation) of the near-surface precipitation. Given beam blockages in mountainous regions, this kind of overshooting (or intercepting) is common for ground radars.

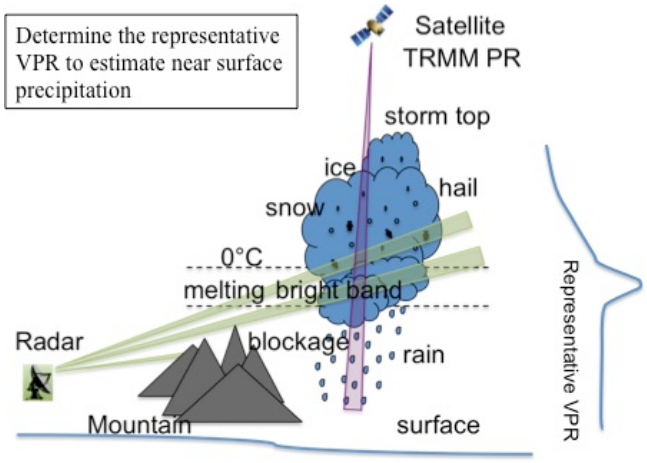

Figure 4.2. Illustration of using spaceborne radar measured representative VPR to improve the near-surface QPE based on ground-radar. Different physical processes associated with different state of hydrometeors at various heights are also shown in the figure.

As illustrated in Fig. 4.2, the VPR measured by spaceborne radar reveals the complete vertical structure of precipitation, linking ground-radar measurements aloft to the near-surface precipitation. Given a representative VPR, the ground-radar QPE can

certainly be improved by considering the vertical structure of hydrometeor phase. This is the basis of the VPR-IE method. Correspondingly, characterizing the representative VPR is one of the major tasks for VPR-IE.

Figure 4.3 shows the framework of the proposed real-time VPR-IE system. The VPR-IE system incorporates NMQ and TRMM products in real-time through the links connecting data servers at the National Severe Storms Laboratory (NSSL) and NASA Precipitation Processing Systems (PPS). As for VPR correction, 3D radar mosaic (S-band 3D reflectivity) and TRMM-PR products (2A25 and 2A23) are the primary inputs.

2A25 includes PR-measured Ku-band 3D reflectivity. 2A23 provides the precipitation type identification (stratiform or convective), detection of the melting layer, and quantities such as the height of BB peak, the height of freezing level, etc. The improved near-surface QPE is evaluated by rain gauge measurements and the results are provided to users via a web-based data delivery system.

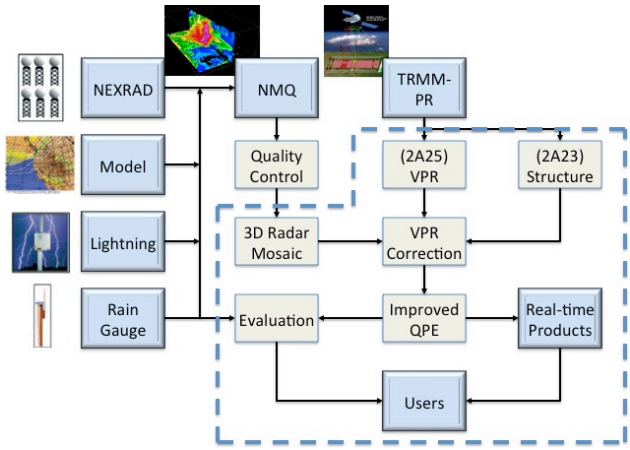

Figure 4.3. Framework of proposed VPR-IE system at OU. The major components associated with VPR correction are enclosed by dashed lines (from Cao et al., 2014).

4.2.1 Ku-band to S-band conversion

The scattering characteristics of hydrometeors at different frequencies may lead to different VPRs. In order to use Ku-band VPR to correct S-band VPR, a conversion from Ku-band to S-band should be applied. Our previous works have introduced two approaches: VPR model approach (Kirstetter, 2013) and empirical conversion (Cao, 2013).

Wen et al., (2013) has presented a physically-based VPR model, which assumes five parameters (cloud top, freezing level height, melting layer width, rain region VPR slope, and ice density factor) to compute a VPR. The model parameters are fitted from observed VPR using nonlinear regression. This method is computationally expensive for real-time data processing.

Cao et al. (2013) have derived a set of empirical relations for hydrometeors of different types or phases (snow, ice/hail, raindrop, melting particle). Radar dual-frequency ratio (DFR, unit in dB), which links Ku-band and S-band reflectivity (Z, unit in dBZ), can be computed from Ku-band reflectivity using polynomial relations. Coefficients a0…a4 have different values, depending on the type and phase of hydrometeors.

$$Z(\mathrm{S}) = Z(\mathrm{Ku}) + \mathrm{DFR} \quad \text{.....(4.1)}$$

$$\mathrm{DFR} = a_0 + a_1 Z(\mathrm{Ku}) + a_2 Z(\mathrm{Ku})^2 + a_3 Z(\mathrm{Ku})^3 + a_4 Z(\mathrm{Ku})^4 \quad \text{.....(4.2)}$$

The empirical conversion is computationally efficient and easily implemented. The detailed conversion procedure and the coefficients in empirical relations can be found in (Cao et al., 2013).

4.2.2 Apparent VPR at Different Radar Ranges

VPR measurements from ground radar may be degraded (i.e., having a worse vertical resolution) by the beam broadening effect, especially at far range(Tabary et al, 2007; Matrosov et al, 2007; Zhang et al, 2007). Smoothing of the VPR may lead to an incorrect quantification of physical processes. The smoothed VPR is normally regarded as the apparent VPR (AVPR) (Zhang et al, 2010). Generally, VPR measurements from TRMM-PR are unaffected by the beam broadening effect in the vertical direction (Cao et al, 2013). The derived S-band VPR from TRMM-PR measurements (as addressed in section II.A) should be converted to the AVPR to match ground-radar measurements at different radar ranges (Wen et al, 2013). To obtain the AVPR, a Gaussian function is used by VPR-IE to smooth the representative VPR. Given a specific radar range, the width of the Gaussian function is determined by the 3-dB radar beam width.

4.2.3 Climatological VPRs for VPR Correction

The proposed VPR-IE system applies climatological VPRs derived from long-term PR observations (Cao et al, 2013) to correct the radar QPE that has been degraded. Using the empirical conversion approach in (Cao et al, 2013b), the VPR statistics in (Cao et al, 2013a) have been repeated to obtain the S-band climatological VPRs for the proposed VPR-IE system (as shown in Fig. 4.4). The climatological VPR $z(h)$ is represented by the ratio of VPR to the reflectivity value at a reference height h_0.

$$z(h) = Z(h)/Z(h_0) \tag{4.3}$$

where, Z is in linear units; h is the height of radar beam center. The h_0 is assumed as 1.5 km below the freezing level. As Fig. 4.4 shows, climatological VPRs are classified by different seasons and near-surface reflectivity values in dBZ.

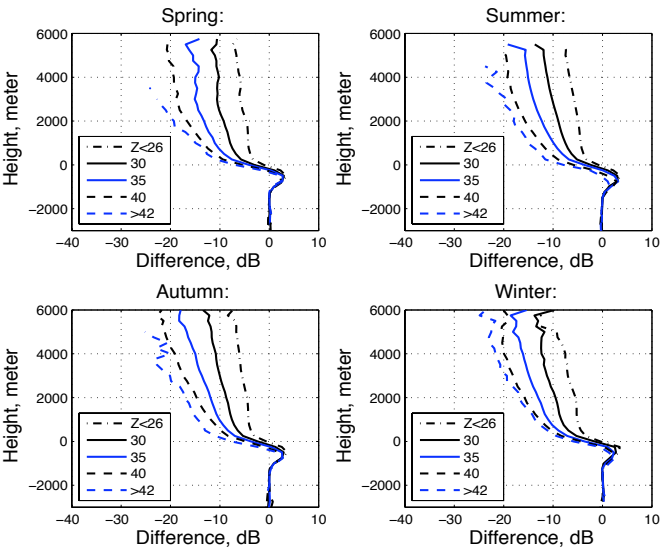

Figure 4.4. S-band climatological VPRs. Y-axis denotes the height relative to the freezing level.

4.2.4 Procedure for Real-time Implementation

The procedure of real-time climatology-based VPR correction is shown in Fig. 4. Since climatological VPRs have been quantified for S-band, the Ku-to-S-band conversion is no longer required for real-time processing. However, given a specific location, the appropriate climatological VPR needs to be determined for constructing the representative VPR. Firstly, the current VPR-IE system only corrects the VPR for stratiform precipitation. The identification of stratiform is mainly based on the real-time NMQ product of precipitation type. Note that BB contamination sometimes can be misidentified as convective precipitation by NMQ. As a result, the VPR-IE system further examines the radar beam height and the freezing level to reduce this uncertainty. Secondly, the climatological VPRs have been quantified with the near-surface reflectivity, which correspond to different rain intensities. The VPR-IE system applies a self-consistency method, i.e., estimating the near-surface reflectivity with all the

climatological VPRs and then checking if the result is consistent with the assumed reflectivity category. The selected climatological VPR is then combined with the real-time freezing level height to take into account the local variation of a storm as well as the underlying terrain. Considering the low revisit frequency of the TRMM satellite, the real-time freezing level data are adapted from NMQ. The VPR-IE system also updates the freezing level whenever the TRMM satellite passes over the region. Combining climatological VPRs and real-time freezing level data provides representative VPRs for different locations. Considering different radar ranges, representative VPRs are converted to the AVPRs, which are combined with ground-radar measurements to estimate the near-surface reflectivity. Consequently, the near-surface QPE can mitigate the underestimation (or overestimation) caused by pristine ice (or melting ice) signals in original ground-radar measurements. Although the spatial pattern of a VPR in an event may be different from the result of long-term statistics, the current VPR-IE system has ignored the spatial variability of VPRs and generally relies on the shape of the climatological VPR and the spatial pattern of the real-time freezing level height.

4.3 Comprehensive Evaluation of CVPR_IE

A variety of studies have investigated different approaches to obtain representative VPRs. There are generally two categories: (1) those rely on ground radar data or other surface observations to derive VPRs (Kitchen et al. 1994; Andrieu and Creutin 1995; Fabry and Zawadzki 1995; Vignal et al. 1999; Germann and Joss 2002; Tabary 2007; Borga et al. 2000; Kirstetter et al. 2010; Zhang and Qi 2010; Kirstetter et al. 2013). However, in mountainous regions, complete VPRs may be difficult to obtain. Another approach (2) investigates the vertical structure of precipitation using

spaceborne radar (Gabella, et al 2006; Wen et al 2013; Cao et al 2013a; Cao et al 2013b), i.e., precipitation radar (PR) onboard National Aeronautics and Space Administration (NASA)'s Tropical Rainfall Measuring Mission (TRMM) satellite. Building on the works proposed by Kirstetter et al. (2012, 2013), Wen et al. (2013) proposed a concept of QPE enhancement, namely the VPR Identification and Enhancement (VPR-IE), which derives a representative, parameterized VPR using PR observations when a local PR pass is available.

The VPR-IE method has been evaluated for several stratiform precipitation events in Arizona. The statistical analysis showed that VPR-IE effectively enhanced ground radar-based QPE but this improvement was limited to times in which there were PR overpasses. Cao et al (2013a) summarized the statistical seasonal, spatial, intensity-related, and type-related characteristics of the vertical structure of precipitation in the region of southern California, Arizona, and western New Mexico through the use of 11+ years of TRMM PR observations. These climatological VPRs can now be integrated into a real-time multisensor scheme.

4.3.1 Data and methodology

Our study area is the Mountainous West region of the U.S. (Fig. 4.5), where ground weather radar QPE is challenging because of insufficient NEXRAD radar coverage and high spatial variability of precipitation due to orographic enhancements. In winter, the relatively shallow precipitating clouds make accurate QPE at the surface level even more difficult. VPR correction improves the surface precipitation estimation by considering the vertical structure of hydrometeors and thus linking surface precipitation to the radar measurements aloft. Wen et al. (2013) used a physically based

VPR model (Kirstetter et al. 2013) to identify and utilize PR-measured VPRs. The physically based VPR-IE method depends on the availability of PR measurements, which is limited to twice daily from the TRMM satellite orbits.

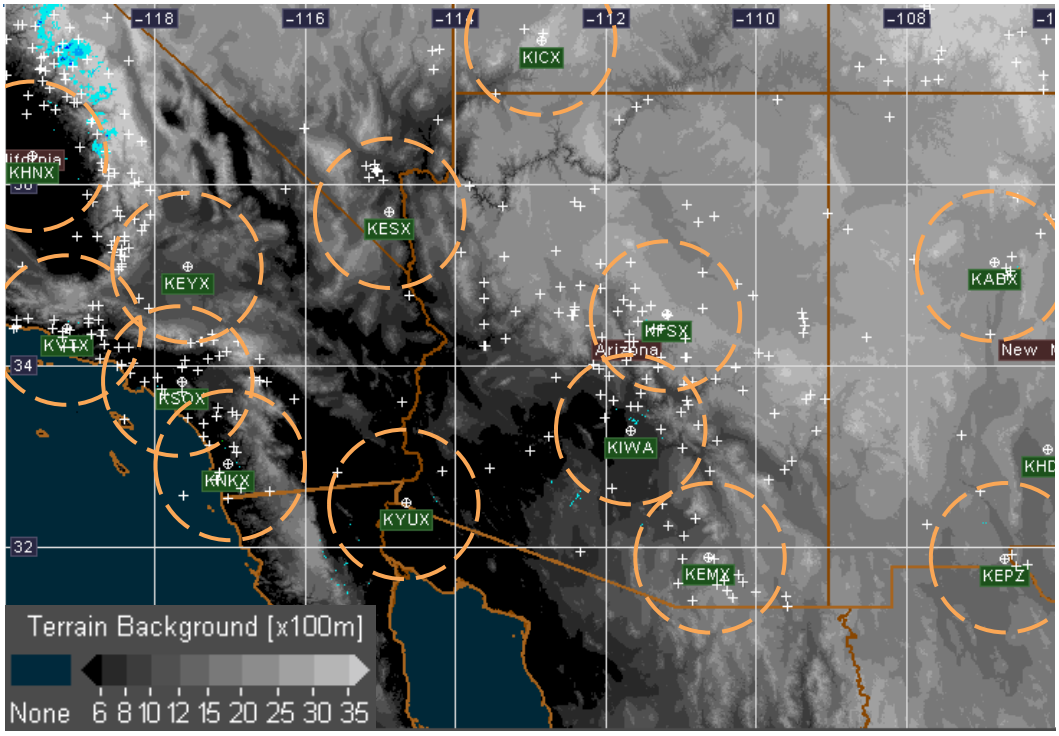

Figure 4.5. An image showing the topography of the study area and the locations of rain gauges (white crosses) and WSR-88D radar sites (white circles with cross) with 100-km range rings.

Cao et al. (2013) derived climatological VPRs from long-term PR measurements for different seasons, rain intensities and convective/stratiform rain types. Since the scattering of hydrometeors depends on frequency, the Ku band climatological VPRs derived from PR measurements have different features compared to S-band VPRs. A conversion from Ku band to S band needs to be applied when the TRMM-based VPR-IE is implemented for ground based radar measurements. A radar dual-frequency ratio

was derived from Ku-band using a set of empirical relations for different hydrometeors (snow, ice/hail, rain, melting particles) and applied to link Ku-band reflectivity to S-band reflectivity (Cao et al, 2013). The S-band climatological VPRs for the cool season are shown in Fig. 4.6. The climatological VPR is represented by the ratio of VPR to the reflectivity value at a reference height, which is set to 1.5 km below the freezing level. This reference height corresponds to liquid hydrometeors that have just melted.

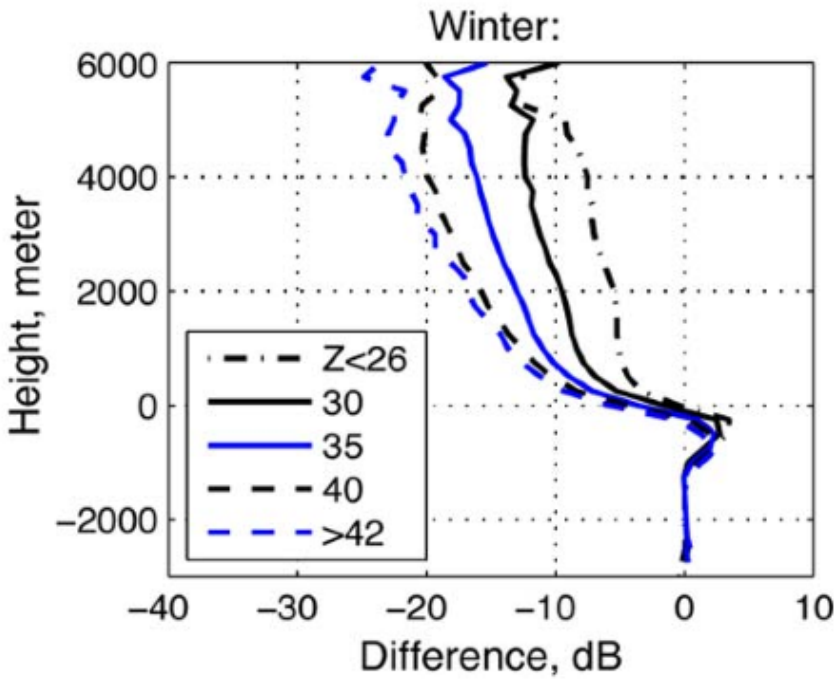

Figure 4.6. Climatological VPRs (already converted from Ku-band) for winter season from 11-year TRMM/PR observations. X-axis denotes the difference relative to the reflectivity measured at 1 km below freezing level. Y-axis denotes the height relative to the freezing level.

The procedure for real-time climatology-based VPR correction is shown in Fig. 4.7. First, stratiform precipitation is identified based on the real-time NMQ precipitation type product. The CVPR-IE is developed for stratiform precipitation, but it is also applied to NMQ-identified convective echoes for situations where the radar beam height is sampling within the melting layer. Second, the surface rain intensity from

NMQ is used to select the appropriate climatological VPR. Third, the selected climatological VPR is then combined with the real-time freezing level height from NMQ to account for local storm structures and the underlying terrain effects. Fourth, representative VPRs are convolved with ground radar sampling properties (e.g., beam broadening with range) to compute the apparent VPRs (AVPRs) at different radar ranges. Finally, the correction is applied to the reflectivity field, which is then converted into rainfall rate using Z-R relations: $Z=200R^{1.6}$ for stratiform rain and $Z=300R^{1.4}$ for convective rain. The rainfall rates are then accumulated to hourly rainfall amounts and compared to rain gauge observations. The focus of this paper is on the assessment of the approach. More details of CVPR-IE are discussed in Cao et al. (2014).

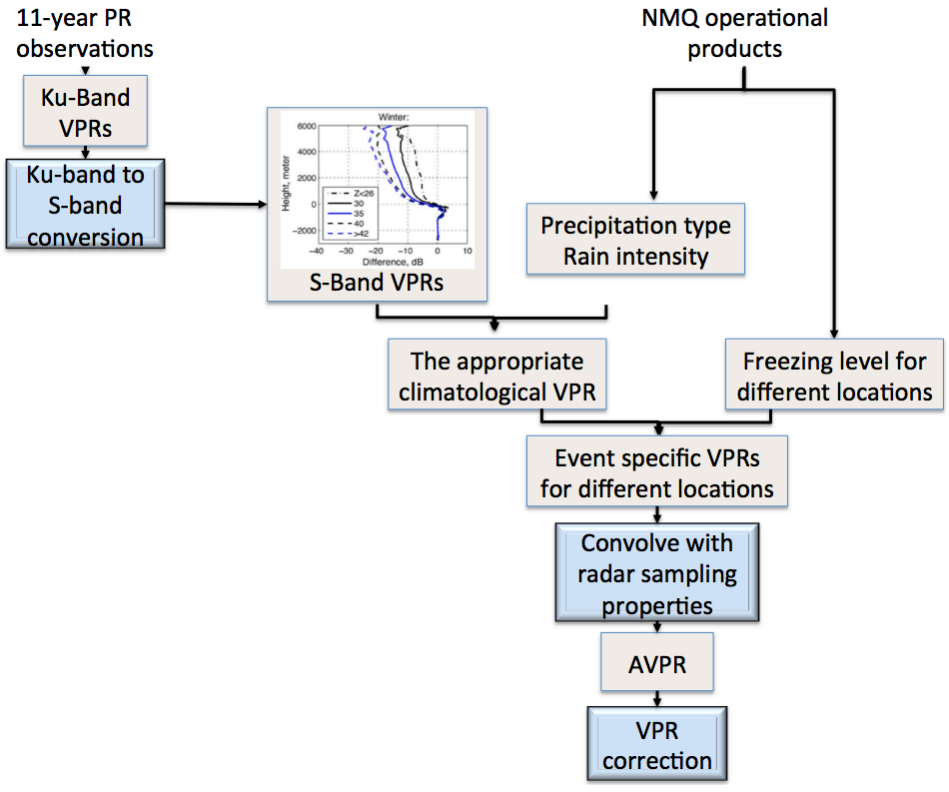

Figure 4.7. Procedure of real-time climatology-based VPR correction.

4.3.2 Results

a. Verification statistics

We select four statistical indices for evaluating CVPR-IE using rain gauges comprising the Hydrometeorological Automated Data System (HADS) network as the reference (Fig. 4.5). The Relative Bias (RB; in percent) is used to assess the systematic bias of radar estimations. Spearman's rank correlation coefficient (CC) is used to assess the agreement between the radar estimates and gauge observations. The mean absolute error (MAE) measures the average magnitude of the error while the root-mean-squared error (RMSE) quantifies the average error magnitude, giving more weight to larger errors:

$$RB = \frac{\sum R(i) - \sum G(i)}{\sum G(i)} \times 100\%, \tag{4.4}$$

$$CC = 1 - \frac{6\sum\left(Rank_{R(i)} - Rank_{G(i)}\right)^2}{n(n^2-1)}, \tag{4.5}$$

$$MAE = \frac{\sum|R(i) - G(i)|}{n}, and \tag{4.6}$$

$$RMSE = \sqrt{\frac{\sum(R(i) - G(i))^2}{n}} \tag{4.7}$$

In (2), RankR(i) and RankG(i) represent the assigned rank value in the ascending order of the radar and gauge observation, respectively. Statistics are computed in Table 6 for hourly rainfall estimates after filtering out all points that have a frozen precipitation type according to the NMQ algorithm. Data pairs with nonzero values from both gauge and radar sources are considered as the correction is focused on quantitative measurement rather than detection.

Table 6. Statistical results of the climatological VPR_IE approach. The first row shows the statistics before CVPR_IE correction; the second row shows the statistics after CVPR_IE correction.

	RB (%)	CC	MAE (mm)	RMSE (mm)	Sample Size
Before	-46.43	0.34	1.33	2.25	14627
After	-39.97	0.35	1.30	2.25	14627

The statistics show improvement with the CVPR-IE method according to all statistical indices except RMSE. To evaluate the significance of the improvement and minimize the impact of the sample representativeness, a bootstrap method is implemented by recomputing statistics on the basis of different samples. Efron (1979) introduced the bootstrap method with the idea that the sample values generated by resampling from the original sample repeatedly are the best guide to the true distribution. Based on these bootstrap samples, estimates of the statistical values (bias, CC, etc.) can be derived. Figure 4.8 shows the probability distribution of statistical parameters derived from 1000 groups of bootstrap samples. Note that a summary statistic fluctuates from sample to sample. In general, all statistical values have improvements with statistical significance after the CVPR-IE correction except RMSE. Relative bias (RB) has the largest improvement with the mode of the distribution of RB shifting from -46% to -40%. The mode of the CC distribution has shifted to higher values following correction and the MAE distribution has shifted to lower values, which means rainfall estimates are more consistent with rain gauge measurements after correction. Fig. 4.8d shows a slight trend of RMSE shifting towards lower values, but not significantly. Further analysis of improvements due to CVPR-IE concentrates on RB, CC and MAE.

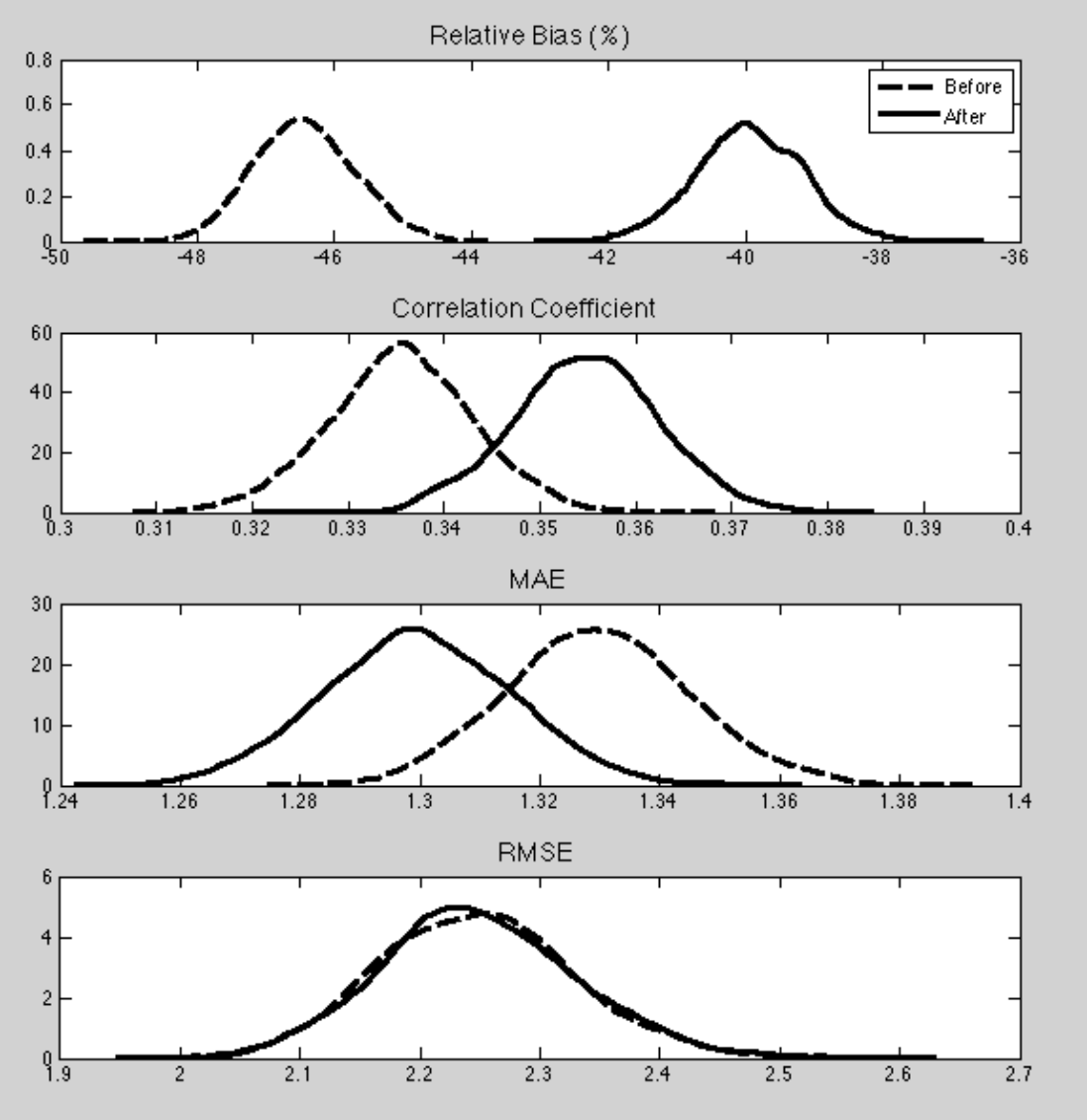

Figure 4.8. The probability distribution of RB, CC, MAE and RMSE using bootstrapping method.

The dependence of the distributions of the statistical values on sample size is shown in Fig. 4.9. Figure 4.9 shows the median of the distribution and the interquartile range for the statistics computed on the uncorrected radar data and then the CVPR-IE method. The breadth of the distributions of the statistics in Fig. 4.9 show a narrowing with larger sample sizes as expected. All statistical indices except RMSE show

improvements for all sample sizes. There is a consistent ~6% improvement in RB performance independent of sample size due to the correction method. It is notable that the consistent improvements are based on hourly scale. These improvements may amplify further if assessed at daily scale. Also, other uncertainties associated with radar calibration, Z-R relation, etc. may mask CVPR_IE's performance. These uncertainties are discussed in the discussion section.

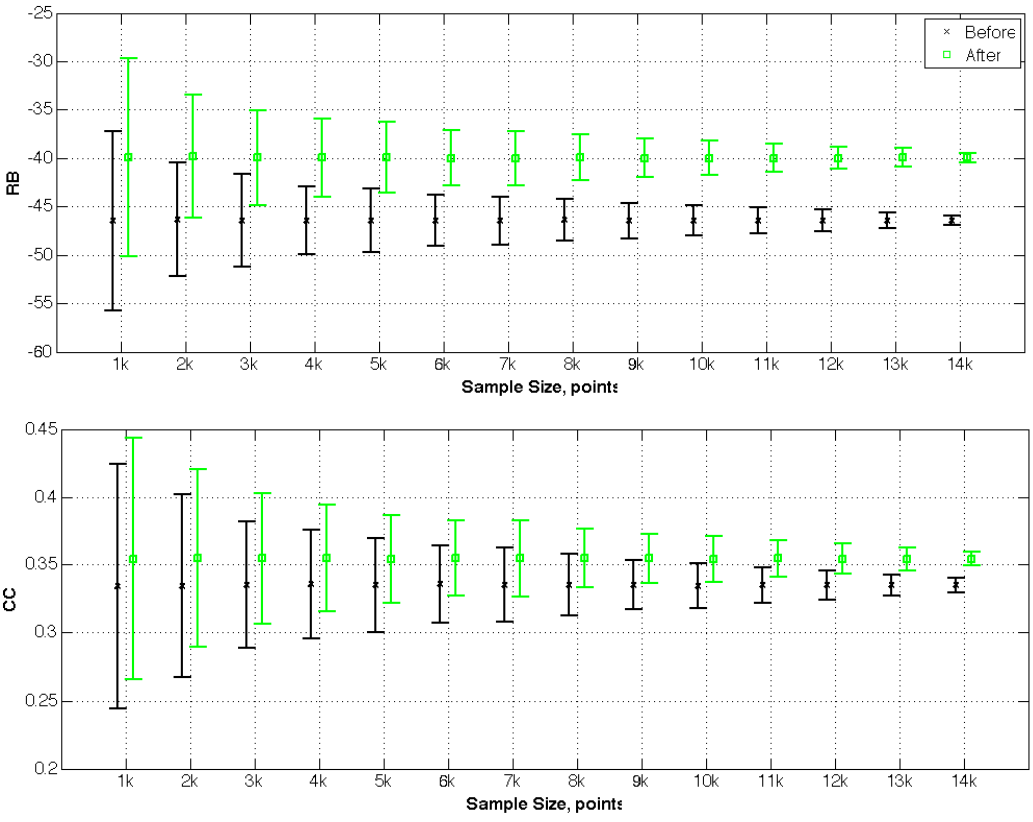

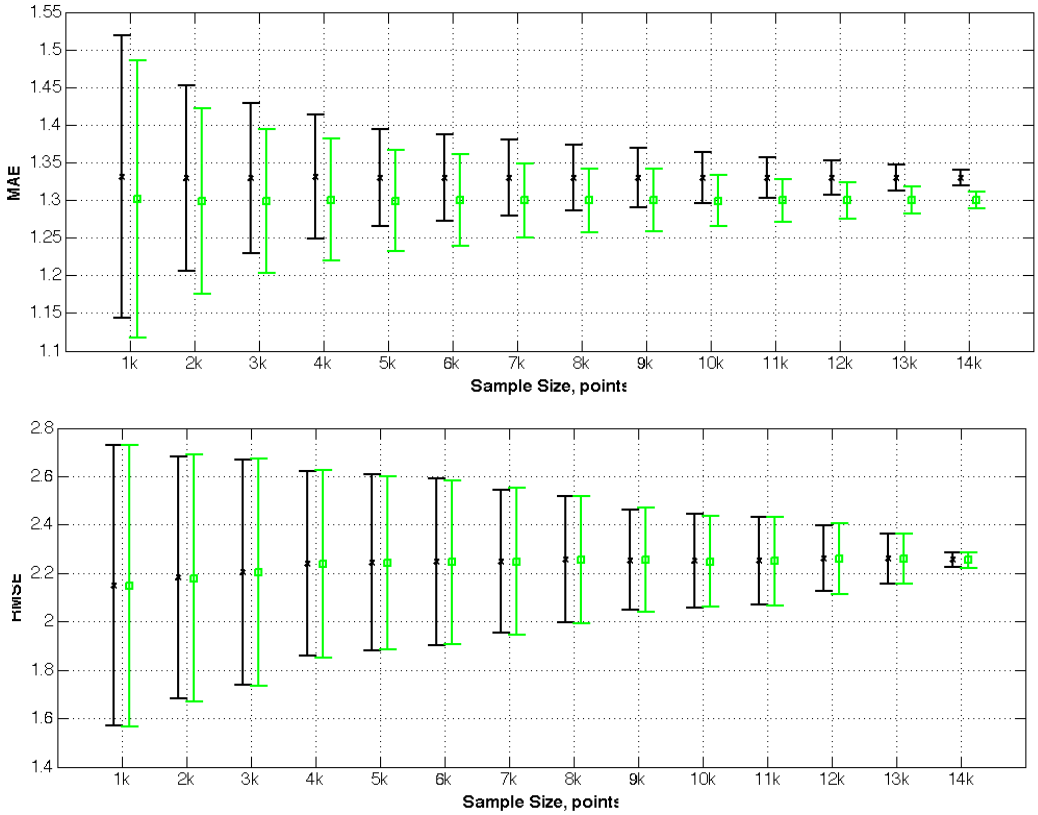

Figure 4.9. The statistics before and after CVPR_IE for a range of sampling sizes. The whiskers refer to the interquartile range.

The statistics shown in Figs. 4.8 - 4.9 are aggregated over a large sample size and cannot highlight the improvement in skill for each data pair following correction. In order to evaluate if the radar estimates are in better agreement with gauge measurements in terms of occurrence of improvement after correction, we apply a difference method similar to Bellon (2006).

$$I_i = |\text{QPE_before}_i - \text{Gauge}_i| - |\text{QPE_after}_i - \text{Gauge}_i| \quad (4.8)$$

, where i indicates the ith gauge-radar pair; QPE_before represents the raw, radar-based estimate while QPE_after is for the corrected QPE following the CVPR_IE application. If $I_i > 0$, then the radar measurement after correction agrees better with

gauge measurements and the reverse is true for $I_i<0$. The occurrences of positive and negative values are counted and the results are plotted as a function of gauge-based rainfall accumulation in Fig. 4.10. The dashed line indicates that the improvement after correction is consistently better than the radar-only product when the surface hourly rainfall is less than 5 mm. It must be noted that the average stratiform rain rates are typically less than 4 mm/hr (Schumacher and Houze, 2003). Consistently higher occurrences of better performance due to CVPR-IE indicate good correction skill in stratiform regions since the correction method focuses on stratiform regions. In convective regions, where hourly rain rates are commonly greater than 4 mm/hr, the number of points for which the rainfall estimates has deteriorated after correction is similar to the occurrences for which the rainfall estimates have improved after correction. Stratiform and convective echoes have different VPR characteristics. VPRs in convective precipitation have less vertical variability without a bright band feature in relation to stratiform echoes. Thus, the current CVPR-IE focuses on stratiform precipitation and shows improvements over a majority of data pairs.

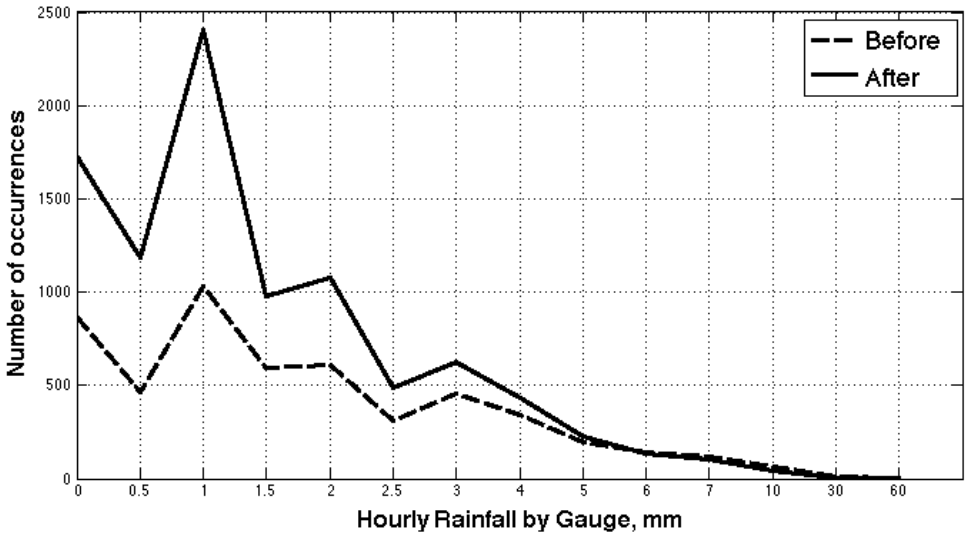

Figure 4.10. The occurrences of improved QPE after correction based on gauge measurements is denoted as dashed black line; the occurrences of worse QPE after correction is denoted as solid line.

b. Verification with radar beam height

Systematic errors in ground-based radar rainfall estimation, related to the VPR features combined with the geometric effects of the radar beam, creates the often-noted radar beam height dependence (Bellon et al. 2005). Figure 7 shows statistics before and after correction as a function of radar sampling height. The uncorrected QPE at near range shows high CC values and low MAE values indicating the radar QPE is highly consistent with rain gauge measurements. The CC and MAE worsen as radar beams approach and then intercept the melting layer. Both statistics either improve or stay constant for 2000 m above the melting layer before deteriorating again above this height. Reflectivity in the melting layer is not well correlated with surface rainfall rates. Regarding the RB, both uncorrected and CVPR-IE-corrected rainfall slightly underestimates gauge accumulations instead of overestimating it in the melting layer. The CVPR-IE correction technique detects the melting layer region and automatically subtracts an offset of reflectivity between the bright band and the liquid rain region as observed in the climatological VPRs (Fig. 4.11). The unusual underestimation in the melting layer region is further underestimated after the VPR correction is applied. We note that there is a negative RB (-50%) for the uncorrected rainfall at the reference level; i.e., where we expect the best accuracy in rainfall estimates. The method is designed to adjust radar estimates so that they represent rainfall at the reference level height. If the rainfall estimates are biased there, then the bias will propagate for corrections applied at

greater sampling heights. We discuss in the Discussion Section that such biases may be due to an inaccurate Z-R relationship, which tends to mask the improvement in the CVPR-IE method. The overshooting of the radar beam in the ice phase causes the CC to drop significantly for radar beam heights greater than 2000 m above the melting layer. The MAE decreases in this region, but only because the quantitative radar and gauge rainfall amounts are becoming quite light in this region. The significant decrease of the CC means that the data may not be correctable at these heights due to a very poor correlation with surface rainfall. This places an upper limit to which the CVPR-IE can be effective in shallow, stratiform rain. Overall, the CVPR-IE using the climatological PR information mitigates the underestimation above the freezing level by improving the RB by 30%. CC and MAE are slightly improved in the ice region.

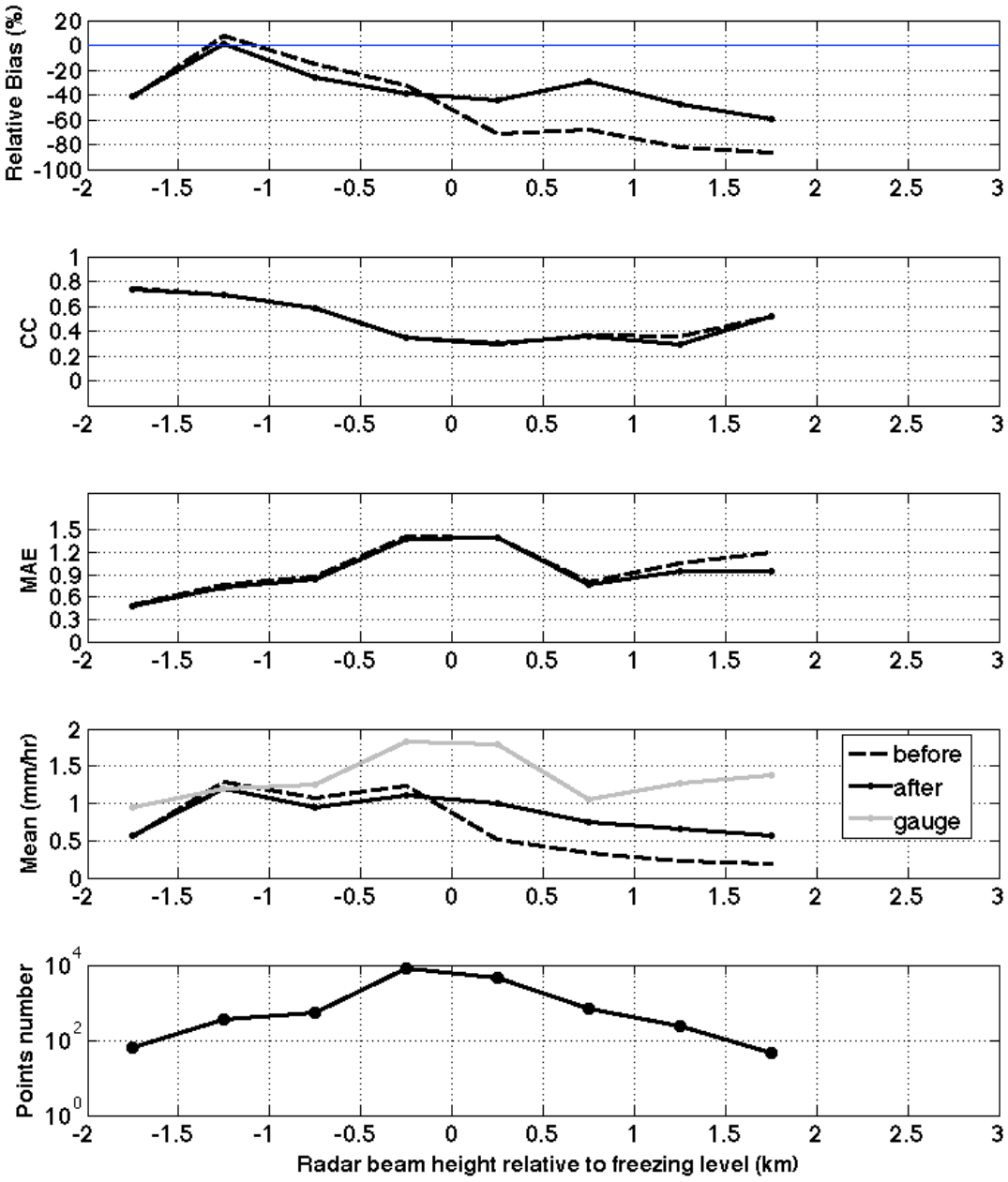

Figure 4.11. The range-dependent statistics of beam height relative to freezing level. The dashed lines denote radar only rain estimation before correction; the black lines denote rain estimation after CVPR_IE; the gray line denotes rain gauge measurements on the ground.

c. Verification with RQI

The NMQ system provides a Radar Quality Index (RQI) product to account for radar beam sampling characteristics (i.e., partial blockage, beam height relative to melting layer, and sampling volume) (Zhang, et al., 2011). The RQI field ranges from zero to unity, indicating the relative quality of the radar QPE from low to high. Sheng et al. (2013) evaluated daily NMQ rainfall accumulations and found that the bias was correlated with RQI values. Figure 4.12 shows the CVPR-IE correction skill as a function of the anticipated quality of the rainfall estimates. All statistics show a trend of improving values with increasing RQI. The trend of CC is a little more complicated with a linear increase up to an RQI of 0.4 and then no improvements thereafter. For uncorrected radar QPE, the RB is lower than -80% and MAE is higher than 1.6 mm when RQI is less than 0.2. The low RQI score mainly corresponds to poor quality QPE caused by sampling well above the melting layer in the ice region. The improved performance of the CVPR-IE is more evident when RQI is low and becomes less significant with increasing RQI, i.e. when radar QPE is less affected by beam sampling problems. When RQI equals unity the radar beam samples rain close to the surface. We again note that the RB is negative even when RQI equals unity. This systematic underestimation is not associated with the variability of VPR and may come from other sources of uncertainty such as Z-R relationship and radar miscalibration.

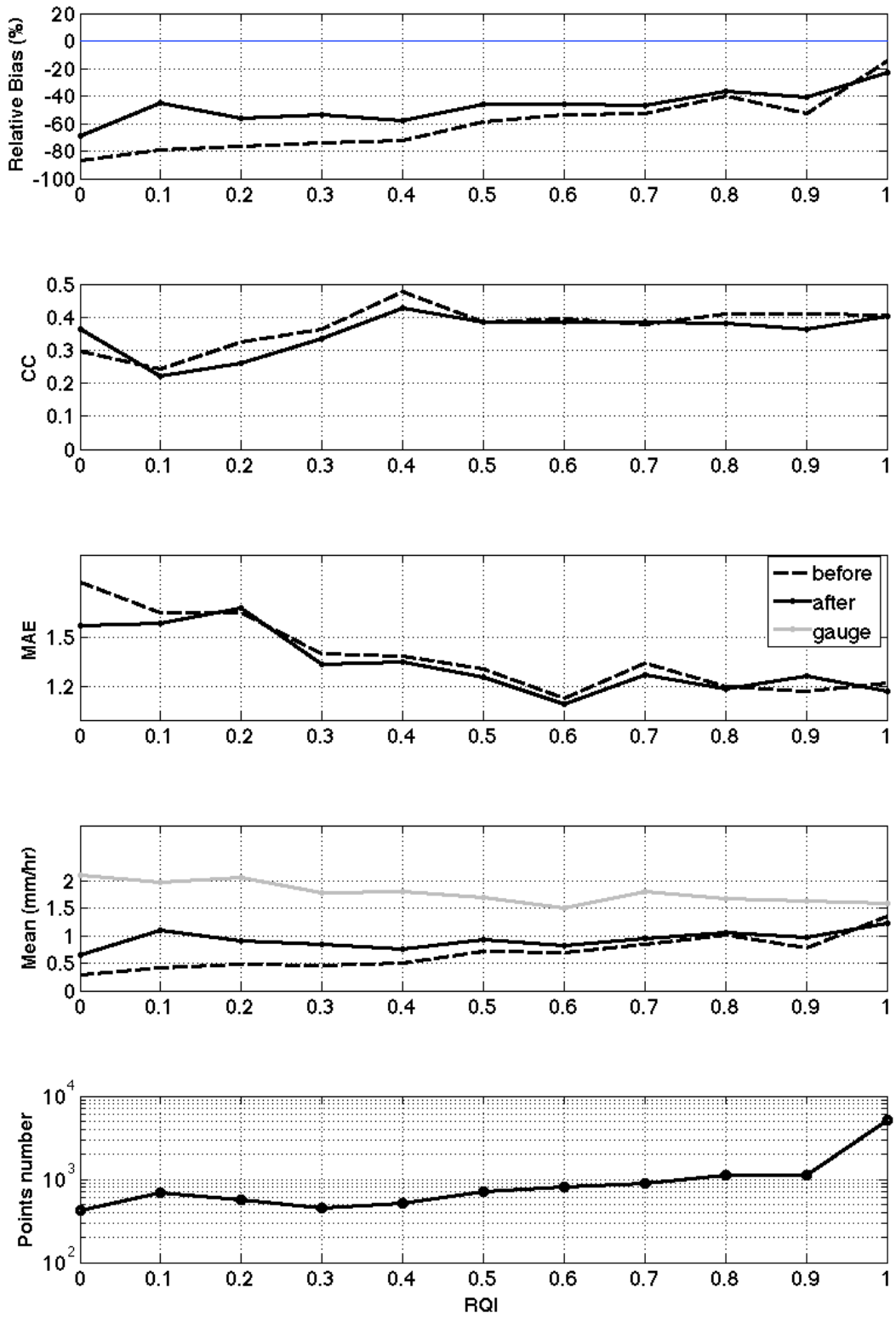

Figure 4.12. Similar to Fig. 4.11. But statistics are along Radar Quality Index (RQI).

d. Verification with precipitation type

CVPR-IE is applied to stratiform echoes on 5-min radar data, which is then accumulated to hourly scale to match the temporal resolution of rain gauges. After the accumulation process, other precipitation types, such as convective, hail or undefined precipitation type, may become prevalent at a given grid point and thus obscure the degree of correction that was made to the stratiform rain echoes. To address this, Fig. 4.13 shows the statistics as a function of the number of occurrences stratiform echoes that were detected within the hour for each grid point. As the proportion of stratiform rain type increases, RB of both uncorrected and corrected QPE improves and the difference between them increases, indicating that the CVPR_IE functions most effectively with widespread, stratiform rain. CC stays relatively constant with increasing stratiform occurrences within the hour. After applying the CVPR-IE correction, CC is slightly improved relative to the uncorrected rainfall estimates. The increasing MAE values with increasing stratiform rain proportion is due to increasing rainfall accumulations. If stratiform rain did not occur, it is likely that precipitation was simply absent at that 5-min time step, thus resulting in lighter hourly accumulations. This inference is supporting by the trend of increasing rainfall accumulations in Fig. 4.13d. There is no difference in MAE following correction using the CVPR-IE method.

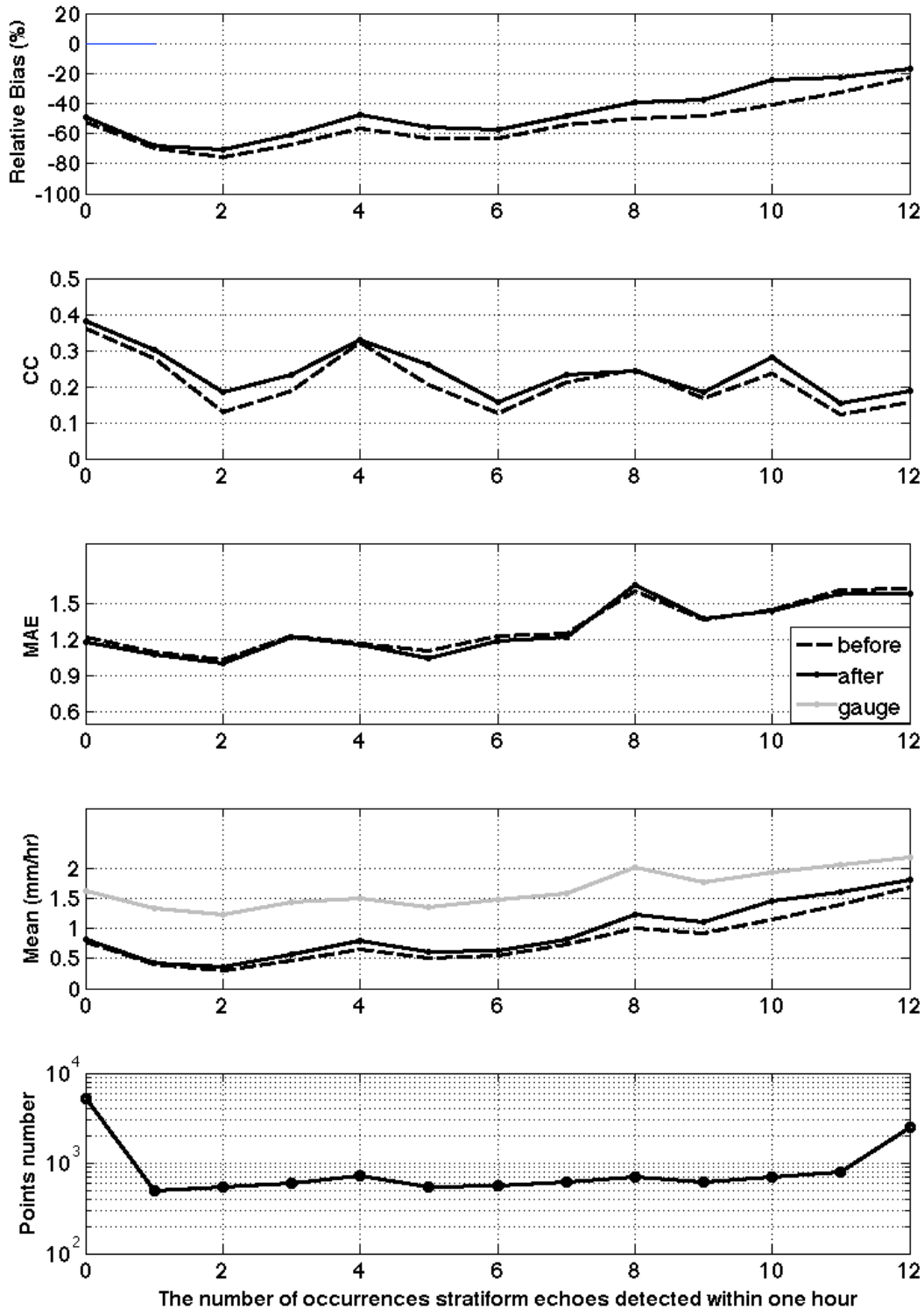

Figure 4.13. Similar to Fig. 4.11. Statistics are along the stratiform precipitation proportion in one hour

Another precipitation type category defined in the NMQ system is called Bright Band (BB), which contains radar measurements of melting hydrometeors 800 meters below the top of the freezing level. As the proportion of the BB type increases, the RB generally increases, CC does not exhibit a clear trend, and MAE increases in correspondence with increasing precipitation amounts (Fig. 4.14). The corrected QPE shows improvements in all three statistics, especially when the BB occurrence is greater than 4.

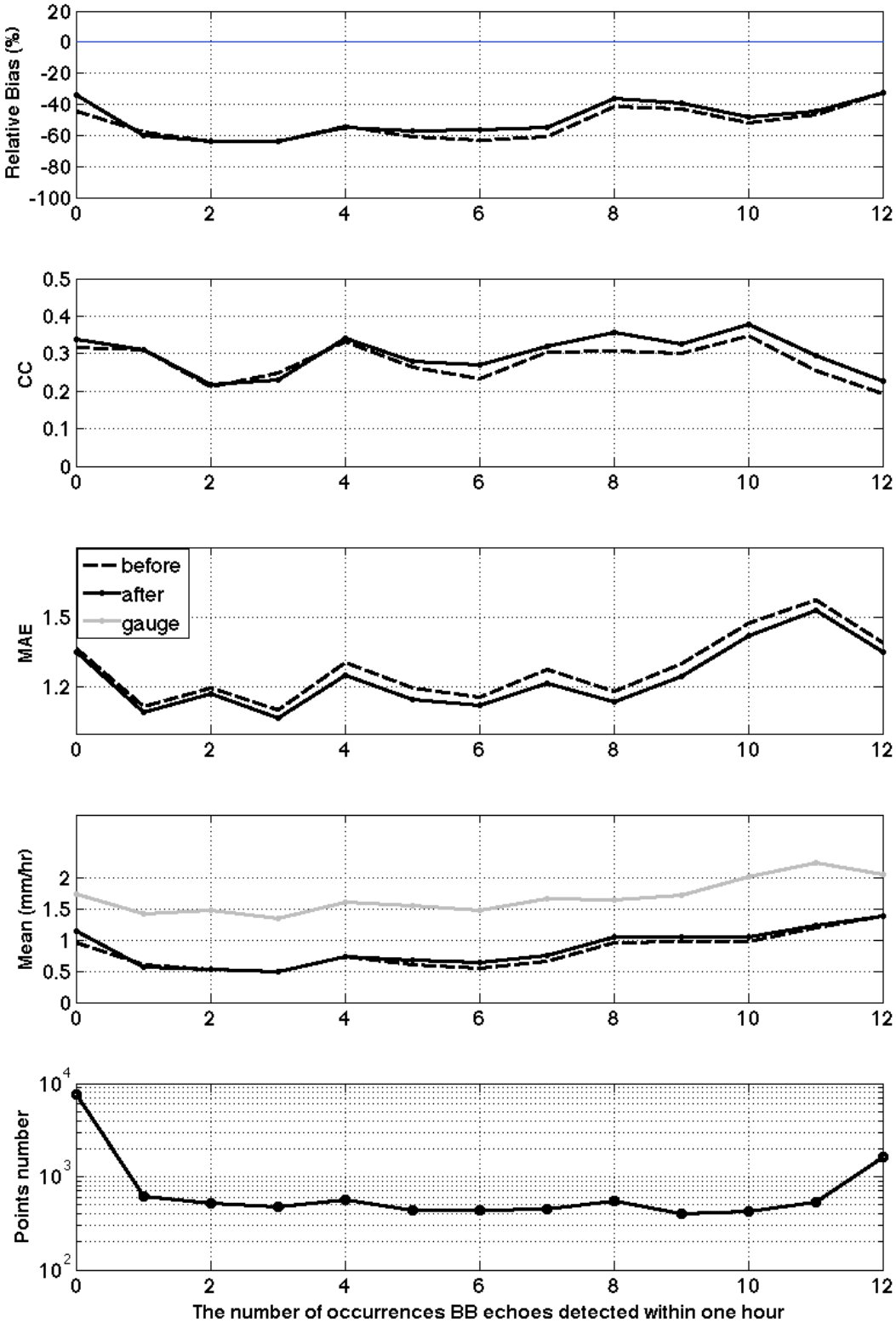

Figure 4.14. Similar to Fig. 4.11. Statistics are with Bright Band precipitation proportion.

4.3.3 Discussion

a. Limitation of Climatological VPR-IE

As demonstrated in the previous section, CVPR-IE mitigates range-dependent errors to some extent. The improvement is mainly seen in RB while CC and MAE only have marginal improvements. Also, the improvement in RB is only around 6%, which is more limited than the improvements (~20%) made by the physically based VPR-IE (Wen et al., 2013). To examine the reasons behind these differences, CVPR-IE was applied to the cases investigated in Wen et al. (2013). The Absolute Error (|Radar - Gauge|), MAE, RMSE and CC are calculated for radar QPE after VPR-IE processing. To quantify the relative differences between the two different VPR-IE correction methods, the statistics are computed as a percent difference relative to the radar-only QPE as shown in Table 7. Improvements occur if there is a reduction in AE, MAE, RMSE and an increase in CC. The analysis is conducted for specific hours when PR overpasses are available since the physically-based VPR-IE method is limited by the temporal resolution of PR. In general, the physically-based VPR-IE method yields more improvements for all five events.

Table 7. Relative changes of statistics due to CVPR-IE and physically based VPR-IE.

	Change of AE (%)		Change of MAE (%)		Change of RMSE (%)		Change of CC (%)	
	Climate	Physical	Climate	Physical	Climate	Physical	Climate	Physical
8 Feb 2009	-3.25	-22.92	-6.20	-24.00	-5.99	-20.00	269.23	104.35
8 Dec 2009	-11.84	-52.02	-1.27	-16.28	0.78	-9.91	3.03	75.00
22 Jan 2010	-4.03	-40.57	-4.85	-27.40	-2.91	-20.80	41.67	100.00
28 Feb 2010	-28.00	-53.52	-9.41	-28.10	-12.53	-36.02	2.53	2.12
7 Mar 2010	23.98	-69.94	-18.98	1.134	-3.31	-3.85	40.00	77.97

The CVPR-IE also improves upon the radar-only QPE but not drastically. The 8 Dec 2009 event is demonstrated in further detail as an example to show the differences between the physical and climatological VPR correction methods. This is a widespread

stratiform event with heavy precipitation and a 0° C-level height of 2500 m. For most of the rainy areas shown in Fig. 4.15a, the radar beam has overshot the melting layer, which led to underestimation of rainfall on the surface. The physical VPR-IE induces the greatest increase of precipitation rate at ground (Fig. 4.15b). Rainfall estimates using the CVPR-IE correction is shown in Fig. 10c. Compared to Fig. 4.15a, the CVPR-IE method increases rainfall estimates around KFSX but not sufficiently. Also, the underestimation within the area around 34.2° in latitude and -112.5° in longitude still remains after CVPR-IE by comparing to the gauge measurements on the ground. The reflectivity measured in this area is 25 dBZ. The corresponding climatological for this grid point is plotted in Fig. 4.16a, along with the physically-based VPR coming from actual PR measurements for the specific event. The physical VPR has a steeper slope in ice region, which provides larger correction on surface level reflectivity compared to the climatological one. The climatological VPR of 25 dB with a less steep slope in ice region limits the correction magnitude. For the rain areas 100 km east of KESX, where the beam height is around 1000 m relative to the freezing level (Fig. 4.16b), the correction of reflectivity using the physical VPR is more than 10 dB, while the climatological one is only ~5dB. The climatological VPR's deviation from the physically-based VPR and its consequent effect on the correction skill exposes the limitation of a climatological VPR correction and emphasizes the importance of ingesting real time information from TRMM/PR or GPM DPR. Blending real time VPR information from other sources, e.g. TRMM/PR, GPM/DPR, with climatological VPRs can solve the VPR variability issue and make the VPR-IE method more robust.

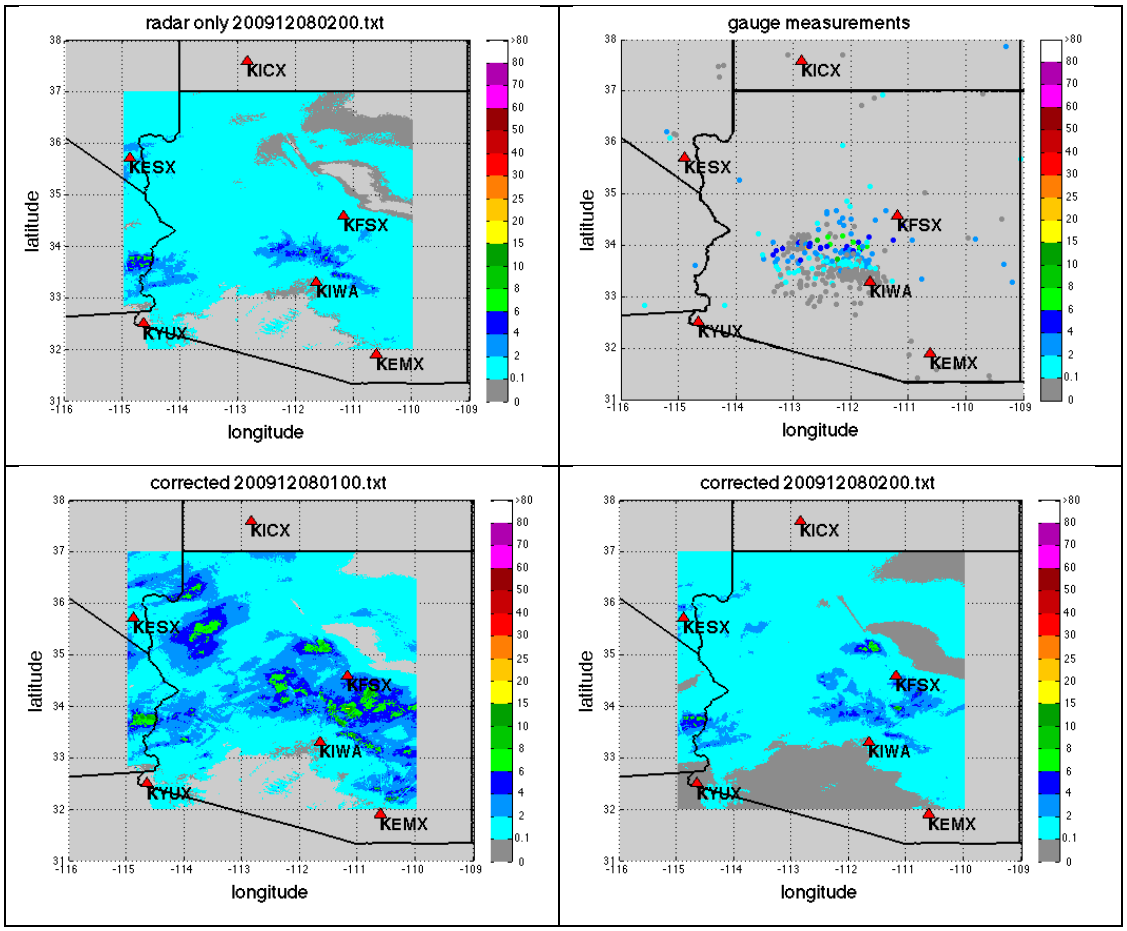

Figure 4.15. Hourly precipitation accumulation from Event 8 Dec 2009. (a) Radar only QPE; (b) Gauge measurements from HADS and the Maricopa County mesonet; (c) Using physically-based VPR-IE approach; (d) Using climatological VPR-IE scheme approach. The red triangles denote the locations of WSR-88D radar sites

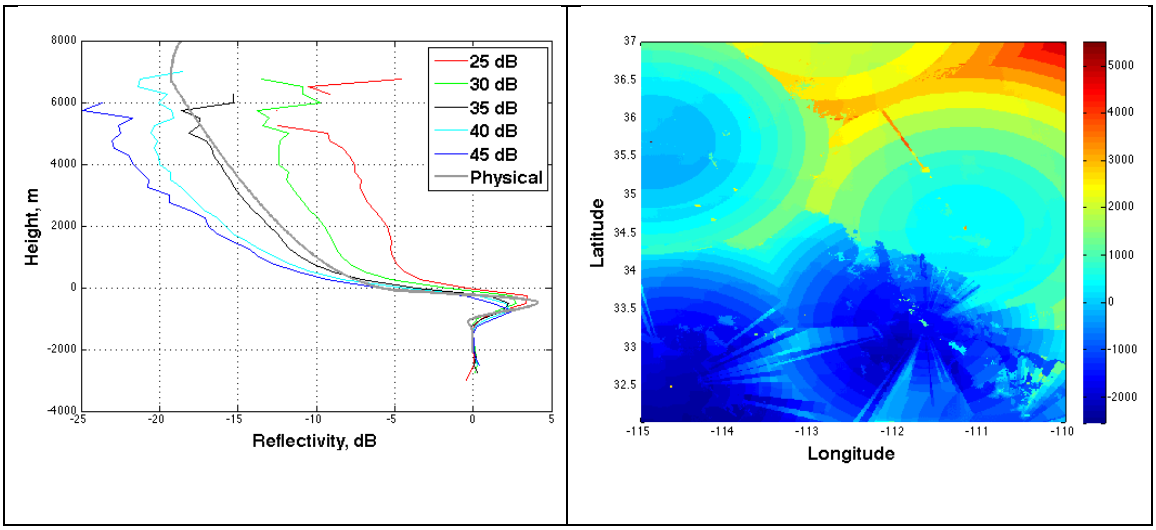

Figure 4.16. (a) Physically based VPR from Event 8 Dec 2009 (gray line) and climatological VPRs; (b) Beam height relative to the freezing level in meters.

b. Z-R relation uncertainty

All results up to now have shown underestimation both before and after application of the correction methodology. The RB improved by only 6% from -46% to -40% when considering gauge-radar pairs at all ranges from radar. Moreover, negative biases remained before and after correction for those bins measured well below the melting layer where the method assumes the radar-only estimates are trustworthy. The CVPR-IE method is essentially correcting data measured aloft to the radar-only rainfall estimates measured below the melting layer. If the rainfall estimates are biased in this region that is assumed to be trustworthy, then the bias will propagate to other bins. This underestimation may be due to an inappropriate Z-R relationship. Kirstetter et al. (2014) provides a new set of Z-R relationships within a paradigm of probabilistic precipitation rate estimates. After applying the newly proposed Z-R relationship, the RB of uncorrected rainfall estimates becomes -11.09% instead of the prior -46.43% (Table 1) using the default Z-R relation for stratiform precipitation in NMQ. After CVPR-IE

correction, the RB is improved to -0.10%. The improper former Z-R relationship masked the improvement of the CVPR-IE scheme, which could mitigate range-dependent errors in reflectivity successfully.

References

Andrieu, H., and J. D. Creutin, 1995: Identification of vertical profiles of radar reflectivity for hydrological applications using an inverse method. Part I: Formulation. J. Appl. Meteor., **34**, 225–239.

Bellon, A., G.-W. Lee, and I. Zawadzki, 2005: Error statistics of VPR corrections in stratiform precipitation. J. Appl. Meteor., **44**, 998–1015.

Borga, M., Anagnostou, E.N. and Frank, E. (2000). On the use of real-time radar rainfall estimates for flood prediction in mountainous basins. Journal of Geophysical Research 105: doi: 10.1029/1999JD900270. issn: 0148-0227.

Cao Q., Y. Hong, J.J. Gourley, Y. Qi, J. Zhang, Y. Wen, and P. Kirstetter, 2012: Statistical and Physical Analysis of Vertical Structure of Precipitation in Mountainous West Region of US using 11+ Year Spaceborne TRMM PR Observations, Journal of Applied Meteorology and Climatology, doi: http://dx.doi.org/10.1175/JAMC-D-12-095.1.

Cao Q., Y. Hong, Y. Qi, Y. Wen, J. Zhang, J. Gourley, and L. Liao, 2013: Empirical Conversion of Vertical Profile of Reflectivity (VPR) from Ku-band to S-band Frequency, Journal of Geophysical Research, **118**, 1-12, DOI: 10.1002/jgrd.50138.

Cao Q., Y. Wen, Y. Hong, J.J. Gourley, and P. Kirstetter, 2014: Enhancing Quantitative Precipitation Estimation (QPE) over Continental United States (CONUS) using a Physically-based Multi-sensor Integration Approach. IEEE Geoscience and Remote Sensing Letters, **11(7),** 1305-1309. doi:10.1109/LGRS.2013.2295768.

Efron, B., 1979: "Bootstrap methods: another look at the jackknife," The Annals of Statistics, **7**, no. 1, pp. 1–26.

Fabry, F., and I. Zawadzki, 1995: Long-term radar observations of the melting layer of precipitation and their interpretation. J. Atmos. Sci., **52**, 838–851.

Gabella, M., J. Joss, S. Michaelides, and G. Perona (2006), Range adjustment for ground-based radar, derived with the spaceborne TRMM Precipitation Radar, IEEE Trans. Geosci. Remote Sens., 44, 126–133, doi:10.1109/TGRS.2005.858436.

Germann, U. and J. Joss, 2002: Mesobeta profiles to extrapolate radar precipitation measurements above the Alps to the ground level. J. Appl. Meteor., **41**, 542-557

Kirstetter, P., H. Andrieu, G. Delrieu and B. Boudevillain, 2010: Identification of Vertical Profiles of Reflectivity for Correction of Volumetric Radar Data Using Rainfall Classification. J. Appl. Meteor. Climatol., **49**, 2167-2180

Kirstetter, P.E., H. Andrieu, B. Boudevillain and G. Delrieu, 2013: A physically-based identification of vertical profiles of reflectivity from volume scan radar data. Journal of

Applied Meteorology and Climatology, **52**, 1645-1663. doi: 10.1175/JAMC-D-12-0228.1

Kirstetter, P.E., J.J. Gourley, Y. Hong,J. Zhang, S. Moazamigoodarzi, C. Langston, A. Arthur : A Paradigm for Probabilistic Precipitation Rate Estimates with Ground-based Radar Networks. Water Resources Research, accepted

Kitchen, M., R. Brown, and A. G. Davies, 1994: Real-time correction of weather radar data for the effects of bright band, range and orographic growth in widespread precipitation. Quart. J. Roy. Meteor. Soc., **120**, 1231–1254. Klaassen 1988

Lakshmanan, V., A. Fritz, T. Smith, K. Hondl, and G. J. Stumpf, 2007: An automated technique to quality control radar reflectivity data. J. Appl. Meteor. Climatol., **46**, 288 – 305

Maddox, R., J. Zhang, J.J. Gourley, and K. Howard, 2002: Weather radar coverage over the contiguous United States. Wea. And Forecast., **17**, 927-934

Schumacher, C., and R. A. Houze Jr., 2003: Stratiform rain in the Tropics as seen by the TRMM precipitation radar. J. Climate, **16**, 1739–1756

Tabary, P., 2007: The new French operational radar rainfall product. Part I: Methodology. Wea. Forecasting, **22**, 393–408

Vignal, B., H. Andrieu, and J. D. Creutin, 1999: Identification of vertical profiles of reflectivity from volume-scan radar data. J. Appl. Meteor., **38**, 1214–1228

Maddox, R., J. Zhang, J.J. Gourley, and K. Howard, 2002: Weather radar coverage over the contiguous United States. Wea. And Forecast., **17**, 927-934.

Vignal, B., and W. F. Krajewski, 2001: Large-sample evaluation of two methods to correct range-dependent error for WSR-88D rainfall estimates. J. Hydrometeor., **2**, 490–504.

Wen Y., Q. Cao, P.-E. Kirstetter, Y. Hong, J. J. Gourley, J. Zhang, G. Zhang, B. Yong, 2013: Incorporating NASA Spaceborne Radar Data into NOAA National Mosaic QPE System for Improved Precipitation Measurement: A Physically Based VPR Identification and Enhancement Method. J. Hydrometeor, **14**, 1293–1307. doi: http://dx.doi.org/10.1175/JHM-D-12-0106.1.

Zhang J. and Y. Qi, 2010: A real-time algorithm for the correction of brightband effects in radar-derived QPE. J. Hydrometeor., **11**, 1157- 1171

Zhang. J., K. Howard, C. Langston, S. Vasiloff, B. Kaney, A. Arthur, S. V. Cooten, K. Kelleher, D. Kitzmiller, F. Ding, D. J. Seo, E. Wells, and C. Dempsey, 2011: National Mosaic and Multi-sensor QPE (NMQ) System: Description, Results, and Future Plans. Bull. Amer. Meteor. Soc., 92, 1321–1338

Chapter 5 Overall conclusions and future work

5.1 Summary and conclusions

5.1.1 Summary of Chapter 2: Ground Polarimetric Weather Radar

This Chapter provides a quantitative assessment of TRMM PR melting layer and reflectivity measurements as compared to a S-band polarimetric radar located in Norman, Oklahoma. The KOUN ground-based radar is the prototype, proof-of-concept radar for the ongoing upgrade of the NEXRAD network. KOUN is shown to be particularly useful in this analysis due to its ability to filter non-meteorological echoes and discriminate hydrometeor species, each of which has differing scattering characteristics at Ku- and S-band frequencies. The main findings are summarized as follows:

1. Comparisons of TRMM PR and KOUN melting layer heights reveal a correlation coefficient of 0.88 and relative bias of 5.94%. The differences are deemed to be due to the vertical vs. horizontal scanning and resolution volume differences rather than systematic offsets that might have pointed to algorithmic errors.
2. NASA's resolution volume matching technique is used to match and compare simultaneous TRMM PR and KOUN reflectivity observations. The results indicate a negligible bias (<0.2%) due to calibration differences between PR and KOUN. However, for Z >50 dBZ, reflectivity from KOUN is slightly higher than that from PR, likely due to non-Rayleigh scattering for Ku band of PR.

3. By comparing reflectivity with respect to different hydrometeor types (as determined by KOUN's Hydrometeor Classification Algorithm), we find biases are primarily from rain/hail mixture, wet snow, graupel, and heavy rain, respectively. These results agree with differences in simulated reflectivity differences at Ku and S band using the T-matrix method, with the notable exception of dry snow. Assumptions for simulating reflectivity in dry snow need to be further investigated.
4. Comparison of vertical reflectivity profiles shows that PR suffers significant attenuation, especially in convective rain and within the melting layer. However, TRMM PR observations correspond very closely with KOUN reflectivity measured nearest to the surface, thus indicating no systematic biases are caused by the TRMM attenuation correction procedures.
5. The polarimetric signatures of snow provide valuable insights into the microphysical processes/properties. The QVP of polarimetric data is an efficient way to examine the temporal evolution of microphysical processes.
6. The polarimetric signatures aloft in the ice parts can help us discriminate snow riming from aggregation by the enhancement of Z and the decrease of Z_{DR}, and the saggy melting layer shape.
7. The intercept α in the power-law relation $S=\alpha Z^{\beta}$ increases with height and decreasing temperature. The α is almost entirely dependent on the intercept of the exponential size distribution of snow N_0. The decreasing of N_0 with increasing temperature and decreasing altitude is aggregation of ice crystals and snowflakes.

NASA has called for comprehensive sensor calibration and ground validation research to be conducted to ensure proper accuracy and precision of the space-borne QPE missions (Petersen and Schwaller 2008). With the upgrad of the U.S. national weather radar network to include polarimetric capabilities, the polarimetric algorithms developed on the prototype KOUN radar may be able to serve as the basis for a nation-wide validation network using polarimetric NEXRAD data for NASA space QPE products. This research motivates and invites synergistic development of multisensor rainfall algorithms using coordinated observations from space and ground.

5.1.2 Summary of Chapter 3: VPR_IE methods

In this Chapter, we have demonstrated the effective integration of the Ku-band TRMM PR products (radar reflectivity, precipitation type, and quantity at 4-km horizontal and 250-meter vertical resolutions) into the NMQ system to improve the S-band ground-based radar rainfall estimation. Our major interest focuses on mountainous regions where beam blockages, overshooting, and intercepting the melting layer remain the major problems for ground radar-based QPE. This study proposes a VPR-IE method to improve the surface rainfall estimate in the Mountainous West region by synergistically integrating observations from spaceborne TRMM PR into NEXRAD-based radar products. With the physically-based VPR model, the TRMM 3-D reflectivity profile (Ku-band) is used to derive a representative VPR at S-band within a specific region (e.g., a region of stratiform precipitation). Surface rainfall estimates, which were previously hampered by sampling within or above the melting layer, can be greatly improved through the incorporation of the TRMM-observed VPR data.

The VPR-IE method has been evaluated with several stratiform precipitation events in Arizona. Two other statistically-based correction methods, TRMM-based rainfall calibration and the rings-based range adjustment, have also been compared with the physically-based VPR method. The statistical analysis shows that the VPR-IE method has the best overall performance and provides much more accurate surface rainfall estimates than the original radar QPE in the current NMQ system for the study region

5.1.3 Summary of Chapter 4: real time VPR_IE methods

This study provides a quantitative assessment of a climatological VPR-IE technique for all winter events in 2011 over a study region in the Intermountain West of the US, where the climatological VPRs are derived from 11+ years of TRMM/PR observations. The main results are summarized as follows:

(1) The statistical analysis shows that the CVPR-IE method provides improvements over the original radar QPE in the current NMQ system.

(2) The statistical significance of the correction skill is further examined using a bootstrapping method based on different sample sizes. The results show that the CVPR-IE method improves radar surface rainfall measurement systematically.

(3) The CVPR-IE mitigates radar underestimation for samples obtained in the ice region but the correction was not enough to remove all negative bias.

(4) The statistics show improvements in radar QPE following application of the CVPR-IE were most effective for bins measured above the melting layer, bins with low radar quality index values, and for gauge-radar pairs that were dominated by stratiform precipitation type.

(5) Compared to a physically-based VPR from real time PR measurements, climatological VPRs have limitations in representing precipitation structures for each individual event. The physically-based VPRs, on the other hand, are updated on a twice daily basis corresponding to a satellite overpass. A hybrid VPR correction scheme incorporating both climatological and real time VPR information is desired to optimize skill in a real time system.

5.2 GPM era

GPM mission is a joint mission led by NASA and Japan Aerospace Exploration Agency (JAXA) designed to monitor and study global precipitation measurements. The core satellite, launched on Feb. 27, 2014 from Japan, flies in non-sun-synchronous orbit (65° inclination on a 407-km-high circular orbit) to serve as a physics observatory to gain insights into precipitation systems and as a calibration reference to unify and refine precipitation estimates from a constellation of research and operational satellites involving passive microwave sensors (Hou et al, 2014). The core satellite carries the Ku/Ka-band DPR and a microwave radiometer (GMI). The DPR is expected to improve the single frequency radar capabilities of the TRMM PR, providing estimates of microphysical properties and vertical structure information of precipitating systems. The GMI with its 1.2-m antenna, is capable of providing measurements at the highest spatial resolution among all constellation radiometers, which is important for obtaining accurate fixes of storm centers for track predictions (Hou et al, 2014). The GPM constellation includes a number of satellites with GMI-like radiometers or microwave sounding instruments. The GPM core satellite sensors are used as a reference to inter-calibrate the constellation radiometers, thus providing self-consistent radiometric observations across the constellation. The higher sensitivity of the DPR Ka-band radar (12 dBZ) relative to the TRMM radar and the high-frequency channels on the GMI give GPM new capabilities to take on the challenge of measuring light rains (i.e., <0.5 mm/hr) and falling snow.

The current VPR-IE schemes (both physically based and climatological) are restricted by the TRMM satellite coverage between 36 N and 36 S. With the recent

availability of Global Precipitation Measurement (GPM) Dual-frequency PR, the VPR-IE approach is anticipated to become more robust when extended to higher latitude mountainous regions. Further, the refined DPR and GMI measurements by quantifying the microphysical properties of precipitating particles provide more insight information of storm vertical structure and storm evolve, which potentially constrains the representative VPRs and decreases its uncertainty.

References

Petersen, Walter A and M. R. Schwaller, 2008: NASA GPM Ground Validation Science Implementation Plan.

Arthur Y. Hou, Ramesh K. Kakar, Steven Neeck, Ardeshir A. Azarbarzin, Christian D. Kummerow, Masahiro Kojima, Riko Oki, Kenji Nakamura, and Toshio Iguchi, 2014: The Global Precipitation Measurement Mission. *Bull. Amer. Meteor. Soc.*, **95**, 701–722. doi: http://dx.doi.org/10.1175/BAMS-D-13-00164.1